In-situ glial cell-surface proteomics identifies pro-longevity factors in *Drosophila*

Authors:
Madeline P. Marques[1,2,4], Bo Sun[1,2], Ye-Jin Park[1,2], Tyler Jackson[1,2], Tzu-Chiao Lu[1,2], Yanyan Qi[1,2], Erin Harrison[1,2], Miranda C. Wang[1,2], Kartik Venkatachalam[3], Omar Moussa Pasha[1,2,4], Amogh Varanasi[1,2,3,4], Dominique Kiki Carey[5], D.R. Mani[5], Jonathan Zirin[6], Mujeeb Qadiri[6], Yanhui Hu[6], Norbert Perrimon[6,7], Steven A. Carr[5], Namrata D. Udeshi[5], Liqun Luo[8], Jiefu Li[9], Hongjie Li[1,2]*

Affiliations:
1 Huffington Center on Aging, Baylor College of Medicine, Houston, TX 77030, USA.
2 Department of Molecular and Human Genetics, Baylor College of Medicine, Houston, TX 77030, USA.
3 Department of Integrative Biology and Pharmacology, University of Texas Health Science Center at Houston, Houston, TX, 77030, USA.
4 Department of BioSciences, Rice University, Houston, TX, 77005, USA
5 The Broad Institute of MIT and Harvard, Cambridge, MA 02142, USA
6 Department of Genetics, Blavatnik Institute, Harvard Medical School, Harvard University, Boston, MA 02115, USA
7 Howard Hughes Medical Institute, Boston, MA 02138, USA
8 Department of Biology, Howard Hughes Medical Institute, Stanford University, Stanford, CA 94305, USA
9 Janelia Research Campus, HHMI, Ashburn, VA 20147

*Corresponding author: hongjie.li@bcm.edu (H.L.)

Abstract

Much focus has shifted towards understanding how glial dysfunction contributes to age-related neurodegeneration due to the critical roles glial cells play in maintaining healthy brain function. Cell-cell interactions, which are largely mediated by cell-surface proteins, control many critical aspects of development and physiology; as such, dysregulation of glial cell-surface proteins in particular is hypothesized to play an important role in age-related neurodegeneration. However, it remains technically difficult to profile glial cell-surface proteins in intact brains. Here, we applied a cell-surface proteomic profiling method to glial cells from intact brains in *Drosophila,* which enabled us to fully profile cell-surface proteomes *in-situ*, preserving native cell-cell interactions that would otherwise be omitted using traditional proteomics methods. Applying this platform to young and old flies, we investigated how glial cell-surface proteomes change during aging. We identified candidate genes predicted to be involved in brain aging, including several associated with neural development and synapse wiring molecules not previously thought to be particularly active in glia. Through a functional genetic screen, we identified one surface protein, DIP-β, which is down-regulated in old flies and can increase fly lifespan when overexpressed in adult glial cells. We further performed whole-head single-nucleus RNA-seq, and revealed that DIP-β overexpression mainly impacts glial and fat cells. We also found that glial DIP-β overexpression was associated with improved cell-cell communication, which may contribute to the observed lifespan extension. Our study is the first to apply *in-situ* cell-surface proteomics to glial cells in *Drosophila*, and to identify DIP-β as a potential glial regulator of brain aging.

Short title: Glial cell-surface proteomics in aging

Keywords: *Drosophila,* glia*,* aging, *in-situ* cell-surface proteomics, DIP-β, snRNA-seq

Introduction

During aging, several changes occur in the brain that render it more vulnerable to a variety of age-related neurodegenerative diseases, including Alzheimer's Disease and Parkinson's Disease (Mattson and Arumugam, 2018). Aging, defined as a time-related decline in physiological functions (Ebeling et al., 2021; Dorsey and Bloem, 2024), is considered the strongest risk factor for these conditions. While these neurodegenerative diseases share many phenotypic similarities with normal brain aging, we still do not fully understand the mechanisms underlying brain aging, nor how these mechanisms deviate in each of these unique pathologies (Mattson and Arumugam, 2018; Iijima et al., 2004; Drachman, 2006; Moqri et al., 2023). By characterizing the functions and mechanisms responsible for brain aging and establishing a foundational understanding of how "normal" age-related neurodegeneration occurs, we will be far better equipped to develop more targeted interventions moving forward.

Recently, much focus has shifted towards understanding how glial dysfunction may contribute to age-related neurodegeneration. This is largely due to the many crucial roles glial cells play in maintaining healthy brain function, including moderating cell-cell interactions, maintaining homeostasis, facilitating immune responses, etc. (Barres, 2008; Freeman, 2015; Kremer et al., 2017). Cell-cell interactions, which are largely mediated by cell-surface proteins, control many critical aspects of development and physiology (Sperry, 1963; Malenka and Bear, 2004; Jan and Jan, 2010; Zipursky and Sanes, 2010; Kolodkin and Tessier-Lavigne, 2011; Yeh et al., 2017; Li et al., 2020; McAlpine et al., 2021). As dysregulation of glia-neuron interactions is considered a hallmark of normal brain aging (Barres, 2008), glial cell-surface proteins are hypothesized to play important roles in maintaining healthy brain function during aging (Kremer et al., 2017). However, fully characterizing the cell-surface proteomes of glial cells has proven challenging using traditional proteomics methods, such as biochemical fractionation (Cordwell and Thingholm, 2010; Li et al., 2020). This is because biochemical fractionation does not allow for cell-type specificity, includes various contaminants (mitochondrial, ER, and Golgi), and, importantly, omits important secreted and extracellular matrix proteins that form an integral part of the cell-surface proteome (Li et al., 2020).

Recently, *in-situ* cell-surface proteomics methods were developed to profile spatiotemporally resolved neuronal cell-surface proteomes from intact brains in *Drosophila* (Li et al., 2020; Xie et al., 2022), as well as in certain mouse brain regions (Shuster et al., 2022). This technique enables complete profiling of cell-surface proteomes *in-situ*, preserving native cell-cell interactions (Li et al., 2020; Xie et al., 2022). Ultimately, this allows investigators to form a more comprehensive understanding of how glia-neuron interactions evolve during aging (as this method effectively captures both the glial cell-surface proteins themselves, as well as any other endogenous proteins that are in very close proximity) (Li et al., 2020; Xie et al., 2022). Applying this platform to the glial cells of young and old flies, we investigated how glial cell-surface proteomes change as flies age. We identified several candidate proteins predicted to be involved in normal brain aging, including several neural development and synapse wiring molecules not previously thought to be particularly active in glia or in aging (Szklarczyk et al., 2023). We found that one synapse wiring molecule in particular, DIP-β, was associated with significant lifespan

increases when overexpressed in adult glial cells (using the *glial-GeneSwitch* conditional driver). Our single-nucleus RNA-seq data suggest that glial DIP-β overexpression improves cell-cell communication, including glia-neuron and glia-fat cell interactions, contributing to lifespan extension.

Our study is the first to apply *in-situ* cell-surface proteomics to glial cells in *Drosophila*, and to fully profile and characterize the glial cell-surface proteomes of aging-model (i.e., young and old) flies. Additionally, while DIP-β's role in precise neural circuit assembly during development has been studied extensively (Carrillo et al., 2015; Cosmanescu et al., 2018; Sanes and Zipursky, 2020; Sergeeva et al., 2020; Wang et al., 2022; Ma et al., 2023), ours is the first to identify DIP-β as a potential regulator of healthy brain function and synapse maintenance during normal brain aging. Combined, these results further demonstrate the power of *in-situ* cell-surface proteomics to identify new molecules involved in the maintenance of healthy brain function during aging.

Results

Glial cell-surface proteomes from young and old fly brains

To fully profile the cell-surface proteomes of glial cells in intact fly brains, we used a modified peroxidase-mediated proximity-based biotinylation procedure (Li et al., 2020; Loh et al., 2016; Xie at al., 2022). To accomplish cell-type and cell-surface specificity, we employed the glia-specific driver *Repo-GAL4* to drive transgenic expression of horseradish peroxidase (HRP) fused to the N-terminus of the transmembrane protein rat CD2 (*UAS-HRP-CD2*). This simultaneously targets HRP-CD2 to the extracellular side of the plasma membrane, while restricting HRP-CD2 expression to glial cells (Larsen et al., 2003; Watts et al., 2004; Li et al., 2020). Next, we used the biotin-xx-phenol (BxxP) substrate, which is unable to cross the plasma membrane (Loh et al., 2016; Li et al., 2020; Durojaye, 2021; Renuse et al., 2020). Combined with the glial cell-surface-targeting of HRP-CD2, this dual-gate approach is designed to enhance the specificity toward glial cell-surface proteins. In the presence of hydrogen peroxide (H_2O_2), HRP forms a reactive complex (HRP-H_2O_2), which converts BxxP into short-lived phenoxyl radicals that rapidly biotinylate endogenous proteins that are in very close proximity (**Fig. 1A**). Because the half-life of these phenoxyl radicals is extremely short (less than 1 millisecond) and the reaction requires only a few minutes to complete, phenoxyl radicals can only label proteins within a very small radius from the peroxidase enzyme. Thus, this provides a snapshot of the cell-surface proteome with high temporal resolution, while minimizing the potential toxic effects of hydrogen peroxide.

To validate HRP-mediated cell-surface biotinylation of glial cells in intact brains, we crossed *Repo-GAL4* with either *UAS-HRP-CD2* or wildtype (w1118) and stained brains with a fluorophore-conjugated neutravidin, which specifically recognizes biotin. We observed extensive HRP-dependent biotinylation of glial cells (**Fig. 1B**). Biochemical characterization by streptavidin blot of the post-enrichment eluate showed that the glial cell-surface-targeted HRP biotinylated a wide range of endogenous proteins compared to the control lacking HRP-CD2 expression (**Fig. 1C**).

Figure 1

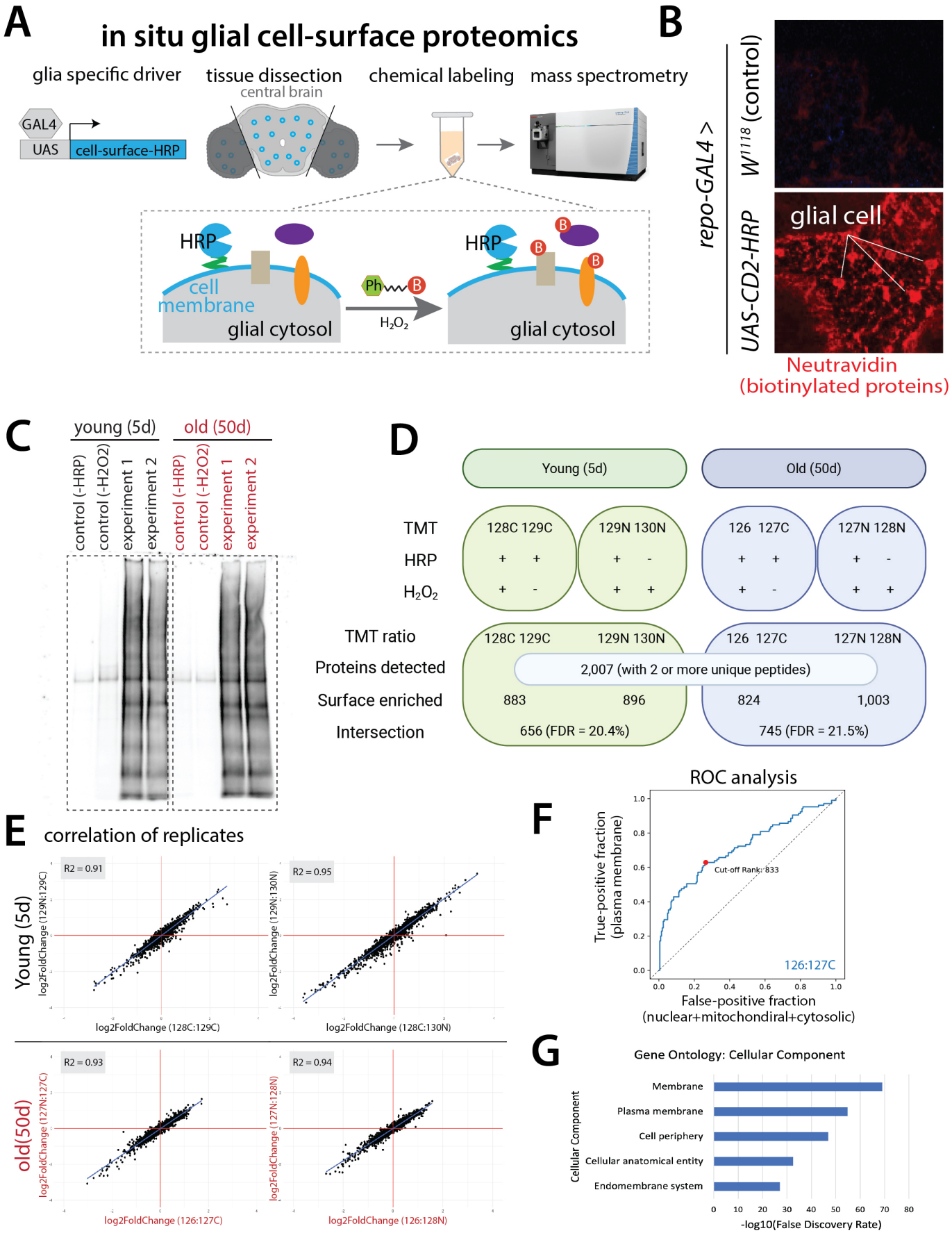
A
in situ glial cell-surface proteomics
glia specific driver
tissue dissection
chemical labeling
mass spectrometry
central brain
GAL4
UAS
cell-surface-HRP
HRP
cell membrane
glial cytosol
Ph
B
H_2O_2
B
repo-GAL4 >
W^{1118} (control)
UAS-CD2-HRP
glial cell
Neutravidin
(biotinylated proteins)
C
young (5d)
old (50d)
control (-HRP)
control (-H2O2)
experiment 1
experiment 2
D
Young (5d)
Old (50d)
TMT
HRP
H_2O_2
128C 129C
129N 130N
126 127C
127N 128N
TMT ratio
Proteins detected
2,007 (with 2 or more unique peptides)
Surface enriched
883
896
824
1,003
Intersection
656 (FDR = 20.4%)
745 (FDR = 21.5%)
E
correlation of replicates
Young (5d)
old(50d)
R2 = 0.91
R2 = 0.95
R2 = 0.93
R2 = 0.94
log2FoldChange (129N:129C)
log2FoldChange (129N:130N)
log2FoldChange (127N:127C)
log2FoldChange (127N:128N)
log2FoldChange (128C:129C)
log2FoldChange (128C:130N)
log2FoldChange (126:127C)
log2FoldChange (126:128N)
F
ROC analysis
True-positive fraction
(plasma membrane)
False-positive fraction
(nuclear+mitochondiral+cytosolic)
Cut-off Rank: 833
126:127C
G
Gene Ontology: Cellular Component
Cellular Component
Membrane
Plasma membrane
Cell periphery
Cellular anatomical entity
Endomembrane system
-log10(False Discovery Rate)

Figure 1: Glial Cell-Surface Proteomics of the Intact Brains of Young and Old Flies.
A: Transgenic expression of HRP fused to the transmembrane protein CD2 targets CD2-HRP to the extracellular side of the glial plasma membrane. In the presence of H_2O_2, CD2-HRP converts BxxP substrate into phenoxyl radicals that biotinylate nearby endogenous proteins. Biotinylated proteins are then enriched from brain lysates using streptavidin beads, followed by on-bead trypsin digestion, TMT labeling, and liquid chromatography-tandem mass spectrometry analysis (LC-MS/MS).
B: To confirm HRP-dependent biotinylation of glial cells, *Repo-GAL4* were crossed with either *UAS-HRP-CD2* or wildtype (w1118) flies and adult brains were stained with neutravidin. Proteins were biotinylated in the experimental group (*UAS-HRP-CD2*) but not in the control group (w1118).
C: Biochemical characterization by streptavidin blot showed that the glial cell-surface-targeted HRP biotinylated a wide range of proteins compared to the negative control lacking HRP-CD2 expression.
D: For each time point (5d and 50d), two biological replicates and two negative controls (one lacking HRP-CD2 expression and one lacking H_2O_2 in the reaction) were profiled. In total, we detected 2,007 proteins with two or more unique peptides. Potential contaminants were removed by comparing differential enrichment between the experimental and negative control groups (i.e., the TMT ratio for each protein identified; see Methods).
E: Strong correlations between biological replicates were observed, further validating the quality of the proteome profiles.
F: The receiver operating characteristic (ROC) curve depicts the true-positive rate against the false-positive rate of detected proteins, for each biological replicate (only 126:127C pictured).
G: Gene Ontology (GO) analysis was performed based on the 872 proteins identified following ratiometric and cutoff (see Methods). Top 5 GO terms on cellular compartments with the lowest false discovery rates are shown.

Quantitative comparison of young and old proteomes

We applied this modified cell-surface biotinylation methodology to the glial cells of young (5-day) and old (50-day) *Drosophila* to investigate how glial cell-surface proteomes change as flies age. To focus on glial cells in the central brain, we removed the optical lobes during sample preparation. To obtain sufficient cell-surface proteins for downstream mass spectrometry analysis, we dissected 300 fly brains for each sample (for a total of 2,400 brains, see below). To better quantify changes in the glial cell-surface proteome and filter out any contaminants captured in the negative controls, we used an 8-plex tandem mass tag (TMT)-based quantitative strategy (Thompson et al., 2003; Li et al., 2020). We profiled two biological replicates and two negative controls (one lacking HRP-CD2 expression and one lacking H_2O_2 in the reaction) for each time point (5d and 50d) (**Fig. 1D**). This allowed us to capture endogenously biotinylated proteins, as well as non-specific binders to streptavidin beads. Freshly dissected intact central brains were incubated with the BxxP substrate for one hour before a 5-minute H_2O_2 reaction. Biotinylated proteins were then enriched from brain lysates using streptavidin beads, followed by on-bead trypsin digestion, TMT labeling, and liquid chromatography-tandem mass spectrometry analysis (LC-MS/MS).

From this 8-plex experiment, we detected a total of 2,007 proteins with 2 or more unique peptides (**Fig. 1D**; Supplementary Table 1) and observed strong correlations between the replicates of each time point (5d and 50d), validating the quality of the proteome profiles (**Fig. 1E**). By comparing differential enrichment between the experimental and negative control groups (i.e., the TMT ratio for each protein), we were able to remove potential contaminants via ratiometric and cutoff analyses (Hung et al., 2014; Li et al., 2020). If a protein had a high TMT ratio, it was considered a true positive (TP), as a high TMT ratio indicates that that protein was extensively biotinylated in the experimental group, but not in the control group. Alternatively, a protein was considered a false positive (FP) if it had a low TMT ratio, as that indicates that protein was similarly biotinylated in both the experimental and the control groups. To calculate the TMT ratios, we paired one biological replicate with one control, as depicted in Fig. 1D.

To determine optimal TMT cutoff values, we plotted the receiver operating characteristic (ROC) curve for each biological replicate (**Fig. 1F**; **Fig. S1B**), which depicts the true-positive rate against the false-positive rate of detected proteins (Li et al., 2020; Nahm, 2022). To maximize the signal-to-noise ratio of the proteomes, each biological replicate was cut off at the position where the value of *true-positive rate (i.e., sensitivity) – false-positive rate (i.e., specificity)* was maximized (described in more detail in the Methods). To further minimize potential contaminants, we selected only TP proteins that overlapped in both biological replicates at each time point (**Fig. 1D**).

In total, we identified 872 proteins following our ratiometric and cutoff analyses, which exhibited high spatial specificity (as seen from the cellular component Gene Ontology (GO) analysis) (**Fig. 1G**). FlyBase, UniProt, and Gene Ontology Data Archive (DOI 10.5281/zenodo.1205166; Version 2023-05-10; Ashburner et al., 2000) were then searched to determine if each of the 872 proteins had plasma membrane and extracellular matrix annotations. We found that of the 872 proteins identified, 682 could be validated by at least one of these databases, further validating the spatial specificity of our cell-surface proteomic labeling (**Fig. S1A**).

Age-related changes in glial cell-surface proteomes

Of the 872 proteins identified by our glial cell-surface proteomics, we found that 127 were unique to young (5d) flies, 216 were unique to old (50d) flies, and 529 were found in both. This suggests that the cell-surface proteomes of glial cells do in fact shift as flies age; as such, we further compared the glial cell-surface proteomes of young and old flies (**Fig. 2A**).

To investigate how old glial cell-surface proteomes change in terms of their biological functions, we performed a GO analysis of genes encoding the most up- and down-regulated proteins. These proteins were selected from the original 872 identified (rather than from the 682 validated by the FlyBase, UniProt, or Gene Ontology Data Archive databases). This was done to ensure we included any potentially important uncharacterized proteins (see Methods). We next plotted the top five retrieved GO terms on biological processes with the lowest false discovery rates (**Fig. 2B**) (Szklarczyk et al., 2023). We found that while most up-regulated genes were associated with cell localization, transport, and homeostasis, most down-regulated genes were

associated with neural circuit development, synaptic wiring, and neuroplasticity, suggesting a possible decline in glia-neuron communication as flies age.

Next, we clustered these proteins by their reported protein-protein interactions and corresponding confidence scores using a Markov clustering algorithm (inflation value set at 2.5) (**Fig. 2C**). FlyBase and UniProt were then referenced to determine if each protein in the protein-protein interaction (PPI plot) had previously reported functions in synapse organization, synapse regulation, cell adhesion, development, or localization and transport.

Consistent with the biological functions identified by our GO analyses, we found that PPI clusters for synapse organization, synapse regulation, cell adhesion, and localization/transport were composed primarily of proteins enriched at the same time point, as seen by separately clustered blue or red nodes (**Fig. 2D**). For example, while most nodes in the synapse organization cluster were found to be downregulated in old fly brains, most nodes in the localization and transport cluster were found to be upregulated. Previous studies have found that communities of co-expressed proteins can be linked to disease processes, and that the most strongly correlated proteins or 'hubs' within these co-expression modules are often enriched in key drivers of disease pathogenesis (Johnson et al., 2020). As such, we identified the top 10 "hub" genes in our PPI network (**Fig. S1C**). We found that of the top 10 hub genes identified, 7 had reported function in cell adhesion (klg, kst) and synaptic wiring (DIP-β, DIP-δ, DIP-**γ**, DIP-κ, DIP-α), while the remaining three had reported function in neuron projection (CG33543), axon guidance (CG34353), and dendrite guidance (Toll-6).

To select candidates predicted to be involved in brain aging for functional screening, we identified genes associated with the largest fold-changes in protein levels between time points (5d and 50d) (**Fig. 2A**). Candidate genes were selected for functional screening only if they were known (or predicted) to be located either on the cell-surface or in the extracellular space. In total, we selected 48 candidate genes for functional screening, most of which were known to have at least one strong human ortholog (Supplementary Table 2) (Wang et al., 2017; Wang et al., 2019a; Wang et al. 2019b). Notably, we found that many of these candidates were cell adhesion and neural wiring molecules not previously thought to be particularly active in glia (**Fig. 2B-C**). Interestingly, our final list of candidates included 9 previously uncharacterized proteins (CG genes as Computated Genes), suggesting that future investigations of these proteins may reveal new facets of glial physiology.

Figure 2

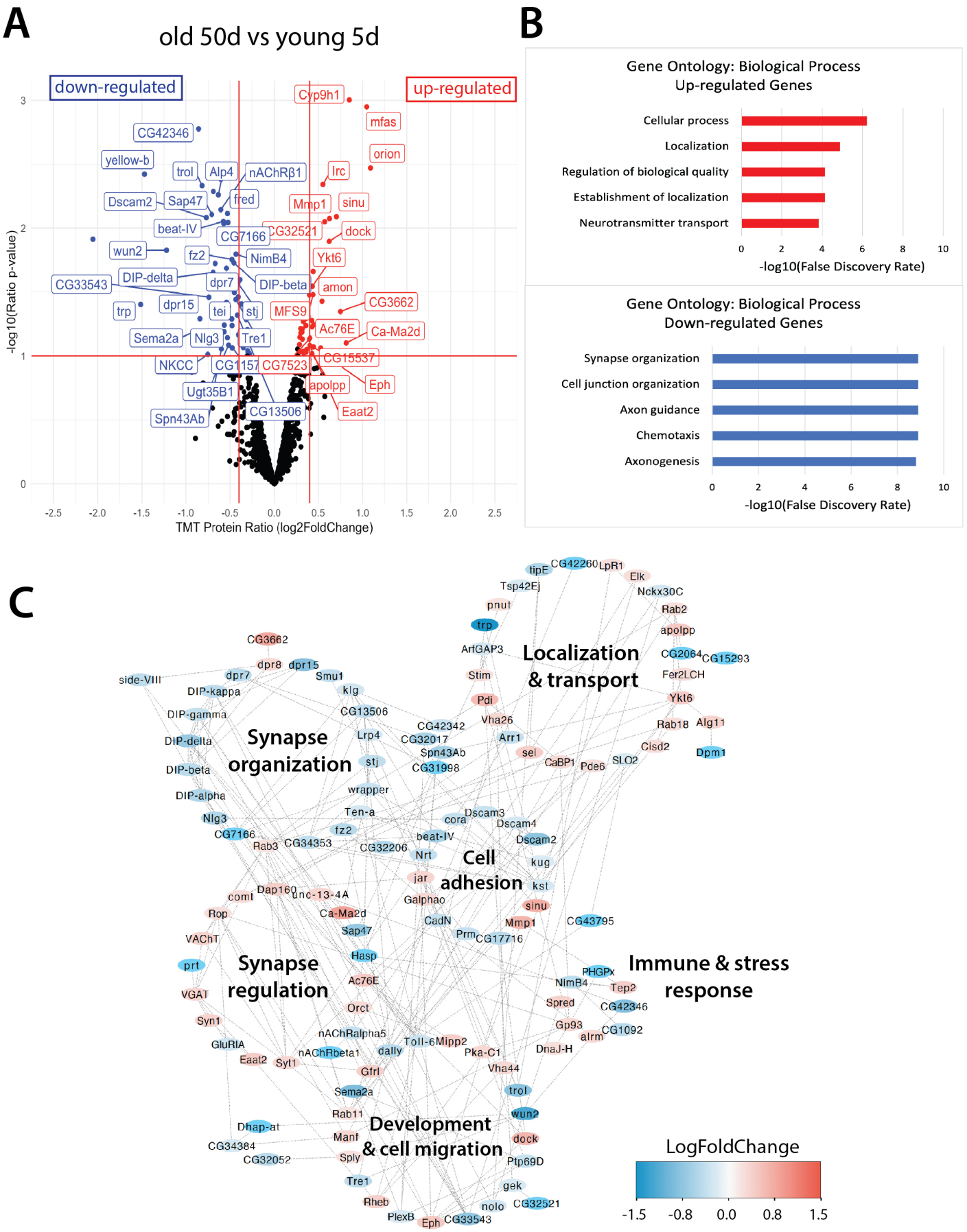
A
old 50d vs young 5d
down-regulated
up-regulated
-log10(Ratio p-value)
TMT Protein Ratio (log2FoldChange)
Cyp9h1
mfas
orion
Irc
Mmp1
sinu
dock
CG32521
Ykt6
amon
CG3662
MFS9
Ac76E
Ca-Ma2d
CG15537
CG7523
apolpp
Eph
Eaat2
CG42346
yellow-b
trol
Alp4
nAChRβ1
Dscam2
Sap47
fred
beat-IV
CG7166
wun2
fz2
NimB4
CG33543
DIP-delta
dpr7
DIP-beta
trp
dpr15
tei
stj
Sema2a
Nlg3
Tre1
NKCC
CG1157
Ugt35B1
Spn43Ab
CG13506
B
Gene Ontology: Biological Process
Up-regulated Genes
Cellular process
Localization
Regulation of biological quality
Establishment of localization
Neurotransmitter transport
-log10(False Discovery Rate)
Gene Ontology: Biological Process
Down-regulated Genes
Synapse organization
Cell junction organization
Axon guidance
Chemotaxis
Axonogenesis
-log10(False Discovery Rate)
C
Localization & transport
Synapse organization
Cell adhesion
Synapse regulation
Immune & stress response
Development & cell migration
LogFoldChange
-1.5
-0.8
0.0
0.8
1.5

Figure 2: Quantitative comparison of young and old proteomes and selection of candidate genes.
A: Genes encoding proteins associated with the largest old/young fold changes were identified and 48 candidate genes were selected for functional screening. Down-regulated candidate genes selected for functional screening are labeled in blue whereas up-regulated candidate genes are labeled in red.
B: A Gene Ontology (GO) analysis investigating proteome biological processes revealed that genes encoding the most up-regulated proteins were primarily associated with cell localization, transport, and maintaining homeostasis, while most down-regulated proteins were primarily associated with neural development, synapse organization, and neuroplasticity.
C: Genes encoding the most up- and down-regulated proteins were clustered by their reported protein-protein interactions (PPIs) and corresponding confidence scores (using a Markov clustering algorithm, inflation value set to 2.5). Each protein in the PPI plot was then assessed individually to determine if it had reported function in synapse organization, synapse regulation, cell adhesion, development and cell migration, or localization and transport.

Functional screening of candidate genes predicted to be involved in normal brain aging

To investigate the potential contribution of each candidate gene to normal brain aging, we conducted a broadscale, unbiased lifespan screen, as previous work has found that brain aging (i.e., age-related neurodegeneration) and lifespan are highly correlated (Mattson et al., 2002; Mattson and Arumugam, 2018). Importantly, several studies have shown that improving brain health can extend lifespan in *Drosophila* (Woodling et al., 2020; Schmid et al., 2022). For our lifespan screen, we used a pan-glial GeneSwitch-GAL4 driver (glial-GS hereafter) (Nicholson et al., 2008). GeneSwitch-GAL4, a modified, drug-inducible version of the GAL4 system, allows for both spatial and temporal control of transgene expression, which is induced by the drug mifepristone (also known as Ru486) (**Fig. 3A**) (Osterwalder et al., 2001; Nicholson et al., 2008). This allowed us to compare flies from the same genetic background after development was complete, ensuring that our gene manipulations were occurring as flies aged and not during key developmental milestones (Osterwalder et al., 2001). Ultimately, this improved the likelihood that any observed lifespan changes could be attributed to the gene manipulations themselves, rather than unintended developmental defects.

For each of the 19 up-regulated candidate genes, we screened 2 RNAi transgenic lines to control for potential off-target effects (**Fig. 3B**; RNAi lines used for each gene are detailed in Supplementary Table 3) (Dietzl et al., 2007; Ni et al., 2011; Perkins et al., 2015). For each down-regulated candidate gene, we screened one over-expression transgenic line (**Fig. 3B**; Supplementary Table 3), using either UAS-cDNA lines or flySAM2.0 lines. flySAM is a CRISPRa (CRISPR activation) system used in *Drosophila* to activate gene expression (Jia et al., 2018). flySAM2.0, an updated and simplified version of flySAM, increases experimental efficiency by combining UAS-dCas9 and sgRNA in the same transgenic fly, so that any flySAM2.0 lines can be directly crossed with a GAL4 line (Jia et al., 2018). For the down-regulated genes, we were able to acquire and screen lines for 19 of the 29 candidate genes (**Fig. 3B**).

First, we confirmed that the glial-GS line only induced transgene expression in the presence of the inducible drug Ru486. We found that the glial-GS drove *UAS-CD8-GFP* expression in the presence of the inducible drug Ru486, but not in the presence of the control (**Fig. 3A**), consistent with the previous study (Nicholson et al., 2008). Next, we crossed the glial-GS line with several control lines (a w1118 wildtype control, a UAS-luciferase RNAi control, a UAS-lacZ control, and a flySAM control). Importantly, we did not find an effect of the Ru486 drug itself on control lifespan (**Fig. 3C; Fig. 4A-B; Fig. S2A-B**).

We observed sex-specific lifespan effects for many of these screened genes. Of the 19 up-regulated genes that were screened, we found that RNAi knockdown of 3 genes (*Ca-Ma2d, orion, sinu*) led to consistent increases in lifespan for females but not for males (**Fig. 3D-E; Fig. S3-6**). We also found that RNAi knockdown of 4 genes (*dock, Eaat2, Eph, Ykt6*) led to consistent decreases in lifespan for males (i.e., lifespan decreases were observed for both RNAi lines used), but inconsistent lifespan changes were observed for females (**Fig. 3D-E; Fig. S3-6**). Interestingly, we did not find any RNAi lines that increased lifespan for both males and females. Of the 19 down-regulated genes that were screened, we found that overexpression of *Nlg3* led to increases in lifespan for males, but not for females, whereas overexpression of 3 genes (*CG42346, NimB4, and Sap47*) led to lifespan decreases for males, but lifespan increases for females (**Fig. 3D, 3F; Fig. S7-8**). Alternatively, we found that overexpression of 6 genes (*beat-IV, CG33543, dpr7, Dscam2, fred*, and *NKCC*) led to increases in lifespan for females, but observed no changes in lifespan for males (**Fig. 3D, 3F; Fig. S7-8**). These sex-specific differences in lifespan is an interesting subject for future validation and investigation. Next, we focused on DIP-β, which was the only candidate gene associated with consistent increases in lifespan for both male and female flies (**Fig. 4C-D**).

Figure 3

A

glial-GeneSwitch (GS) > UAS-GFP

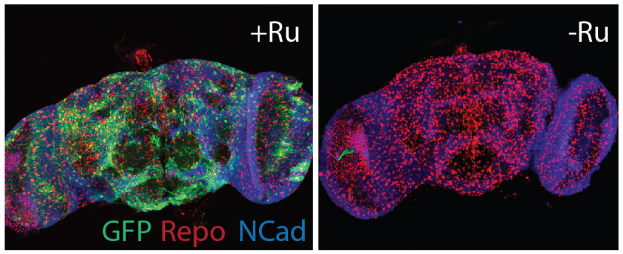

B

lifespan screen

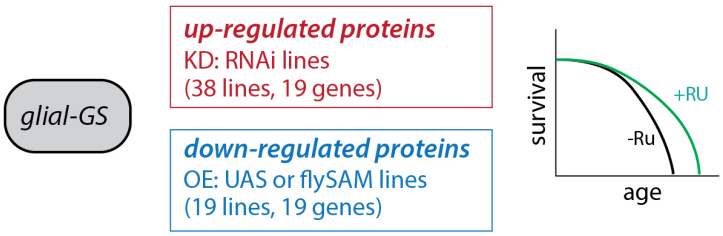

C

Control Line	Males		Females	
	median change	p-value	median change	p-value
w1118	4.11%	0.13	2.63%	0.24
lucRNAi	0%	0.71	3.75%	0.07
UAS-lacZ	0%	0.72	-2.53%	0.34
flySam control THI 2432.S	-8.86%	0.06	7.14%	0.93

D

lifespan summary

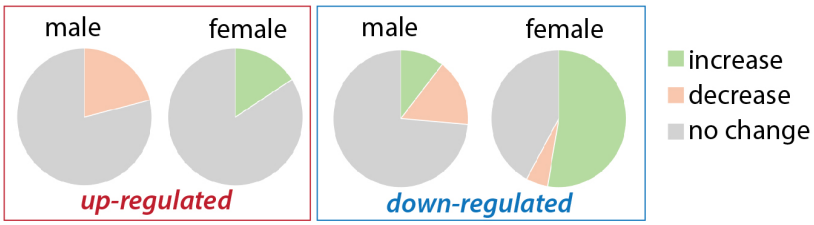

E

Candidate Gene	RNAi #1				RNAi #2			
	Males		Females		Males		Females	
	median change	p-value	median change	p-value	median change	p-value	median change	p-value
Ac76E	-5.36%	0.91	-2.78%	0.16	0%	0.56	36.96%	<0.001
amon	0%	0.04	0%	0.98	-6.94%	0.06	17.39%	<0.001
apolpp	0%	0.41	2.60%	0.01	9.43%	0.004	2.78%	0.001
Ca-Ma2d	-6.58%	0.001	8.97%	<0.001	-3.39%	0.29	12.70%	<0.001
CG15537	3.28%	0.06	2.86%	<0.001	-4.92%	0.67	-10.67%	0.001
CG32521	3.85%	0.01	7.81%	0.051	-9.09%	<0.001	0%	0.001
CG3662	0%	0.26	7.81	0.051	-2.78%	0.19	2.56	<0.001
CG7523	7.81%	<0.001	16.42%	<0.001	-2.78%	0.75	2.78	0.001
Cyp9h1	2.82%	0.54	7.04	<0.001	-4.41%	0.44	2.60%	0.04
dock	-9.09%	<0.001	-3.70%	0.07	-17.31%	<0.001	8.47%	0.01
Eaat2	-14.49%	<0.001	5.56%	0.002	-5.41%	0.002	-2.47%	0.47
Eph	-7.94	<0.001	-3.66%	0.06	-6.15%	0.03	18.03%	<0.001
Irc	-2.99%	0.002	9.72%	<0.001	0%	0.48	0%	0.2
mfas	0%	0.49	3.80%	<0.001	-3.03%	0.85	2.56%	0.02
MFS9	-3.13%	0.51	6.85%	0.6	0%	0.36	21.62%	<0.001
Mmp1	-2.82%	0.02	6.41	0.74	-3.51%	0.01	22.92%	0.004
orion	0%	0.06	8.82%	<0.001	-3.45%	0.32	7.46%	0.003
sinu	-4.55%	<0.001	10.96%	0.001	-13.43%	<0.001	11.11%	<0.001
Ykt6	-8.82%	<0.001	32.56%	<0.001	-22.58%	<0.001	-14.81%	<0.001

F

Candidate Gene	flySam/UAS line			
	Males		Females	
	median change	p-value	median change	p-value
beat-IV	-2.78%	0.73	17.91%	<0.001
CG13506	-8.06%	0.07	-12.33%	<0.001
CG33543	0%	0.31	25%	<0.001
CG42346	-10.77%	<0.001	7.46%	<0.001
DIP-beta	11.11%	<0.001	14.89%	<0.001
DIP-delta	-2.82%	0.89	0%	0.62
dpr7	0%	0.44	10.45%	0.02
Dscam2	3.08%	0.65	6.76%	<0.001
fred	0%	0.15	29.63%	<0.001
fz2 *	-3.51%	0.23	3.13%	0.001
NimB4	-10%	0.002	10%	<0.001
NKCC	0%	0.64	7.14%	<0.001
Nlg3	30.77%	<0.001	-3.7%	0.99
Sap47	-15.78%	<0.001	5.41%	0.001
Sema2a *	0%	0.2	0%	0.99
Spn43Ab	0%	0.18	0%	0.81
stj *	5.77%	0.57	7.14%	0.27
trol *	0%	0.51	2.56%	0.18
yellow-b	0%	0.01	0%	0.002

* UAS lines others, flySAM lines

Figure 3: Functional screening of candidate genes predicted to be involved in normal brain aging.
A: Confocal images showing that the glial-GS line only induced transgene expression in the presence of the inducible drug Ru486.
B: 48 candidate genes were selected for functional screening. For each of the 19 up-regulated genes, two RNAi lines were used to control for possible off target effects. Of the 29 down-regulated genes selected, we were able to acquire and screen lines for 19 genes.
C: No obvious lifespan effect was observed in control lines: a w1118 wildtype control, a UAS-luciferase RNAi control, a UAS-lacZ control, and a flySAM control.
D: Pie charts summarizing the results of our broadscale lifespan screen for male and female flies.
E: Of the 19 up-regulated candidate genes screened, RNAi knockdown of 4 genes led to consistent lifespan decreases for males. Alternatively, RNAi knockdown of 3 genes led to consistent lifespan increases for females.
F: Of the 19 down-regulated candidate genes screened, overexpression of 2 genes led to lifespan increases for males, whereas overexpression of 3 genes led to lifespan decreases. In parallel, overexpression of 10 genes led to lifespan increases for females, whereas overexpression of 1 gene led to decreased lifespan.

Validating that glial overexpression of DIP-β increases lifespan

Following our functional screen, we identified DIP-β as the most promising candidate for further investigation. Interestingly, DIP-β was also identified as the top-ranked “hub” gene in our PPI analysis of the most up- and down-regulated genes (**Fig. S1C**).

To validate these initial findings, we conducted two additional lifespan trials, again using the DIP-β flySAM line to overexpress DIP-β in glia. We observed consistent increases in lifespan across DIP-β flySAM lifespan trials. Next, we conducted two more lifespan trials, this time using a UAS-DIP-β line to overexpress DIP-β in glia. Again, we observed consistent increases in lifespan across UAS-DIP-β lifespan trials (**Fig. 4D**). Combined, these data indicate that the lifespan increases observed when DIP-β is overexpressed in glial cells are likely due to the gene manipulations themselves.

Next, we conducted climbing (i.e., negative geotaxis) assays, as motor control and climbing ability are commonly considered reliable phenotypic indicators of brain aging and age-related neurodegeneration (Barone and Bohmann, 2013; Beharry et al., 2013; Manjila and Hasan, 2018). We found that pan-glial overexpression of DIP-β was also associated with improved climbing and motor control ability in aged flies for both males and females. Altogether, these results indicate that DIP-β can play an important role in maintaining healthy brain function and delaying phenotypes associated with age-related neurodegeneration.

Figure 4

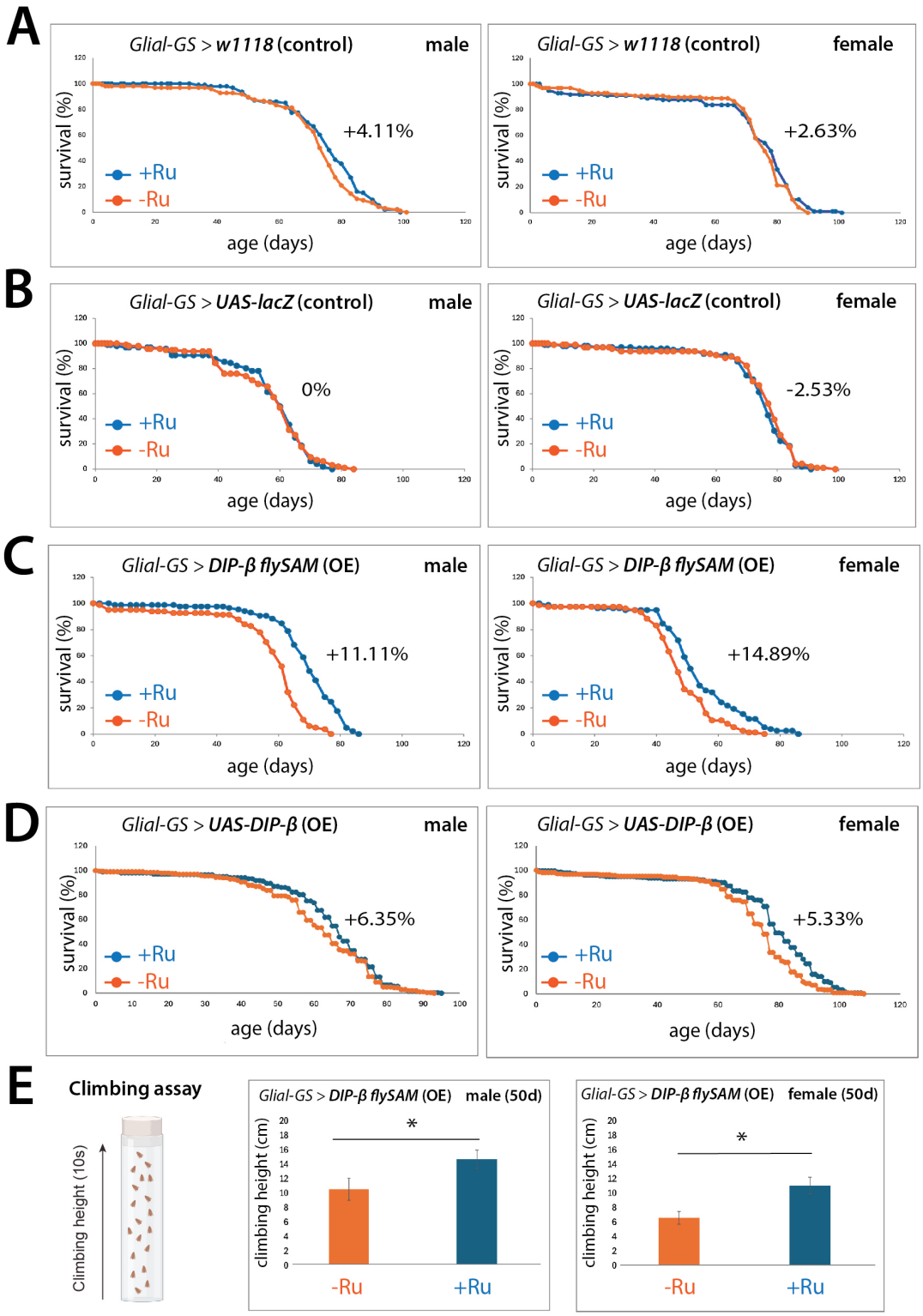
A
Glial-GS > w1118 (control)
male
+4.11%
Glial-GS > w1118 (control)
female
+2.63%
B
Glial-GS > UAS-lacZ (control)
male
0%
Glial-GS > UAS-lacZ (control)
female
-2.53%
C
Glial-GS > DIP-β flySAM (OE)
male
+11.11%
Glial-GS > DIP-β flySAM (OE)
female
+14.89%
D
Glial-GS > UAS-DIP-β (OE)
male
+6.35%
Glial-GS > UAS-DIP-β (OE)
female
+5.33%
survival (%)
age (days)
+Ru
-Ru
E
Climbing assay
Climbing height (10s)
Glial-GS > DIP-β flySAM (OE) male (50d)
Glial-GS > DIP-β flySAM (OE) female (50d)
climbing height (cm)
*
-Ru
+Ru

Figure 4: Validating that pan- glial overexpression of DIP-β increases lifespan and serves a protective function during aging.
A-C: Glial overexpression of DIP-β (flySam 2.0 line) significantly extends lifespan for both male and female flies, compared to the negative controls (only the w1118 and UAS-lacZ controls are shown here).
D: Glial overexpression of DIP-β (UAS-cDNA line) significantly extends lifespan for both male and female flies
E: To further validate that glial overexpression of DIP-β is serving a protective function during brain aging, climbing (i.e., negative geotaxis) assays were conducted. Glial overexpression of DIP-β was also associated with improved climbing and motor control ability in aged flies.

Investigating the downstream transcriptomic effects of overexpression of DIP-β in glial cells during aging

To investigate the downstream transcriptomic effects of upregulating glial expression of DIP-β as flies age, we conducted single-nucleus RNA sequencing (snRNA-seq). To do this, we prepared two whole-head samples collected from old (50d) flies: one where DIP-β had been overexpressed in glia from day 5-50 and one where DIP-β expression had not been manipulated (**Fig. 5A**).

For our snRNA-seq, we used the DIP-β flySAM 2.0 to overexpress DIP-β in glia (as opposed to the UAS-DIP-β line), as we consistently observed stronger lifespan-extension effects for the flySAM line. Additionally, we chose to sequence the heads of female flies, as we consistently observed stronger lifespan-extension effects for females. Sequencing whole-head samples allows for detailed profiling of glia, neurons, and other related cell types and subtypes (including fat cells, muscle, trachea, epithelial cells, etc.). As such, this enables us to form a more comprehensive understanding of global changes across the entire fly head (as previously demonstrated in our Aging Fly Cell Atlas (Lu et al., 2023) and Alzheimer's Disease Fly Cell Atlas (Park et al., 2025).

In total, we obtained 48,959 high-quality cells after the quality control steps: ~23,000 from the DIP-β overexpression (i.e., Ru486+) sample and ~26,000 from the control (i.e., Ru486-) sample (**Fig. 5B**). Based on our Fly Cell Atlas cell annotations (Li et al., 2022), these cells were annotated into 8 broad cell types (CNS neurons, sensory neurons, glia, fat cells, hemocytes, muscle, trachea, and epithelial cells) and 96 detailed cell subtypes (**Fig. S9**).

First, we compared broad cell type compositions between the DIP-β overexpression and the control samples. We found that broad cell type compositions were largely consistent between the two groups (**Fig. 5C**), suggesting that DIP-β overexpression does not change cell ratios within the head. Next, we analyzed differentially expressed genes (DEGs) for each of the 8 broad cell types. We found that glial cells exhibited the second highest number of DEGs after fat cells (**Fig. 5D**). Further analysis of DEGs across 96 detailed cell subtypes revealed that cortex glia (i.e., "adult brain cell body glia") and ensheathing glia were among the top affected cell subtypes (**Fig.**

448 **5E**). Between these two glial subtypes, 186 DEGs were unique to cortex glia, 27 were unique to
449 ensheathing glia, and 40 were found in both cortex glia and ensheathing glia (**Fig. 5F**).
450
451 As fat cells exhibited the highest number of DEGs between the glial DIP-β overexpression
452 and control samples, we conducted a KEGG pathway analysis to evaluate the biological functions
453 of these genes (**Fig. 5G**) (Chen et al., 2017). We found that fat cells showed more up-regulated
454 DEGs than down-regulated ones, and that the top altered metabolic and signaling pathways for
455 these up-regulated genes were related to homeostasis, signal integration, stress resistance, and
456 longevity (**Fig. 5G**). Interestingly, these results are consistent with our previous findings that fat
457 cells are often among the cell types found to be most sensitive to changes related to aging and
458 neurodegeneration (Lu et al., 2023; Park et al., 2025).
459
460 Next, we conducted a cell-cell communication (CCC) analysis to evaluate how glial
461 overexpression of DIP-β impacts cell-cell signaling pathways during normal brain aging (**Fig. 5H**)
462 (Wilk et al., 2024). To do this, we employed the FlyPhoneDB2 that we recently developed (Qadiri
463 et al., 2025). FlyPhoneDB2 is a computational platform for analyzing cell-cell communication in
464 *Drosophila* snRNA-seq data using curated ligand-receptor pairs. By aggregating and comparing
465 ligand-receptor expression values for various groups of cells, we were able to infer which groups
466 of cells are likely interacting with glia and which ligand-receptor pairs are contributing to the glial-
467 other cell communication changes. We found that DIP-β overexpression was generally associated
468 with an increase in cell-cell communication compared with the aged control, particularly glia-
469 neuron and glia-fat cell communication (**Fig. 5H**). We found that the top altered glial signaling
470 pathways include TGF-beta, WNT, FGFR, and EGFR signaling pathways (**Fig. 5H**).
471
472 Combined, these results suggest that glial overexpression of DIP-β leads to improved glia-
473 neuron and glia-fat cell communication as flies age, which may be contributing to the observed
474 lifespan extensions through multiple signaling pathways (**Fig. 5I**). As such, it will be interesting to
475 investigate the molecular mechanisms underlying how DIP-β overexpression leads to these
476 signaling changes, how DIP-β's binding partners (multiple cell-surface Dpr proteins, see
477 Discussion) are involved, and which downstream pathways play key roles in mediating the
478 lifespan extension in future studies.
479
480

Figure 5

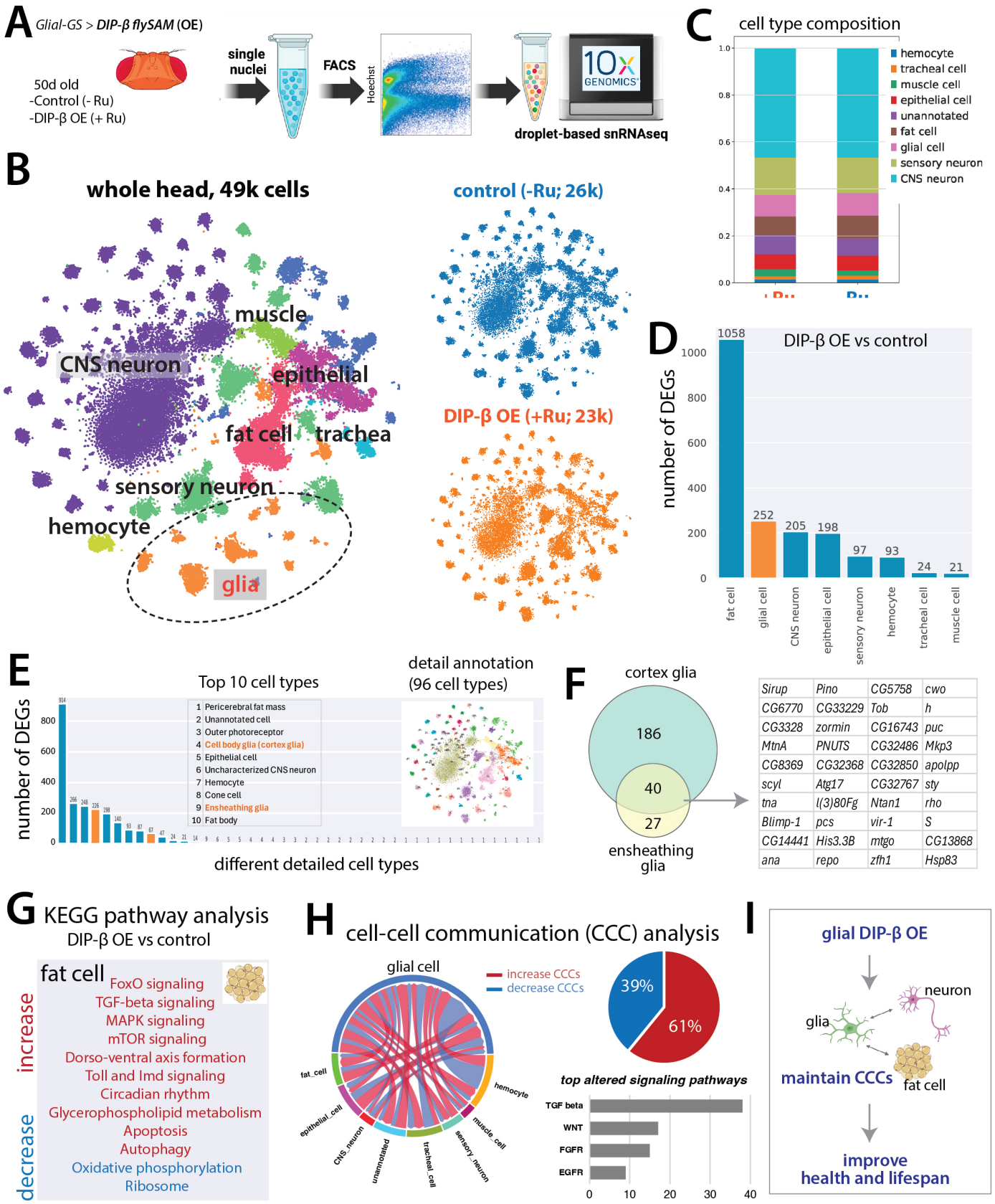
A
Glial-GS > DIP-β flySAM (OE)
50d old
-Control (- Ru)
-DIP-β OE (+ Ru)
single nuclei
FACS
Hoechst
10x GENOMICS
droplet-based snRNAseq
B
whole head, 49k cells
muscle
CNS neuron
epithelial
fat cell
trachea
sensory neuron
hemocyte
glia
control (-Ru; 26k)
DIP-β OE (+Ru; 23k)
C
cell type composition
hemocyte
tracheal cell
muscle cell
epithelial cell
unannotated
fat cell
glial cell
sensory neuron
CNS neuron
D
DIP-β OE vs control
number of DEGs
1058
252
205
198
97
93
24
21
fat cell
glial cell
CNS neuron
epithelial cell
sensory neuron
hemocyte
tracheal cell
muscle cell
E
Top 10 cell types
detail annotation (96 cell types)
number of DEGs
1 Pericerebral fat mass
2 Unannotated cell
3 Outer photoreceptor
4 Cell body glia (cortex glia)
5 Epithelial cell
6 Uncharacterized CNS neuron
7 Hemocyte
8 Cone cell
9 Ensheathing glia
10 Fat body
different detailed cell types
F
cortex glia
186
40
27
ensheathing glia
Sirup Pino CG5758 cwo
CG6770 CG33229 Tob h
CG3328 zormin CG16743 puc
MtnA PNUTS CG32486 Mkp3
CG8369 CG32368 CG32850 apolpp
scyl Atg17 CG32767 sty
tna l(3)80Fg Ntan1 rho
Blimp-1 pcs vir-1 S
CG14441 His3.3B mtgo CG13868
ana repo zfh1 Hsp83
G
KEGG pathway analysis
DIP-β OE vs control
fat cell
increase
FoxO signaling
TGF-beta signaling
MAPK signaling
mTOR signaling
Dorso-ventral axis formation
Toll and Imd signaling
Circadian rhythm
Glycerophospholipid metabolism
decrease
Apoptosis
Autophagy
Oxidative phosphorylation
Ribosome
H
cell-cell communication (CCC) analysis
glial cell
increase CCCs
decrease CCCs
fat_cell
epithelial_cell
CNS_neuron
unannotated
tracheal_cell
sensory_neuron
muscle_cell
hemocyte
39%
61%
top altered signaling pathways
TGF beta
WNT
FGFR
EGFR
0
10
20
30
40
I
glial DIP-β OE
neuron
glia
maintain CCCs
fat cell
improve health and lifespan

Figure 5: Single-nucleus RNA-sequencing - investigating the downstream transcriptomic effects of glial overexpression of DIP-β during aging.

A: Two whole-head samples (20 heads each) were prepared for snRNA-seq: one where DIP-β had been overexpressed in glia from day 5-50 and one control. Single-nucleus RNA-seq libraries were prepared using the 10X Genomics Chromium Single Cell 3' HT v3.1 protocol.

B: In total, approximately 49,000 high-quality cells were obtained after quality control and filtering from our fly head samples, which consist of 8 broad cell types.

C: Broad cell-type cluster compositions were largely consistent between the glial DIP-β overexpression treatment (Ru486+) and the control (Ru486-) groups.

D: A broad analysis of differentially expressed genes (DEGs) revealed that the glial cell-type cluster showed the second highest number of DEGs between the glial DIP-β overexpression treatment (Ru486+) and the negative control (Ru486-) groups.

E: A more detailed analysis investigating DEGs across 90 different cell subtypes revealed that of the glial cell subtypes, cortex glia (i.e., "adult brain cell body glia") and ensheathing glia showed the highest number of DEGs between the DIP-β overexpression treatment (Ru486+) and the control (Ru486-) groups.

F: Of the 252 DEGs identified for glial cells, 186 were unique to cortex glia, 27 were unique to ensheathing glia, and 40 were found to be differentially expressed in both cortex and ensheathing glia.

G: As fat cells exhibited the highest number of DEGs between the DIP-β overexpression and control groups, we conducted a KEGG analysis to evaluate the biological functions of these genes. Most fat cell DEGs were up-regulated, and the top altered metabolic and signaling pathways for these genes were found to be related to homeostasis, signal integration, stress resistance, and longevity.

H: Cell-cell communication (CCC) analysis was performed using FlyPhoneDB2. DIP-β overexpression was generally associated with an increase in cell-cell communication, particularly glia-neuron and glia-fat cell communication. The top altered glial signaling pathways are shown.

I: Our proposed model: Glial overexpression of DIP-β leads to improved glia-neuron and glia-fat cell communication as flies age, which may contribute to the observed lifespan extensions.

515 **Discussion**
516
517 Age-related changes in the cell-surface proteomes of glial cells are hypothesized to play
518 important roles in the dysregulation of glia-neuron interactions observed in brain aging (Barres,
519 2008; Kremer et al., 2017). However, these changes have not been previously characterized due
520 to technical limitations. Here, we adapted a platform to profile spatiotemporally resolved glial cell-
521 surface proteomes from intact brains in young and old *Drosophila* (Li et al., 2020). Our study
522 revealed global downregulation of synaptic wiring and cell adhesion molecules in the aged brain,
523 and identified several molecules not previously thought to be particularly active in glia. Additionally,
524 our study identified the neural wiring molecule DIP-β as a potential regulator of healthy brain
525 function during brain aging. Here, we explore how cell adhesion and synapse organization
526 molecules like DIP-β may be playing a role in age-related neurodegeneration.
527
528 In *Drosophila*, several superfamilies of cell adhesion molecules (CAMs) are known to
529 contribute to neural circuit organization (including cadherins, immunoglobulins, leucine-rich
530 repeat proteins, and teneurins) (Byron et al., 2010; Bulgakova et al., 2012; Sanes and Zipursky,
531 2020; Xu et al., 2024). While the mechanisms underlying precise neural wiring are not yet fully
532 understood, it is generally thought that each subset of neurons expresses a unique combination
533 of CAMs, which act as highly specified identification tags (Elmariah et al., 2005; Lin and Koleske,
534 2011; Silies and Klambt, 2011; Carrillo et al., 2015; Tan et al., 2015; Cosmanescu et al., 2018; Li
535 et al., 2020; Kim et al., 2020). Indeed, previous work has provided ample evidence in support of
536 this, demonstrating that neuronal cell subtypes often express the same groups of CAMs, and that
537 loss-of-function mutations in these molecules result in profound (and often predictable) neural
538 wiring defects (Carrillo et al., 2015; Wang et al., 2022; Ma et al., 2023). While many previous
539 studies have painstakingly delineated the contributions of various CAMs to precise synaptic wiring
540 in the developing brain, these molecules do not have a comparably well-defined role in the aging
541 brain (Lin and Koleske, 2010; Ma et al., 2023).
542
543 Global downregulation of synaptic wiring molecules, loss of cell identity, and diminished
544 synaptic connectivity are all considered hallmarks of age-related neurodegeneration (in both
545 normal brain aging, as well as in a wide variety of neurodegenerative diseases) (Lin and Koleske
546 2010; Li et al., 2020; Banerjee et al., 2021; Banerjee et al., 2024; Li et al., 2022). While most of
547 what glia do in the brain is thought to depend on their close physical relationship with neurons,
548 synapses, and other glial cells, we know surprisingly little about how glia precisely associate and
549 coordinate with their intended targets (Silies and Klambt, 2011; Freeman, 2015; Cho et al., 2018;
550 Bittern et al., 2021). For example, exactly how one cortex glial cell is able to accommodate the
551 unique needs of up to 100 neurons simultaneously remains one of the greatest mysteries in glial
552 cell biology (Hillen et al., 2018; Chen et al., 2024). Previous studies have demonstrated that at
553 least some CAMs play important roles in glia-neuron interactions (Grumet and Edelman, 1988;
554 Lepeta et al., 2016; Chou et al., 2020); for example, Neurexins and Neuroligins are known to help
555 coordinate astrocyte-synapse contact sites during synaptogenesis (Grumet and Edelman, 1988;
556 Lepeta et al., 2016; Chou et al., 2020; Chen et al., 2024). Additionally, CAMs have been found to
557 function in a range of other biological processes related to trans-synaptic signaling, including
558 synaptic vesicle organization, receptor clustering, and structural and functional plasticity (Chou et

al., 2020). However, we do not yet fully understand the role these CAMs may be playing in enabling glia to effectively interact with, support, and coordinate with other cells in the brain.

In *Drosophila*, heterophilic binding between members of two immunoglobulin sub-families, the 11-member DIP (Dpr interacting proteins) family and the 21-member Dpr (defective proboscis extension response) family, are known to regulate precise synapse organization (Carrillo et al., 2015; Tan et al., 2015; Cosmanescu et al., 2018; Xu et al., 2019; Honig and Shapiro, 2020; Sanes and Zipursky, 2020; Sergeeva et al., 2020; Wang et al., 2022; Ma et al., 2023). While DIPs and Dprs are best known for regulating precise synaptic wiring in the developing optic lobe, some studies have found that DIP/Dpr proteins also play important roles in the central adult brain (Carrillo et al., 2015; Wang et al., 2022; Ma et al., 2023). For example, one study found that similar to optic lobe neurons, dopaminergic and clock neurons express cell-subtype-specific combinations of DIP and Dpr proteins, and that cyclic expression of DIP-β in a small subset of clock neurons (small LNvs) plays an important role in sleep onset and duration in adult flies (Ma et al., 2023). As transcript cycling across the day has been well documented in clock neurons, it is possible that DIP-β may be playing a role in circadian-related changes in synaptic plasticity (Ahmad et al., 2021). In support of this, the human ortholog of DIP-β, IgLON5, is involved in processes related to neuroplasticity and neurogenesis, and is additionally suspected of playing a role in maintaining blood-brain barrier (BBB) integrity (Madetko et al., 2022; Zhang et al., 2023). Recently, IgLON5 was implicated in a rare autoimmune disease, anti-IgLON5, a condition that presents with several nonspecific symptoms, including sleep disturbances, gait abnormalities, and impaired cognitive function (Madetko et al., 2022; Zhang et al., 2023). Combined, these findings suggest that DIP-β may be playing important roles in neuroplasticity, sleep regulation, and BBB permeability.

Interestingly, we found that of the 32 DIP and Dpr proteins known in *Drosophila*, nine (DIP-β, DIP-δ, DIP-**γ**, DIP-κ, DIP-α, Dpr7, Dpr 8, Dpr12, Dpr 15) were included in our final cell-surface proteomes. Of these 9 proteins, four (DIP-β, DIP-δ, Dpr8, Dpr15) were also included in the 48 candidates selected for further screening, suggesting that these molecules likely play important roles in age-related neurodegeneration. Previous work has demonstrated that, in general, DIPs bind preferentially to Dprs (Sergeeva et al., 2020), and that while neurons typically express several Dprs, DIPs are expressed far more selectively (1-2 per neuron) (Cosmanescu et al., 2018; Wang et al., 2022). DIPs and Dprs have been found to display a broad range of binding affinities, as some bind heterophilically to one partner, others are more promiscuous, and a few bind homophilically (Cosmanescu et al., 2018; Sanes and Zipursky, 2020; Xu et al., 2019). Of the 11 DIP proteins, DIP-β has been found to display some of the strongest and most promiscuous binding affinities (i.e., DIP-β binds strongly to a broader range of Dprs, such as Dpr6, Dpr8, Dpr9, Dpr15, and Dpr21, than most other DIPs) (Cosmanescu et al., 2018; Sergeeva et al., 2020). This suggests that DIP-β may have the potential to interact with a broader range of neuronal cell types than other DIPs. While another down-regulated DIP (DIP-δ) was also included in our functional screen, we did not observe any lifespan increases when DIP-δ was overexpressed in glia. This could be because DIP-δ reportedly binds with only one Dpr (Dpr 12), and thus may be interacting with a narrower range of neurons (Honig and Shapiro, 2020).

As one of the best documented roles of glial cells is to facilitate controlled transport of nutrients and macromolecules, both into and out of individual neurons via the blood-brain barrier (BBB) (Artiushin et al., 2018; Moulton et al., 2021; Axelrod et al., 2023; Contreras and Klambt, 2023), our finding that upregulation of DIP-β in glia primarily impacts cortex and ensheathing glia is particularly interesting. Cortex glia are thought to facilitate the efficient transfer of nutrients from the hemolymph to neuronal cell bodies, whereas ensheathing glia clear debris from the neuropil (Hartenstein, 2011; Freeman, 2015). While previous work suggests that DIPs and Dprs are primarily expressed in neurons under normal conditions, it is possible that upregulating a CAM with particularly strong and promiscuous binding affinities in these cells may be sufficient to (at least partially) compensate for global downregulation of other endogenous CAMs. This hypothesis is further supported by our snRNA-seq results, which found that glial DIP-β overexpression was associated with increased cell-cell communication in aged flies. Altogether, our findings suggest that overexpressing DIP-β in glia may help preserve their ability to interact with and support their intended targets in the aging brain.

In summary, our study revealed that the maintenance of cell-cell communication and healthy brain function during aging relies on several previously unexpected cell-adhesion and synaptic wiring molecules. Our findings highlight the power of using *in-situ* cell-surface proteomics to capture the native complexity of proteomes that would otherwise be lost using more traditional proteomics methods. Further investigations of these CAMs (particularly DIP-β) will be instrumental for expanding our understanding of the mechanisms underlying how these molecules contribute to synaptic connectivity and the maintenance of healthy brain function during normal brain aging.

ACKNOWLEDGMENTS

We thank the Li lab members for their constructive advice on this project. We thank Dr. Chundi Xu for sharing the UAS-DIP-Beta fly line.

FUNDING

M.P.M. was supported by an Alzheimer's Association Research Fellowship (AARF-22-967413) and the CAND fellowship from Baylor College of Medicine for this work. T.J. is supported by the NIH F31 DK141194. N.P. is an investigator of the Howard Hughes Medical Institute and supported by NIH U01 AG086143, R24OD030002 and R24OD019847. L.L. is an investigator of the Howard Hughes Medical Institute and supported by NIH R01-DC005982. H.L. is a CPRIT Scholar in Cancer Research (RR200063), and supported by NIH U01 AG086143, NIH DP2AT013275, the Longevity Impetus Grant, the Ted Nash Long Life Foundation, the Welch Foundation, and the Hevolution/AFAR Foundation.

AUTHOR CONTRIBUTIONS

Conceptualization: M.M., H.L.
Fly experiments: M.M, E.H., O.P., A.V.
Cell-surface proteomics: J.L., H.L., L.L., N.D.U., D.K.C., D.R.M, S.A.C
Data analysis: M.M., B.S., M.C.W., T-C.L., M.Q., Y.H.
snRNA-seq: T.J., Y-J.P., Y.Q.
Transgenic fly: J.Z., N. P.
Writing: M.M., H.L.
Review and Editing: All authors.
Resources: L.L., K.V., H.L.
Supervision: H.L.
Funding Acquisition: H.L.

DECLARATION OF INTERESTS: The authors declare no competing interests.

Methods

Lead contact and materials availability

Further information and requests for resources and reagents should be directed to the Lead Contact, Hongjie Li (Hongjie.Li@bcm.edu). All unique reagents generated in this study are available from the Lead Contact.

Drosophila as a Model System

Drosophila have long been established as one of the best developed model species for studying nervous system biology (Freeman, 2015; Jourjine and Hoekstra, 2021). This is largely due to their short generation time, and to their powerful and extensive molecular genetics toolkit, which enables investigators to single out, manipulate, and quantitatively compare genetically and morphologically defined cell populations (Jourjine and Hoekstra, 2021). Ultimately, this allows investigators to carry out broadscale, unbiased screens of many cells and genes rapidly and affordably, after which the findings can be translated into mouse and human models. Additionally, *Drosophila* have proven a prime model system for studying aging and age-related diseases, as many key aging pathways are known to be conserved from flies to mammals (Giansanti and Piergentili, 2025; Park et al., 2025).

In *Drosophila*, glial cells follow neurons as the most abundant cell type in the brain and are thought to represent approximately 5-10% of the total population of cells within the fly central nervous system (CNS) (Freeman, 2015). A large body of work has found evidence that *Drosophila* glia share many morphological and functional similarities with mammalian glia, and that this conservation of basic glial cell biology extends to the molecular level (Freeman, 2015). In *Drosophila*, the CNS is composed primarily of three glial cell subtypes (cortex glia, ensheathing glia, and astrocyte-like glia), which fully envelope the CNS scaffold of neuron cell bodies, neurites, and synapses (Freeman, 2015). Recent studies have found that these CNS glial cells play several key roles in the *Drosophila* brain, including homeostasis, plasticity, neurodegeneration, etc. (Freeman, 2015).

Drosophila stocks and genotypes

All fly stocks were kept in a humidified, temperature controlled incubator at 25℃ with a 12:12 hour light/dark cycle (Bauer et al., 2004; Li et al., 2020). Fly stocks were housed in vials containing standard cornmeal medium and flipped to new food vials every 2-3 weeks. Standard cornmeal medium consisted of cornmeal, agar, inactive dry yeast, molasses (Genesee Scientific), and water, as well as nipagin (dissolved into 140-proof ethanol, Decon Labs) and propionic acid (Sigma Aldrich). In cases where larger numbers of flies of a certain genotype were required for experiments (such as our glial-GS line), flies were transferred to bottles containing standard cornmeal medium and flipped to new food bottles every 2-3 weeks. The following lines were used: w1118, UAS-luciferase RNAi, UAS-lacZ , Repo-GAL4, UAS-redStinger, UAS-CD4-GFP (Han et al., 2011), UAS-CD8-GFP (Lee and Luo, 1999), UAS-HRP-CD2 (Larsen et al., 2003), Atpalpha-GeneSwitch (Nicholson et al., 2008), UAS-DIP-β (Xu et al., 2019). All UAS and RNAi lines were generated previously (Xu et al., 2019) and acquired from the Bloomington *Drosophila* Stock Center and the Vienna *Drosophila* Resource Center (Supplementary Table 3). All flySAM overexpression and flySAM control lines were generated by the Perrimon Lab (Jia et al., 2018).

Glial cell-surface biotinylation in intact brains of young and old flies

Glial cell-surface proteins were labeled in intact fly brains, using the biotinylation methods previously described by Li et al. 2020 (Cell). Brain dissections were performed using Dumont #5 Forceps (Fine Science Tools). All dissection tools were cleaned prior to brain dissections with Milli-Q ultrapure water (EMD Millipore) to remove any detergent or chemical contaminants. Brains were then dissected in Schneider's medium (Thermo Fisher), which had been pre-cooled on ice,

706 and subsequently transferred into 1.5 mL protein low-binding tubes (LoBind, Eppendorf), which
707 contained 500 µL of Schneider's medium per sample (i.e., EP tube) and were kept on ice. Optical
708 lobes were removed, and only central brains were used. Following dissection, brains were briefly
709 rinsed with fresh Schneider's medium to remove fat bodies and dissection debris. Next, 100 µM
710 BxxP was dissolved in fresh Schneider's media by extensive vortex and sonication. Brains were
711 then incubated in the BxxP-Schneider's medium for 1 hour on ice (i.e., pre-loaded with BxxP),
712 with occasional mixing by pipetting (Durojaye, 2021). Following incubation, 1 mM (0.003%) H2O2
713 (Thermo Fisher) was added to the BxxP-Schneider's medium for 5-minutes at room temperature,
714 allowing H2O2 to form a reactive complex with HRP (HRP-H2O2) and oxidize BxxP into phenoxyl
715 radicals that react with endogenous proteins in very close proximity (Durojaye, 2021; Guo et al.,
716 2023). Following the 5-minute incubation period, the reaction was then immediately quenched by
717 five thorough washes with PBS (phosphate buffered saline; Thermo Fisher) containing 10 mM
718 sodium ascorbate (Spectrum Chemicals), 5 mM Trolox (Sigma-Aldrich), and 10 mM sodium azide
719 (Sigma-Aldrich), all at room temperature. For biochemical characterization or proteomic sample
720 collection, the quenching solution was then drained, after which brains were snap frozen in liquid
721 nitrogen (and minimal residual quenching solution) and stored at −80°C. For
722 immunocytochemistry, the brains were immediately fixed and stained (see below for details).
723
724 ***Lysis of fly brains***
725 Fly brains were lysed using the methods previously described by Li et al. 2020 (Cell). To
726 avoid potential loss during transfer, brains were processed in the original sample tube. Following
727 biotinylation, 40 µL of high-SDS RIPA buffer (50 mM Tris-HCl [pH 8.0], 150 mM NaCl, 1% sodium
728 dodecyl sulfate (SDS), 0.5% sodium deoxycholate, 1% Triton X-100, 1x protease inhibitor cocktail
729 (P8849), and 1 mM phenylmethylsulfonyl fluoride (PMSF); Sigma-Aldrich) was added to each
730 sample (i.e., EP tube) of frozen brains. Disposable pestles driven by an electric motor (Thermo
731 Fisher) were then used to extensively grind the samples on ice. Following processing, brain
732 lysates of the same experimental group were merged into a single tube, for a final volume of 300
733 µL of high-SDS RIPA buffer per experimental group. Samples were then vortexed briefly, followed
734 by two rounds of 10-second sonication (Li et al., 2020), after which they were heated to 95°C for
735 5 minutes to denature postsynaptic density (Li et al., 2020; Loh et al., 2016). Next, 1.2 mL of SDS-
736 free RIPA buffer (50 mM Tris-HCl [pH 8.0], 150 mM NaCl, 0.5% sodium deoxycholate, 1% Triton
737 X-100, 1x protease inhibitor cocktail (P8849), and 1 mM PMSF) was added to each sample (i.e.,
738 experimental group), after which they were rotated for 1 hour at 4°C. Brain lysates were then
739 transferred to 3.5 mL ultracentrifuge tubes (Beckman Coulter), which contained 200 µL of normal
740 RIPA buffer (50 mM Tris-HCl [pH 8.0], 150 mM NaCl, 0.2% SDS, 0.5% sodium deoxycholate, 1%
741 Triton X-100, 1x protease inhibitor cocktail (P8849), and 1 mM PMSF). Lysates were then
742 centrifuged at 100,000 g for 30 minutes at 4°C, after which 1.5 mL (per sample) of the supernatant
743 was carefully collected and kept on ice.
744
745 ***Enrichment of biotinylated proteins***
746 Streptavidin magnetic beads (Pierce) were used to enrich (i.e., "capture") biotinylated
747 proteins from brain lysates. All chemicals were purchased through Sigma-Aldrich. For silver stains
748 and Western blots, 20 µL of streptavidin beads were added to each sample (which each contained
749 ~50 dissected brains). For proteomic samples, 400 µL were added to each sample (which
750 contained ~1000 dissected brains). Before being added to brain lysates, streptavidin beads were
751 washed twice with normal RIPA buffer (50 mM Tris-HCl [pH 8.0], 150 mM NaCl, 0.2% SDS, 0.5%
752 sodium deoxycholate, and 1% Triton X-100). Washed beads were then added to the post-
753 ultracentrifugation brain lysates and incubated on a rotator overnight at 4°C. Following incubation,
754 beads were washed twice with 1 mL of normal RIPA buffer, then once with 1 mL of 1 M KCl, once
755 with 1 mL of 0.1 M Na2CO3, once with 1 mL of 2 M urea in 10 mM Tris-HCl [pH 8.0], and finally
756 twice with 1 mL of normal RIPA buffer. For silver stains and Western blots, biotinylated proteins

757 were eluted by heating beads at 95°C for 10 minutes in 20 µL of 3x protein loading buffer (Bio-
758 Rad), supplemented with 20 mM dithiothreitol (DTT) and 2mM biotin. For proteomic samples, on-
759 bead trypsin digestion was performed following enrichment (see below for details).
760
761 ***Streptavidin blot***
762 Labeled proteins were separated using electrophoresis. For protein electrophoresis, 4–
763 12% Bis-Tris PAGE gels (Thermo Fisher) were used, following the manufacturer's protocol.
764 Proteins were then transferred to nitrocellulose membranes (Thermo Fisher) for Streptavidin blots.
765 All wash and incubation steps were performed on an orbital shaker at room temperature. For
766 Streptavidin blots, samples were blocked with 3% bovine serum albumin (BSA) in TBST (Tris-
767 buffered saline with 0.1% Tween 20; Thermo Fisher) for 1 hour. Samples were then incubated
768 with HRP-conjugated streptavidin. Clarity Western ECL blotting substrate (Bio-Rad) and
769 BioSpectrum imaging system (UVP) were used for detection of biotinylated proteins.
770
771 ***On-bead trypsin digestion of biotinylated proteins***
772 Proteomic samples were prepared for mass spectrometry analysis using the methods
773 previously described by Li et al. 2020 (Cell). To remove non-biotinylated proteins while retaining
774 the biotinylated proteins on the beads, samples were washed twice with 200 µL of 50 mM Tris-
775 HCl buffer [pH 7.5], followed by two washes with 2 M urea/50 mM Tris [pH 7.5] buffer. Next, the
776 final volume of 2 M urea/50 mM Tris [pH 7.5] buffer was removed, and samples were incubated
777 with 80 µL of 2 M urea/50 mM Tris buffer containing 1 mM dithiothreitol (DTT) and 0.4 µg trypsin.
778 Samples were then incubated in the urea/trypsin buffer for 1 hour at 25°C while shaking at 1000
779 revolutions per minute (rpm). After 1 hour, the supernatant was removed and transferred to a
780 fresh tube. The streptavidin beads were washed twice with 60 µL of 2 M urea/50 mM Tris [pH 7.5]
781 buffer and the washes were combined with the on-bead digest supernatant. The eluate was
782 reduced with 4 mM DTT for 30 minutes at 25°C with shaking at 1000 rpm. The samples were
783 alkylated with 10 mM iodoacetamide and incubated for 45 minutes in the dark at 25°C while
784 shaking at 1000 rpm. An additional 0.5 µg of trypsin was added to the sample and the digestion
785 was completed overnight at 25°C with shaking at 700 rpm. After overnight digestion, the sample
786 was acidified (pH < 3) by adding formic acid (FA) such that the sample contained ~1% FA.
787 Samples were desalted on C18 StageTips (3M). Briefly, C18 StageTips were conditioned with
788 100 µL of 100%MeOH, 100 µL of 50%MeCN/0.1% FA, and 2x with 100 µL of 0.1% FA. Acidified
789 peptides were loaded onto the conditioned StageTips, which were subsequently washed 2x with
790 100 µL of 0.1%FA. Peptides were eluted from StageTips with 50 µL of 50%MeCN/0.1% FA and
791 dried to completion.
792
793 ***TMT labeling and SCX StageTip fractionation of peptides***
794 Desalted peptides were labeled with 8 TMT reagents from a 10-plex reagent kit (Thermo
795 Fisher), as directed by the manufacturer. Peptides were reconstituted in 100 µL of 50 mM HEPES
796 buffer. Each 0.8 mg vial of TMT reagent was reconstituted in 41 µL of anhydrous acetonitrile and
797 added to the corresponding peptide sample for 1 hour at room temperature. Labeling of samples
798 with TMT reagents was completed with the design described in Fig. 1A. TMT labeling reactions
799 were quenched with 8 µL of 5% hydroxylamine at room temperature for 15 minutes with shaking,
800 evaporated to dryness in a vacuum concentrator, and desalted on C18 StageTips as described
801 above.
802 For the TMT 8-plex cassette, 50% of the sample was fractionated by Strong Cation
803 Exchange (SCX) StageTips while the other 50% of each sample was reserved for LC-MS analysis
804 by a single shot, long gradient. One SCX StageTip was prepared per sample using 3 plugs of
805 SCX material (3M) topped with 2 plugs of C18 material. StageTips were sequentially conditioned
806 with 100 µL of MeOH, 100 µL of 80%MeCN/0.5% acetic acid, 100 µL of 0.5% acetic acid, 100 µL
807 of 0.5% acetic acid/500mM NH4AcO/20% MeCN, followed by another 100 µL of 0.5% acetic acid.

808 The dried sample was re-suspended in 250 µL of 0.5% acetic acid, loaded onto the StageTips,
809 and washed 2x with 100 µL of 0.5% acetic acid. The sample was trans-eluted from C18 material
810 onto the SCX with 100 µL of 80%MeCN/0.5% acetic acid, and consecutively eluted using 3 buffers
811 with increasing pH. The first elution was with pH 5.15 (50mM NH4AcO/20% MeCN), followed by
812 pH 8.25 (50mM NH4HCO3/20% MeCN), and finally with pH 10.3 (0.1% NH4OH, 20% MeCN).
813 Three eluted fractions were re-suspended in 200 µL of 0.5% acetic acid, to reduce the MeCN
814 concentration, and subsequently desalted on C18 StageTips as described above. Desalted
815 peptides were dried to completion.
816
817 ***Liquid chromatography and mass spectrometry***
818 Desalted, TMT-labeled peptides were resuspended in 9 µL of 3% MeCN, 0.1% FA and
819 analyzed by online nanoflow liquid chromatography tandem mass spectrometry (LC-MS/MS)
820 using a Fusion Lumos mass spectrometer (Thermo Fisher) coupled on-line to a Proxeon Easy-
821 nLC 1000 (Thermo Fisher). Four microliters of each sample was loaded at 500 nl/min onto a
822 microcapillary column (360 µm outer diameter × 75 µm inner diameter) containing an integrated
823 electrospray emitter tip (10 µm), packed to approximately 24 cm with ReproSil-Pur C18-AQ 1.9
824 µm beads (Dr. Maisch GmbH) and heated to 50°C. The HPLC solvent A was 3% MeCN, 0.1%
825 FA, and the solvent B was 90% MeCN, 0.1% FA. Peptides were eluted into the mass spectrometer
826 at a flow rate of 200 nl/min. The SCX fractions were run with 110-minute method, which used the
827 following gradient profile: (min:%B) 0:2; 1:6; 85:30; 94:60; 95:90; 100:90; 101:50; 110:50 (the last
828 two steps at 500 nL/min flow rate). Non-fractionated samples were analyzed using a 260 min LC-
829 MS/MS method with the following gradient profile: (min:%B) 0:2; 1:6; 235:30; 244:60; 245:90;
830 250:90; 251:50; 260:50 (the last two steps at 500 nL/min flow rate). The Fusion Lumos was
831 operated in the data-dependent mode acquiring HCD MS/MS scans (r =50,000) after each MS1
832 scan (r = 60,000) on the top 12 most abundant ions using an MS1 target of 3 × 106 and an MS2
833 target of 5 × 104. The maximum ion time utilized for MS/MS scans was 120 ms; the HCD
834 normalized collision energy was set to 34; the dynamic exclusion time was set to 20 s, and the
835 peptide match and isotope exclusion functions were enabled. Charge exclusion was enabled for
836 charge states that were unassigned, 1 and >7.
837
838 ***Mass spectrometry data processing***
839 Collected data were analyzed using the Spectrum Mill software package v6.1 pre-release
840 (Agilent Technologies). Nearby MS scans with the similar precursor m/z were merged if they were
841 within ± 60 s retention time and ±1.4 m/z tolerance. MS/MS spectra were excluded from searching
842 if they failed the quality filter by not having a sequence tag length 0 or did not have a precursor
843 MH+ in the range of 750 – 4000. All extracted spectra were searched against a UniProt database
844 containing *Drosophila melanogaster* reference proteome sequences. Search parameters
845 included: ESIC EXACTIVE-HCD-v2 scoring parent and fragment mass tolerance of 20 ppm, 30%
846 minimum matched peak intensity, trypsin allow P enzyme specificity with up to four missed
847 cleavages, and calculate reversed database scores enabled. Fixed modifications were
848 carbamidomethylation at cysteine. TMT labeling was required at lysine, but peptide N termini were
849 allowed to be either labeled or unlabeled. Allowed variable modifications were protein N-terminal
850 acetylation and oxidized methionine. Individual spectra were automatically assigned a confidence
851 score using the Spectrum Mill auto-validation module. Score at the peptide mode was based on
852 target-decoy false discovery rate (FDR) of 1%. Protein polishing auto-validation was then applied
853 using an auto thresholding strategy. Relative abundances of proteins were determined using TMT
854 reporter ion intensity ratios from each MS/MS spectrum and the median ratio was calculated from
855 all MS/MS spectra contributing to a protein subgroup. Proteins identified by 2 or more distinct
856 peptides and ratio counts were considered for the dataset.
857
858 ***Proteomic data analysis***

For our proteomic data analysis, we adopted the ratiometric and cutoff methodologies as previously described (Hung et al., 2014; Li et al., 2020). Detected proteins were classified according to the annotation of subcellular localization in the UniProt database. Proteins with the plasma membrane and extracellular matrix annotations were classified as true-positives (TPs). Proteins with either nucleus, mitochondrion, or cytoplasm annotation, but without the membrane annotation, were classified as false-positives (FPs). Of the total 2,007 detected proteins (those with 2 or more unique peptides), 380 were TPs and 671 were FPs. For each replicate, the proteins were first ranked in a descending order according to the TMT ratio (128C:129C, 129N:130N, 126:127C, or 127N:128N) (Fig. 1D). For each protein on the ranked list, the accumulated true-positive count and false-positive count above its TMT ratio were calculated.

To determine the optimal TMT cutoff values, we plotted the receiver operating characteristic (ROC) curve for each biological replicate (Fig. 1F; Fig. S1), which depicts the true-positive rate against the false-positive rate of detected proteins (Li et al., 2020; Nahm, 2022). To maximize the signal-to-noise ratio of the proteomes, each biological replicate was cut off at the position where the value of *true-positive rate (i.e., sensitivity) – false-positive rate (i.e., specificity)* was maximized: 128C:129C = 0.3076, 129N:130N = 0.3316, 126:127C = 0.3027, or 127N:128N = 0.3059. Post-cutoff proteomic lists of the two biological replicates for each time point were intersected to obtain the final proteome (i.e., only TP proteins that overlapped in both biological replicates at each time point were selected). We also performed cutoff analyses with a different TMT pairing regime (126:128N, 127N:127C, 128C:130N, and 129N:129C) and obtained very similar proteomes (data not shown). All ROC curves were plotted using PEELing, which is an integrated and user-centric platform for spatially-resolved proteomics data analysis (Peng et al., 2025).

To generate correlation plots (Fig. 1E), both biological replicates for each age group were compared to one control at a time, either the control lacking HRP or the control lacking H2O2. For example, for the correlation plot investigating the correlation between biological replicates for old flies using the “no HRP” control, 126:128N is plotted on the x-axis and 127N:128N is plotted on the y-axis. All correlation plots were done using the tidyverse (Wickham et al., 2019) and ggpubr (Kassambara, 2023) packages in R (R Studio Version 2024.12.0+467; R statistical software version 4.1.0; R Core Team, 2021).

Quantitative comparison of young and old proteomes

For the cellular component Gene Ontology (GO) analysis (Fig. 1G), we uploaded the final proteomes (i.e., the 872 proteins identified following our ratiometric and cutoff analyses) into the STRING database search portal and plotted the top five retrieved terms on cellular compartment with the lowest false discovery rates (Szklarczyk et al., 2023). For the biological process GO analyses (Fig. 2B), we uploaded ~100 of the most up-regulated and ~100 of the most down-regulated genes into the STRING database search portal and plotted the top five retrieved terms on biological process with the lowest false discovery rates (Szklarczyk et al., 2023). For the protein network (Fig. 2C), we uploaded ~100 of the most up-regulated and ~100 of the most down-regulated genes into the STRING database search portal and clustered their corresponding proteins by their reported protein-protein interactions and corresponding confidence scores using a Markov clustering algorithm (inflation value set at 2.5) (Szklarczyk et al., 2023). The resulting protein-protein interactions (PPI) were then plotted in Cytoscape (v3.10.3) (Gustavsen et al., 2019). PPI plot “hub” genes were identified using the Cytoscape cytoHubba plugin (Chin et al., 2014). FlyBase and UniProt were searched to determine if each protein in the protein-protein interaction (PPI) plot had reported function in synapse organization, synapse regulation, cell adhesion, development, and localization and transport.

For the volcano plot (Fig. 2A), the TMT ratio (log2FoldChange) for each of the 872 proteins identified was plotted on the x-axis and the log10(Ratio P-value) was plotted on the y-axis using the ggplot2 (Wickham, 2016) and ggrepel (Slowikowski, 2024) packages in R (R Studio Version

2024.12.0+467; R statistical software version 4.1.0; R Core Team, 2021). To identify approximately 50 candidate genes predicted to be involved in brain aging for further screening, we generated a volcano plot, where the TMT ratio (log2FoldChange) for each of the 872 proteins identified was plotted on the x-axis and the log10(Ratio P-value) was plotted on the y-axis (Fig. 2A). Genes associated with the largest change in protein levels between time points were identified using arbitrary cutoff values: 0.4 to -0.4 log protein ratios and 0.1 p-value (Fig. 2A). This generated a list of 71 genes, which were then assessed individually to determine if they were located either on the cell-surface or in the extracellular space. Candidate genes were selected for further screening only if they were known (or predicted to be) located either on the cell-surface or extracellular space. In total, 48 candidate genes were selected for further screening, most of which were known to have at least one strong human ortholog (Supplementary Table 2) (Wang et al., 2017; Wang et al., 2019a; Wang et al., 2019b).

Immunohistochemistry

Dissection and immunostaining of fly brains were performed according to previously described methods (Wu and Luo, 2006; Kelly et al., 2017). Briefly, the brains were dissected in 1xPBS (phosphate buffered saline; Thermo Fisher) and then fixed in 4% paraformaldehyde (Electron Microscopy Sciences) in 1xPBS with 0.015% Triton X-100 (Sigma-Aldrich) for 20 minutes on a nutator at room temperature. Fixed brains were washed with PBST (0.3% Triton X-100 in PBS) four times, each time nutating for 20-30 minutes. The brains were then blocked in 5% normal donkey serum (Jackson ImmunoResearch) or normal goat serum (BioLegend) in PBST for 1 hour at room temperature or overnight at 4°C on a nutator. Primary antibodies were diluted in the blocking solution and incubated with brains for 36–48 hours on a 4°C nutator. After washing with PBST three times, each time nutating for 20 minutes, brains were incubated with secondary antibodies diluted in the blocking solution and nutated in the dark for 24–36 hours at 4°C. Brains were then washed again with PBST three times, each time nutating for 20 minutes. Immunostained brains were mounted with SlowFade antifade reagent (Thermo Fisher) and stored at 4°C before imaging.

Primary antibodies used in immunostaining include: rat anti-NCad (1:40; DN-Ex#8, Developmental Studies Hybridoma Bank), chicken anti-GFP (1:1000; GFP-1020, Aves Labs), rabbit anti-DsRed (1:200; 632496, Takara Bio), and mouse anti-Repo (1:100; 8D12 anti-Repo, Developmental Studies Hybridoma Bank). Donkey or goat secondary antibodies conjugated to Alexa Fluor 488/568/647 (Jackson ImmunoResearch or Thermo Fisher) were used at 1:250. Neutravidin (Thermo Fisher) pre-conjugated with Alexa Fluor 647 was used to detect biotin.

Image acquisition and processing

Images were acquired by either a Zeiss LSM 780 laser-scanning confocal microscope (with a 40x/1.4 Plan-Apochromat oil objective, Carl Zeiss) or a Leica STELLARIS 5 confocal microscope (with a 20x objective). Confocal z-stacks were obtained by 1-μm intervals at the resolution of 512×512. Images were exported as maximum projections or single confocal sections by ZEN (Carl Zeiss) in the format of TIFF. Z-stack images were processed using Image J (Schneider et al., 2012) and Fiji (Schindelin et al., 2012) (Image-Stacks-Z projection-Max Intensity). BioRender was used to make diagrams. Adobe Illustrator was used to assemble all figures, as well as rotate and crop images.

Fly rearing (for lifespan, climbing assays, and single-nucleus RNA-sequencing)

To rear flies for lifespan assays, climbing assays, and single-cell RNA sequencing, we placed 20-30 unmated females with 5-10 males of each genotype in bottles containing standard cornmeal medium. Flies were allowed to mate and lay eggs for 3 days, after which they were flipped into new food bottles and allowed to mate and lay eggs for an additional 4 days. On day

961 4, all F0 parent flies were cleared from the bottles. In general, the glial-GS was used as the
962 maternal line, whereas the RNAi/UAS/flySAM/etc. lines were used as the paternal F0 lines.
963 Following eclosion, F1 flies were allowed to mate for 1-3 days, after which they collected under
964 light CO2 anesthesia and transferred into "cages" containing vials with standard cornmeal
965 medium. Cages consisted of clear polystyrene containers (53 mm diameter, 100 mm height, 175
966 mL) which were plugged with ceaprene foam stoppers (for 175 mL containers) (Greiner Bio-One)
967 that had been modified to accommodate a standard fly food vial (VWR) (i.e., a razor was used to
968 create a hole in the middle of the stopper, which securely held a vial containing standard fly
969 medium). Fly food vials were replaced with new food vials every 2-3 days.
970 In most cases, we were able to collect enough F1 flies 1-3 days post-eclosion (i.e., flies
971 ranged from 1-3 days old when collected and transferred into the lifespan cages) from two crosses
972 per genotype. However, in some cases certain crosses produced fewer F1 progeny, which
973 eclosed slowly over a broader range of time. In these cases, flies could range from 1-5 days old
974 when collected and transferred into the lifespan cages. To best control for this variability in
975 eclosion time, equal numbers of flies were collected for each condition (Ru846 treatment vs.
976 ethanol control) at each collection time point. For example, if 50 F1 flies were collected from a
977 cross on Day 1 following eclosion, 25 flies would be assigned the Ru486 treatment and 25 flies
978 would be assigned to the ethanol control. In cases where we were unable to collect sufficient
979 progeny after 5 days, or wanted to further investigate a particular candidate (like DIP-beta),
980 crosses were remade (with 3-5 crosses per genotype) to reduce the amount of time for sufficient
981 numbers of F1 progeny to eclose. This approach allowed us to maintain a reasonable amount of
982 efficiency screening a large number of candidate genes.
983
984 ***Lifespan assays***
985 For the broadscale lifespan screen of our candidate genes, we collected 80-100 F1 males
986 and 80-100 F1 females per genotype/treatment (i.e., for F1 males, 80-100 flies were assigned to
987 the Ru486 treatment and 80-100 flies were assigned to the ethanol control) and placed them into
988 lifespan cages. Males and females were housed separately for the full duration of all lifespan
989 experiments. Depending on genotype fecundity and eclosion time, flies ranged from 1-5 days old
990 at the start of the experiment (i.e., when they were collected and placed into the lifespan cages
991 following eclosion). All lifespan cages were kept in a humidified, temperature controlled incubator
992 at 25℃ with a 12:12 hour light/dark cycle for the full duration of the experiment (Bauer et al., 2004).
993 Flies were allowed to mature for 3-6 days on plain standard cornmeal medium (to ensure that the
994 adult brains were fully developed prior to gene expression manipulation), after which flies were
995 switched to fly food vials containing either the Ru486 (mifepristone) drug treatment or the ethanol
996 control. To prepare the Ru486 food vials, 100 μL of Ru486 solution (4mM Ru486 powder
997 dissolved by vortex into 200-proof ethanol) was added to each vial, which contained standard fly
998 medium (Goodman et al., 2021). To prepare the ethanol control vials, 100 μL of 200-proof ethanol
999 was added to each vial. The Ru486 was purchased from Cayman Chemical and the 200-proof
1000 ethanol was purchased from Thermo Scientific. All Ru486 and ethanol control food vials were
1001 allowed to dry completely before being introduced to the flies to prevent flies from sticking to the
1002 wet medium. Ru486 or ethanol control food vials were exchanged with new food vials every 2-3
1003 days for the full duration of the experiment, at which time the number of flies that were alive, dead,
1004 or had escaped during the food exchange were noted. Lifespan experiments continued until all
1005 flies were dead.
1006
1007 ***Climbing assays***
1008 To age flies for climbing assays (and single-cell RNA sequencing), we collected 56 F1
1009 males and 66-68 F1 females (collected from several glial-GeneSwitch x DIP-β flySAM crosses)
1010 per treatment (Ru486 treatment vs. ethanol control) and transferred them into lifespan cages.
1011 Flies were allowed to mature for 3-6 days on plain standard cornmeal medium, after which flies

1012 were switched to fly food vials containing either the Ru486 drug treatment or the ethanol control.
1013 Males and females were aged separately in their respective cages until they reached the target
1014 age of 50-55 days old. To prepare for climbing assays, flies were collected under light CO2
1015 anesthesia and transferred from their "cages" into either Ru486 drug supplemented or ethanol
1016 control food vials (8-10 males and 8-10 females per vial) (Ali et al., 2011). Flies were allowed to
1017 recover from the CO2 anesthesia for 3 days (Ali et al., 2011; Burns et al., 2020; Burns and Saltz,
1018 2024). During this time, flies were kept in a humidified, temperature controlled incubator at 25℃
1019 with a 12:12 hour light/dark cycle (Ali et al., 2011). On the third day, flies were transferred to a
1020 humidified, temperature controlled room (25℃) (Goodman et al., 2019) and allowed to acclimate
1021 for 1 hour prior. Following this acclimation period, unanesthetized flies were gently transferred
1022 from food vials into the lanes of the climbing apparatus, which were plugged with cellulose acetate
1023 plugs (VWR) and additionally secured with general purpose laboratory tape (VWR), after which
1024 they were allowed to acclimate in their lanes for 5 minutes. For the climbing assay, flies were
1025 tapped to the bottom of an empty vial and immediately video recorded for 10 seconds (Ali et al.,
1026 2011; Goodman et al., 2019). Each test group was subjected to 3 consecutive trials with a 1
1027 minute recovery between trials (Ali et al., 2011; Goodman et al., 2019). For analysis, the climbing
1028 height (in centimeters) for each fly at the 10-second time point was recorded. Mean climbing
1029 height values from the 3 trials per test group were used to account for technical variability (Ali et
1030 al., 2011; Goodman et al., 2019). Upon completion of the climbing assays, flies were humanely
1031 sacrificed by being placed in a freezer for a minimum of 24 hours (Burns and Saltz, 2024).
1032
1033 ***Single-nucleus RNA-sequencing***
1034 The heads of female flies were collected at day 50 (i.e., when the flies were 50 days old),
1035 placed into 1.5 mL Eppendorf tubes, flash-frozen in liquid nitrogen, and stored at -80C. In total,
1036 two samples (each containing 20 heads) were prepared for single-nucleus RNA sequencing: one
1037 where DIP-beta had been overexpressed in glial cells from day 5-50 and one where DIP-beta
1038 expression had not been manipulated (i.e., the flies received an ethanol control instead of the
1039 Ru486 drug used to induce overexpression of DIP-beta). Single-nucleus suspensions were
1040 prepared as described in the Fly Cell Atlas (Li et al., 2022). After nuclei dissociation, the nuclei
1041 were purified from debris using the SONY SH800 FACS sorter. Nuclei were stained with Hoechst-
1042 33342 (1:1000, >5 minutes). It is typical to observe separate cell populations during FACS since
1043 some cells have variable sizes of nuclei and ploidy numbers. All populations were included to
1044 ensure every cell would be captured from the samples. Nuclei were collected in a 1.5 mL
1045 Eppendorf tube containing 200uL 1X PBS with 0.5% BSA (RNase inhibitor added). For each of
1046 the 10X Genomics runs, 250-300k nuclei were collected. The nuclei were centrifuged for 10
1047 minutes at 1000g in 4C. conditions and then resuspended using 40uL of 1X PBS with 0.5% BSA
1048 (RNase inhibitor added). 2uL of the nuclei suspension were allocated for counting under a
1049 hemocytometer to calculate the nuclei concentration. For the high-throughput single-cell
1050 sequencing kit from 10X Genomics, we loaded 50k cells into the Chromium Controller to target a
1051 final number of 20-30k nuclei.
1052 Single-nucleus RNA-seq libraries were prepared using the 10X Genomics Chromium
1053 Single Cell 3' HT v3.1 protocol. All PCR reactions were performed using the BioRad C1000 Touch
1054 Thermal Cycler with the 96-Deep Well Reaction Module. We used 11 cycles for the cDNA
1055 amplification and then we used 13 cycles for the sample index PCR. As per the 10X Genomics
1056 protocol, 1:10 dilutions of amplified cDNA and the final gene expression libraries were evaluated
1057 on the Agilent Tapestation Bioanalyzer. Each library was diluted to approximately 4nM and equal
1058 volumes of each library were pooled in a NovaSeq PE150 S4 sequencing run. Pools were
1059 sequenced with the dual index configuration Read 1 28 cycles, Index 1 (i7) 10 cycles, Index 2 (i5)
1060 10 cycles, and Read 2 90 cycles. The sequencing depth was about 30-40k reads per nucleus.
1061
1062 ***Preprocessing and quality control of single-nucleus RNA-sequencing data***

The Drosophila melanogaster genome (FlyBase Release 6.31) was downloaded along with a pre-mRNA GTF containing both intronic and exonic annotations, then indexed using Cell Ranger mkref v7.0.1 (10x Genomics) to enable accurate mapping of nucleus-derived transcripts (Zheng et al., 2017; Thurmond et al., 2019). Paired-end FASTQ reads were aligned to this custom reference using Cell Ranger count v7.0.1, producing raw feature-barcode matrices and QC metrics (Zheng et al., 2017).

To remove background ("ambient") RNA contamination inherent to droplet-based assays and technical artifacts, we applied CellBender remove-background v0.3.2, which employs a deep generative model to distinguish true cell-derived signal from ambient noise (Fleming et al., 2023). Barcodes flagged as potential doublets were then identified and removed with scDblFinder v1.22.0, a Bioconductor package that simulates artificial doublets and uses neighborhood classification to assign doublet probabilities (Germain et al., 2021).

We next filtered nuclei based on gene and UMI counts: cells with fewer than 200 detected genes or fewer than 300 UMIs were discarded to exclude low-quality captures, while those exceeding five median absolute deviations above the median for either metric were deemed outliers and removed (Luecken and Theis, 2019). Finally, nuclei with >10 % mitochondrial UMIs—indicative of damaged or apoptotic cells—were excluded from further analysis (Ilicic et al., 2016). After all the above quality control processing, 26,261 nuclei in the –RU condition and 22,698 nuclei in the +RU condition were retained.

Single-nucleus RNA clustering and annotation

The Ru486+ (+RU) and Ru486- (-RU, i.e., the ethanol control) matrices were merged into a single AnnData object and log-normalized. We then computed 150 principal components (PCs) to capture major sources of biological variation. To correct batch effects between conditions while preserving true transcriptomic differences, Harmony v1.0 was applied to the PC embeddings (Korsunsky et al., 2019).

Cell-type labels were transferred from the AD-FCA (specifically the whole-head data, comprising 108 fine-grained cell types) using machine learning basedlabel-transfer workflow (Lu et al., 2023; Stuart et al., 2019). A k-nearest-neighbor graph ($k = 20$) was built on the Harmony-corrected PCs, and the Leiden algorithm (Traag and Waltman, 2019) at resolution 6 was used to detect communities, yielding 130 clusters with high modularity and guaranteed connectivity (Traag et al. 2019). Clusters were then inspected and, where necessary, manually corrected based on marker expression and neighborhood structure, and subsequently consolidated into nine broad cell-type categories for downstream analyses.

snRNA-seq: cell composition

To quantify how DIP-β overexpression alters cellular makeup, we counted the nuclei assigned to each broad cell type in DIP-β overexpression versus control samples. Cell-type proportions were normalized by the total number of nuclei per genotype, allowing direct comparison of enrichment or depletion across conditions.

Climb

snRNA-seq: DEG analysis

Within each broad cell type, we identified differentially expressed genes (DEGs) between DIP-β overexpression and control samples using the Wilcoxon rank-sum test implemented in Scanpy's rank_genes_groups function (Wolf et al., 2018), applying Benjamini–Hochberg correction for multiple testing. Genes with a false discovery rate (FDR) < 0.05 were considered significant.

snRNA-seq: KEGG pathway analysis

Significant DEGs ($|\log_2 \text{fold change}| > 0.5$, FDR < 0.05) were subjected to pathway enrichment analysis using the clusterProfiler R package (Yu et al., 2012), mapping to the Kyoto Encyclopedia of Genes and Genomes (KEGG) database (Kanehisa and Goto, 2000). Enriched pathways with adjusted p-values (FDR) < 0.05 were reported.

snRNA-seq: cell-cell communication analysis

Cell-cell communication analysis was performed using our recently developed FlyPhoneDB2 (Qadiri et al., 2025). The core algorithm infers tissue-specific signaling events between cell types by calculating cell-cell interaction scores based on curated ligand-receptor pairs.

Quantification and Statistical Analyses

No statistical methods were used to determine sample sizes, but our sample sizes were similar to those generally employed in the field (Li et al., 2020). Any brains damaged in dissection were excluded from analysis. Excel (Microsoft), Prism (GraphPad), and R (R Studio Version 2024.12.0+467; R statistical software version 4.1.0; R Core Team, 2021) were used for data analysis and plotting. Statistical methods used are described in the figure legend of each relevant panel.

Data and Code Availability

The original mass spectra and the protein sequence databases used for searches have been deposited in the public proteomics repository MassIVE (http://massive.ucsd.edu) (username: MSV000099083; password: glial). These datasets will be made public upon acceptance of the manuscript. Original proteomic data prior to analyses is provided in the Supplementary Table 1. snRNA-seq data has been deposited to NCBI Gene Expression Omnibus (GSE308135).

References

1. Mattson, M.P.; Arumugam, T.V. Hallmarks of Brain Aging: Adaptive and Pathological Modification by Metabolic States. *Cell Metabolism*. **2018**, *27(6)*, 1176-1199.1.
2. Ebeling M, Rau R, Malmström H, Ahlbom A, Modig K. The rate by which mortality increase with age is the same for those who experienced chronic disease as for the general population. Age Ageing. 2021 Sep 11;50(5):1633-1640. doi: 10.1093/ageing/afab085. PMID: 34038514; PMCID: PMC8437060.
3. Dorsey ER, Bloem BR. Parkinson's Disease Is Predominantly an Environmental Disease. J Parkinsons Dis. 2024;14(3):451-465. doi: 10.3233/JPD-230357. PMID: 38217613; PMCID: PMC11091623.
4. Iijima, K.; Liu, H.P.; Chiang, A.S.; Hearn, S.A.; Konsolaki, M.; Zhong, Y. Dissecting the pathological effects of human Abeta40 and Abeta42 in *Drosophila*: a potential model for Alzheimer's disease. *Proc Natl Acad Sci USA*. **2004**, *101(17)*, 6623-8.
5. Drachman, D.A. Aging of the brain, entropy, and Alzheimer disease. *Neurology*. **2006**, *67(8)*, 1340-52.
6. Moqri, M.; Herzog, C.; Poganik, J.R.; Biomarkers of Aging Consortium; Justice, J.; Belsky, D.W.; Higgins-Chen, A.; Moskalev, A.; Fuellen, G., Cohen; A.A., Bautmans, I.; Widschwendter, M.; Ding, J.; Fleming, A.; Mannick, J.; Han, J.J.; Zhavoronkov, A.; Barzilai, N.; Kaeberlein, M.; Cummings, S.; Kennedy, B.K.; Ferrucci, L.; Horvath, S.; Verdin, E.;

Maier, A.B.; Snyder, M.P.; Sebastiano, V.; Gladyshev, V.N. Biomarkers of aging for the identification and evaluation of longevity interventions. *Cell*. **2023**, *186(18)*, 3758-3775.

7. Barres, B.A. The mystery and magic of glia: a perspective on their roles in health and disease. *Neuron*. **2008**, *60(3)*, 430-40.
8. Freeman, M.R. *Drosophila* Central Nervous System Glia. *Cold Spring Harb Perspect Biol*. **2015**, *7(11)*, a020552.
9. Kremer, M.C.; Jung, C.; Batelli, S.; Rubin, G.M.; Gaul, U. The glia of the adult *Drosophila* nervous system. *Glia*. **2017**, *65(4)*, 606-638.
10. Sperry RW. CHEMOAFFINITY IN THE ORDERLY GROWTH OF NERVE FIBER PATTERNS AND CONNECTIONS. Proc Natl Acad Sci U S A. 1963 Oct;50(4):703-10. doi: 10.1073/pnas.50.4.703. PMID: 14077501; PMCID: PMC221249.
11. Malenka RC, Bear MF. LTP and LTD: an embarrassment of riches. Neuron. 2004 Sep 30; 44(1): 5-21. doi: 10.1016/j.neuron.2004.09.012. PMID: 15450156.
12. Jan YN, Jan LY. Branching out: mechanisms of dendritic arborization. Nat Rev Neurosci. 2010 May;11(5):316-28. doi: 10.1038/nrn2836. Erratum in: Nat Rev Neurosci. 2010 Jun;11(6):449. PMID: 20404840; PMCID: PMC3079328.
13. Zipursky SL, Sanes JR. Chemoaffinity revisited: dscams, protocadherins, and neural circuit assembly. Cell. 2010 Oct 29;143(3):343-53. doi: 10.1016/j.cell.2010.10.009. PMID: 21029858.
14. Kolodkin AL, Tessier-Lavigne M. Mechanisms and molecules of neuronal wiring: a primer. Cold Spring Harb Perspect Biol. 2011 Jun 1;3(6): a001727. doi: 10.1101/cshperspect.a001727. PMID: 21123392; PMCID: PMC3098670.
15. Yeh FL, Hansen DV, Sheng M. TREM2, Microglia, and Neurodegenerative Diseases. Trends Mol Med. 2017 Jun;23(6):512-533. doi: 10.1016/j.molmed.2017.03.008. Epub 2017 Apr 22. PMID: 28442216.
16. Li J, Han S, Li H, Udeshi ND, Svinkina T, Mani DR, Xu C, Guajardo R, Xie Q, Li T, Luginbuhl DJ, Wu B, McLaughlin CN, Xie A, Kaewsapsak P, Quake SR, Carr SA, Ting AY, Luo L. Cell-Surface Proteomic Profiling in the Fly Brain Uncovers Wiring Regulators. Cell. 2020 Jan 23;180(2):373-386.e15. doi: 10.1016/j.cell.2019.12.029. Epub 2020 Jan 16. PMID: 31955847; PMCID: PMC7072036.
17. McAlpine, C.S.; Park, J.; Griciuc, A.; Kim, E.; Choi, S.H.; Iwamoto, Y.; Kiss, M.G.; Christie, K.A.; Vinegoni, C.; Poller, W.C.; Mindur, J.E.; Chan, C.T.; He, S.; Janssen, H.; Wong, L.P.; Downey, J.; Singh, S.; Anzai, A.; Kahles, F.; Jorfi, M.; Feruglio, P.F.; Sadreyev, R.I.; Weissleder, R.; Kleinstiver, B.P.; Nahrendorf, M.; Tanzi, R.E.; Swirski, F.K. Astrocytic interleukin-3 programs microglia and limits Alzheimer's disease. *Nature*. **2021**, *595(7869)*, 701-706.
18. Cordwell SJ, Thingholm TE. Technologies for plasma membrane proteomics. Proteomics. 2010 Feb;10(4):611-27. doi: 10.1002/pmic.200900521. PMID: 19834916.
19. Xie, Q.; Li, J.; Li, H.; Udeshi, N.D., Svinkina, T., Orlin, D.; Kohani, S.; Guajardo, R.; Mani, D.R.; Xu, C.; Li, T.; Han, S.; Wei, W.; Shuster, S.A.; Luginbuhl, D.J.; Quake, S.R.; Murthy, S.E.; Ting, A.Y.; Carr, S.A., Luo, L. Transcription factor Acj6 controls dendrite targeting via a combinatorial cell-surface code. *Neuron*. **2022**, *110(14)*, 2299-2314.
20. Shuster SA, Li J, Chon U, Sinantha-Hu MC, Luginbuhl DJ, Udeshi ND, Carey DK, Takeo YH, Xie Q, Xu C, Mani DR, Han S, Ting AY, Carr SA, Luo L. In situ cell-type-specific cell-surface proteomic profiling in mice. Neuron. 2022 Dec 7;110(23):3882-3896.e9. doi: 10.1016/j.neuron.2022.09.025. Epub 2022 Oct 10. PMID: 36220098; PMCID: PMC9742329.
21. Szklarczyk D, Kirsch R, Koutrouli M, Nastou K, Mehryary F, Hachilif R, Gable AL, Fang T, Doncheva NT, Pyysalo S, Bork P, Jensen LJ, von Mering C. The STRING database in 2023: protein-protein association networks and functional enrichment analyses for any

sequenced genome of interest. Nucleic Acids Res. 2023 Jan 6;51(D1):D638-D646. doi: 10.1093/nar/gkac1000. PMID: 36370105; PMCID: PMC9825434.

22. Carrillo RA, Özkan E, Menon KP, Nagarkar-Jaiswal S, Lee PT, Jeon M, Birnbaum ME, Bellen HJ, Garcia KC, Zinn K. Control of Synaptic Connectivity by a Network of Drosophila IgSF Cell Surface Proteins. Cell. 2015 Dec 17;163(7):1770-1782. doi: 10.1016/j.cell.2015.11.022. PMID: 26687361; PMCID: PMC4720259.

23. Cosmanescu F, Katsamba PS, Sergeeva AP, Ahlsen G, Patel SD, Brewer JJ, Tan L, Xu S, Xiao Q, Nagarkar-Jaiswal S, Nern A, Bellen HJ, Zipursky SL, Honig B, Shapiro L. Neuron-Subtype-Specific Expression, Interaction Affinities, and Specificity Determinants of DIP/Dpr Cell Recognition Proteins. Neuron. 2018 Dec 19;100(6):1385-1400.e6. doi: 10.1016/j.neuron.2018.10.046. Epub 2018 Nov 19. PMID: 30467080; PMCID: PMC6309224.

24. Sanes JR, Zipursky SL. Synaptic Specificity, Recognition Molecules, and Assembly of Neural Circuits. Cell. 2020 Apr 30;181(3):536-556. doi: 10.1016/j.cell.2020.04.008. Erratum in: Cell. 2020 Jun 11;181(6):1434-1435. doi: 10.1016/j.cell.2020.05.046. PMID: 32359437.

25. Sergeeva AP, Katsamba PS, Cosmanescu F, Brewer JJ, Ahlsen G, Mannepalli S, Shapiro L, Honig B. DIP/Dpr interactions and the evolutionary design of specificity in protein families. Nat Commun. 2020 May 1;11(1):2125. doi: 10.1038/s41467-020-15981-8. PMID: 32358559; PMCID: PMC7195491.

26. Wang Y, Lobb-Rabe M, Ashley J, Chatterjee P, Anand V, Bellen HJ, Kanca O, Carrillo RA. Systematic expression profiling of Dpr and DIP genes reveals cell surface codes in Drosophila larval motor and sensory neurons. Development. 2022 May 15;149(10):dev200355. doi: 10.1242/dev.200355. Epub 2022 May 19. PMID: 35502740; PMCID: PMC9188756.

27. Ma D, Herndon N, Le JQ, Abruzzi KC, Zinn K, Rosbash M. Neural connectivity molecules best identify the heterogeneous clock and dopaminergic cell types in the *Drosophila* adult brain. Sci Adv. 2023 Feb 22;9(8):eade8500. doi: 10.1126/sciadv.ade8500. Epub 2023 Feb 22. PMID: 36812309; PMCID: PMC9946362.

28. Loh KH, Stawski PS, Draycott AS, Udeshi ND, Lehrman EK, Wilton DK, Svinkina T, Deerinck TJ, Ellisman MH, Stevens B, Carr SA, Ting AY. Proteomic Analysis of Unbounded Cellular Compartments: Synaptic Clefts. Cell. 2016 Aug 25;166(5):1295-1307.e21. doi: 10.1016/j.cell.2016.07.041. PMID: 27565350; PMCID: PMC5167540.

29. Larsen CW, Hirst E, Alexandre C, Vincent JP. Segment boundary formation in Drosophila embryos. Development. 2003 Dec;130(23):5625-35. doi: 10.1242/dev.00867. Epub 2003 Oct 1. PMID: 14522878.

30. Watts RJ, Schuldiner O, Perrino J, Larsen C, Luo L. Glia engulf degenerating axons during developmental axon pruning. Curr Biol. 2004 Apr 20;14(8):678-84. doi: 10.1016/j.cub.2004.03.035. PMID: 15084282.

31. Durojaye OA. Intracellular proteome compartmentalization: a biotin ligase-based proximity labeling approach. Cell Biosci. 2021 Aug 23;11(1):165. doi: 10.1186/s13578-021-00666-6. PMID: 34425888; PMCID: PMC8381540.

32. Renuse S, Madugundu AK, Jung JH, Byeon SK, Goldschmidt HL, Tahir R, Meyers D, Kim DI, Cutler J, Kim KP, Wu X, Huganir RL, Pandey A. Signature Fragment Ions of Biotinylated Peptides. J Am Soc Mass Spectrom. 2020 Feb 5;31(2):394-404. doi: 10.1021/jasms.9b00024. Epub 2020 Jan 13. PMID: 31939678; PMCID: PMC7199424.

33. Thompson A, Schäfer J, Kuhn K, Kienle S, Schwarz J, Schmidt G, Neumann T, Johnstone R, Mohammed AK, Hamon C. Tandem mass tags: a novel quantification strategy for comparative analysis of complex protein mixtures by MS/MS. Anal Chem. 2003 Apr 15;75(8):1895-904. doi: 10.1021/ac0262560. Erratum in: Anal Chem. 2003 Sep

15;75(18):4942. Johnstone, R [added]. Erratum in: Anal Chem. 2006 Jun 15;78(12):4235. Mohammed, A Karim A [added]. PMID: 12713048.

34. Hung V, Zou P, Rhee HW, Udeshi ND, Cracan V, Svinkina T, Carr SA, Mootha VK, Ting AY. Proteomic mapping of the human mitochondrial intermembrane space in live cells via ratiometric APEX tagging. Mol Cell. 2014 Jul 17;55(2):332-41. doi: 10.1016/j.molcel.2014.06.003. Epub 2014 Jul 4. PMID: 25002142; PMCID: PMC4743503.
35. Nahm FS. Receiver operating characteristic curve: overview and practical use for clinicians. Korean J Anesthesiol. 2022 Feb;75(1):25-36. doi: 10.4097/kja.21209. Epub 2022 Jan 18. PMID: 35124947; PMCID: PMC8831439.
36. Ashburner M, Ball CA, Blake JA, Botstein D, Butler H, Cherry JM, Davis AP, Dolinski K, Dwight SS, Eppig JT, Harris MA, Hill DP, Issel-Tarver L, Kasarskis A, Lewis S, Matese JC, Richardson JE, Ringwald M, Rubin GM, Sherlock G. Gene ontology: tool for the unification of biology. The Gene Ontology Consortium. Nat Genet. 2000 May;25(1):25-9. doi: 10.1038/75556. PMID: 10802651; PMCID: PMC3037419.
37. Johnson ECB, Dammer EB, Duong DM, Ping L, Zhou M, Yin L, Higginbotham LA, Guajardo A, White B, Troncoso JC, Thambisetty M, Montine TJ, Lee EB, Trojanowski JQ, Beach TG, Reiman EM, Haroutunian V, Wang M, Schadt E, Zhang B, Dickson DW, Ertekin-Taner N, Golde TE, Petyuk VA, De Jager PL, Bennett DA, Wingo TS, Rangaraju S, Hajjar I, Shulman JM, Lah JJ, Levey AI, Seyfried NT. Large-scale proteomic analysis of Alzheimer's disease brain and cerebrospinal fluid reveals early changes in energy metabolism associated with microglia and astrocyte activation. Nat Med. 2020 May;26(5):769-780. doi: 10.1038/s41591-020-0815-6. Epub 2020 Apr 13. PMID: 32284590; PMCID: PMC7405761.
38. Wang J, Al-Ouran R, Hu Y, Kim SY, Wan YW, Wangler MF, Yamamoto S, Chao HT, Comjean A, Mohr SE; UDN; Perrimon N, Liu Z, Bellen HJ. MARRVEL: Integration of Human and Model Organism Genetic Resources to Facilitate Functional Annotation of the Human Genome. Am J Hum Genet. 2017 Jun 1;100(6):843-853. doi: 10.1016/j.ajhg.2017.04.010. Epub 2017 May 11. PMID: 28502612; PMCID: PMC5670038.
39. Wang J, Liu Z, Bellen HJ, Yamamoto S. Navigating MARRVEL, a Web-Based Tool that Integrates Human Genomics and Model Organism Genetics Information. J Vis Exp. 2019 Aug 15;(150):10.3791/59542. doi: 10.3791/59542. PMID: 31475990; PMCID: PMC7401700.
40. Wang J, Mao D, Fazal F, Kim SY, Yamamoto S, Bellen H, Liu Z. Using MARRVEL v1.2 for Bioinformatics Analysis of Human Genes and Variant Pathogenicity. Curr Protoc Bioinformatics. 2019 Sep;67(1):e85. doi: 10.1002/cpbi.85. PMID: 31524990; PMCID: PMC6750039.
41. Mattson MP, Duan W, Maswood N. How does the brain control lifespan? Ageing Res Rev. 2002 Apr;1(2):155-65. doi: 10.1016/s1568-1637(01)00003-4. PMID: 12039436.
42. Woodling NS, Rajasingam A, Minkley LJ, Rizzo A, Partridge L. Independent glial subtypes delay development and extend healthy lifespan upon reduced insulin-PI3K signalling. BMC Biol. 2020 Sep 14;18(1):124. doi: 10.1186/s12915-020-00854-9. PMID: 32928209; PMCID: PMC7490873.
43. Schmid ET, Pyo JH, Walker DW. Neuronal induction of BNIP3-mediated mitophagy slows systemic aging in *Drosophila*. Nat Aging. 2022 Jun;2(6):494-507. doi: 10.1038/s43587-022-00214-y. Epub 2022 May 16. PMID: 36213625; PMCID: PMC9540997.
44. Nicholson L, Singh GK, Osterwalder T, Roman GW, Davis RL, Keshishian H. Spatial and temporal control of gene expression in Drosophila using the inducible GeneSwitch GAL4 system. I. Screen for larval nervous system drivers. Genetics. 2008 Jan;178(1):215-34. doi: 10.1534/genetics.107.081968. PMID: 18202369; PMCID: PMC2206072.

45. Osterwalder, T.; Yoon, K.S.; White, B.H.; Keshishian, H. A conditional tissue specific transgene expression system using inducible GAL4. *Proc Natl Acad Sci USA*. **2001**, *98(22)*, 12596-601.
46. Dietzl G, Chen D, Schnorrer F, Su KC, Barinova Y, Fellner M, Gasser B, Kinsey K, Oppel S, Scheiblauer S, Couto A, Marra V, Keleman K, Dickson BJ. A genome-wide transgenic RNAi library for conditional gene inactivation in Drosophila. Nature. 2007 Jul 12;448(7150):151-6. doi: 10.1038/nature05954. PMID: 17625558.
47. Ni JQ, Zhou R, Czech B, Liu LP, Holderbaum L, Yang-Zhou D, Shim HS, Tao R, Handler D, Karpowicz P, Binari R, Booker M, Brennecke J, Perkins LA, Hannon GJ, Perrimon N. A genome-scale shRNA resource for transgenic RNAi in Drosophila. Nat Methods. 2011 May;8(5):405-7. doi: 10.1038/nmeth.1592. Epub 2011 Apr 3. PMID: 21460824; PMCID: PMC3489273.
48. Perkins LA, Holderbaum L, Tao R, Hu Y, Sopko R, McCall K, Yang-Zhou D, Flockhart I, Binari R, Shim HS, Miller A, Housden A, Foos M, Randkelv S, Kelley C, Namgyal P, Villalta C, Liu LP, Jiang X, Huan-Huan Q, Wang X, Fujiyama A, Toyoda A, Ayers K, Blum A, Czech B, Neumuller R, Yan D, Cavallaro A, Hibbard K, Hall D, Cooley L, Hannon GJ, Lehmann R, Parks A, Mohr SE, Ueda R, Kondo S, Ni JQ, Perrimon N. The Transgenic RNAi Project at Harvard Medical School: Resources and Validation. Genetics. 2015 Nov;201(3):843-52. doi: 10.1534/genetics.115.180208. Epub 2015 Aug 28. PMID: 26320097; PMCID: PMC4649654.
49. Jia, Y.; Xu, R.G.; Ren, X.; Ewen-Campen, B.; Rajakumar, R.; Zirin, J.; Yang-Zhou, D.; Zhu, R.; Wang, F.; Mao, D.; Peng, P.; Qiao, H.H.; Wang, X.; Liu, L.P.; Xu, B.; Ji, J.Y.; Liu, Q.; Sun, J.; Perrimon, N.; Ni, J.Q. Next-generation CRISPR/Cas9 transcriptional activation in *Drosophila* using flySAM. *Proc Natl Acad Sci USA*. **2018**, *115(18)*, 4719-4724.
50. Barone, M.C.; Bohmann, D. Assessing neurodegenerative phenotypes in *Drosophila* dopaminergic neurons by climbing assays and whole brain immunostaining. *J Vis Exp*. **2013**, *74*, e50339.
51. Beharry, C.; Alaniz, M.E.; Alonso Adel, C. Expression of Alzheimer-like pathological human tau induces a behavioral motor and olfactory learning deficit in *Drosophila melanogaster*. *J Alzheimers Dis*. **2013**, *37(3)*, 539-50.
52. Manjila SB, Hasan G. Flight and Climbing Assay for Assessing Motor Functions in *Drosophila*. Bio Protoc. 2018 Mar 5;8(5):e2742. doi: 10.21769/BioProtoc.2742. PMID: 34179270; PMCID: PMC8203865.
53. Lu, T.C.; Brbić, M.; Park, Y.J.; Jackson, T.; Chen, J.; Kolluru, S.S.; Qi, Y., Katheder, N.S.; Cai, X.T.; Lee, S.; Chen, Y.C.; Auld, N.; Liang, C.Y.; Ding, S.H.; Welsch, D.; D'Souza, S.; Pisco, A.O.; Jones, R.C.; Leskovec, J.; Lai, E.C.; Bellen, H.J.; Luo, L.; Jasper, H.; Quake, S.R.; Li H. Aging Fly Cell Atlas identifies exhaustive aging features at cellular resolution. *Science*. **2023**, *380(6650)*, eadg0934.
54. Park YJ, Lu TC, Jackson T, Goodman LD, Ran L, Chen J, Liang CY, Harrison E, Ko C, Chen X, Wang B, Hsu AL, Ochoa E, Bieniek KF, Yamamoto S, Zhu Y, Zheng H, Qi Y, Bellen HJ, Li H. Distinct systemic impacts of Aβ42 and Tau revealed by whole-organism snRNA-seq. Neuron. 2025 Jul 9;113(13):2065-2082.e8. doi: 10.1016/j.neuron.2025.04.017. Epub 2025 May 16. PMID: 40381615; PMCID: PMC12245608.
55. Li H, Janssens J, De Waegeneer M, Kolluru SS, Davie K, Gardeux V, Saelens W, David FPA, Brbić M, Spanier K, Leskovec J, McLaughlin CN, Xie Q, Jones RC, Brueckner K, Shim J, Tattikota SG, Schnorrer F, Rust K, Nystul TG, Carvalho-Santos Z, Ribeiro C, Pal S, Mahadevaraju S, Przytycka TM, Allen AM, Goodwin SF, Berry CW, Fuller MT, White-Cooper H, Matunis EL, DiNardo S, Galenza A, O'Brien LE, Dow JAT; FCA Consortium§; Jasper H, Oliver B, Perrimon N, Deplancke B, Quake SR, Luo L, Aerts S, Agarwal D,

Ahmed-Braimah Y, Arbeitman M, Ariss MM, Augsburger J, Ayush K, Baker CC, Banisch T, Birker K, Bodmer R, Bolival B, Brantley SE, Brill JA, Brown NC, Buehner NA, Cai XT, Cardoso-Figueiredo R, Casares F, Chang A, Clandinin TR, Crasta S, Desplan C, Detweiler AM, Dhakan DB, Donà E, Engert S, Floc'hlay S, George N, González-Segarra AJ, Groves AK, Gumbin S, Guo Y, Harris DE, Heifetz Y, Holtz SL, Horns F, Hudry B, Hung RJ, Jan YN, Jaszczak JS, Jefferis GSXE, Karkanias J, Karr TL, Katheder NS, Kezos J, Kim AA, Kim SK, Kockel L, Konstantinides N, Kornberg TB, Krause HM, Labott AT, Laturney M, Lehmann R, Leinwand S, Li J, Li JSS, Li K, Li K, Li L, Li T, Litovchenko M, Liu HH, Liu Y, Lu TC, Manning J, Mase A, Matera-Vatnick M, Matias NR, McDonough-Goldstein CE, McGeever A, McLachlan AD, Moreno-Roman P, Neff N, Neville M, Ngo S, Nielsen T, O'Brien CE, Osumi-Sutherland D, Özel MN, Papatheodorou I, Petkovic M, Pilgrim C, Pisco AO, Reisenman C, Sanders EN, Dos Santos G, Scott K, Sherlekar A, Shiu P, Sims D, Sit RV, Slaidina M, Smith HE, Sterne G, Su YH, Sutton D, Tamayo M, Tan M, Tastekin I, Treiber C, Vacek D, Vogler G, Waddell S, Wang W, Wilson RI, Wolfner MF, Wong YE, Xie A, Xu J, Yamamoto S, Yan J, Yao Z, Yoda K, Zhu R, Zinzen RP. Fly Cell Atlas: A single-nucleus transcriptomic atlas of the adult fruit fly. Science. 2022 Mar 4;375(6584):eabk2432. doi: 10.1126/science.abk2432. Epub 2022 Mar 4. PMID: 35239393; PMCID: PMC8944923.

56. Chen L, Zhang YH, Wang S, Zhang Y, Huang T, Cai YD. Prediction and analysis of essential genes using the enrichments of gene ontology and KEGG pathways. PLoS One. 2017 Sep 5;12(9):e0184129. doi: 10.1371/journal.pone.0184129. PMID: 28873455; PMCID: PMC5584762.
57. Wilk AJ, Shalek AK, Holmes S, Blish CA. Comparative analysis of cell-cell communication at single-cell resolution. Nat Biotechnol. 2024 Mar;42(3):470-483. doi: 10.1038/s41587-023-01782-z. Epub 2023 May 11. PMID: 37169965; PMCID: PMC10638471.
58. Qadiri M, Liu Y, Kim AR, Han M, Zhou E, Veal A, Lu TC, Li H, Hu Y, Perrimon N. FlyPhoneDB2: A computational framework for analyzing cell-cell communication in *Drosophila* scRNA-seq data integrating AlphaFold-multimer predictions. Comput Struct Biotechnol J. 2025 Jun 20;27:2814-2822. doi: 10.1016/j.csbj.2025.06.032. PMID: 40677242; PMCID: PMC12269837.
59. Byron A, Morgan MR, Humphries MJ. Adhesion signalling complexes. Curr Biol. 2010 Dec 21;20(24):R1063-R1067. doi: 10.1016/j.cub.2010.10.059. PMID: 21172621; PMCID: PMC4241715.
60. Bulgakova NA, Klapholz B, Brown NH. Cell adhesion in Drosophila: versatility of cadherin and integrin complexes during development. Curr Opin Cell Biol. 2012 Oct;24(5):702-12. doi: 10.1016/j.ceb.2012.07.006. Epub 2012 Aug 28. PMID: 22938782; PMCID: PMC3879911.
61. Xu C, Li Z, Lyu C, Hu Y, McLaughlin CN, Wong KKL, Xie Q, Luginbuhl DJ, Li H, Udeshi ND, Svinkina T, Mani DR, Han S, Li T, Li Y, Guajardo R, Ting AY, Carr SA, Li J, Luo L. Molecular and cellular mechanisms of teneurin signaling in synaptic partner matching. Cell. 2024 Sep 5;187(18):5081-5101.e19. doi: 10.1016/j.cell.2024.06.022. Epub 2024 Jul 11. PMID: 38996528; PMCID: PMC11833509.
62. Elmariah SB, Hughes EG, Oh EJ, Balice-Gordon RJ. Neurotrophin signaling among neurons and glia during formation of tripartite synapses. Neuron Glia Biol. 2004 Nov;1(4):1-11. doi: 10.1017/S1740925X05000189. PMID: 16528404; PMCID: PMC1397704.
63. Lin YC, Koleske AJ. Mechanisms of synapse and dendrite maintenance and their disruption in psychiatric and neurodegenerative disorders. Annu Rev Neurosci. 2010;33:349-78. doi: 10.1146/annurev-neuro-060909-153204. PMID: 20367247; PMCID: PMC3063389.

64. Silies M, Klämbt C. Adhesion and signaling between neurons and glial cells in Drosophila. Curr Opin Neurobiol. 2011 Feb;21(1):11-6. doi: 10.1016/j.conb.2010.08.011. Epub 2010 Sep 9. PMID: 20832289.
65. Tan L, Zhang KX, Pecot MY, Nagarkar-Jaiswal S, Lee PT, Takemura SY, McEwen JM, Nern A, Xu S, Tadros W, Chen Z, Zinn K, Bellen HJ, Morey M, Zipursky SL. Ig Superfamily Ligand and Receptor Pairs Expressed in Synaptic Partners in Drosophila. Cell. 2015 Dec 17;163(7):1756-69. doi: 10.1016/j.cell.2015.11.021. PMID: 26687360; PMCID: PMC4804707.
66. Kim HN, Ruan Y, Ogana H, Kim YM. Cadherins, Selectins, and Integrins in CAM-DR in Leukemia. Front Oncol. 2020 Dec 10;10:592733. doi: 10.3389/fonc.2020.592733. PMID: 33425742; PMCID: PMC7793796.
67. Banerjee S, Vernon S, Jiao W, Choi BJ, Ruchti E, Asadzadeh J, Burri O, Stowers RS, McCabe BD. Miniature neurotransmission is required to maintain Drosophila synaptic structures during ageing. Nat Commun. 2021 Jul 20;12(1):4399. doi: 10.1038/s41467-021-24490-1. PMID: 34285221; PMCID: PMC8292383.
68. Banerjee S, Vernon S, Ruchti E, Limoni G, Jiao W, Asadzadeh J, Van Campenhoudt M, McCabe BD. Trio preserves motor synapses and prolongs motor ability during aging. Cell Rep. 2024 Jun 25;43(6):114256. doi: 10.1016/j.celrep.2024.114256. Epub 2024 May 24. PMID: 38795343.
69. Cho S, Muthukumar AK, Stork T, Coutinho-Budd JC, Freeman MR. Focal adhesion molecules regulate astrocyte morphology and glutamate transporters to suppress seizure-like behavior. Proc Natl Acad Sci U S A. 2018 Oct 30;115(44):11316-11321. doi: 10.1073/pnas.1800830115. Epub 2018 Oct 16. PMID: 30327343; PMCID: PMC6217442.
70. Bittern J, Pogodalla N, Ohm H, Brüser L, Kottmeier R, Schirmeier S, Klämbt C. Neuron-glia interaction in the Drosophila nervous system. Dev Neurobiol. 2021 Jul;81(5):438-452. doi: 10.1002/dneu.22737. Epub 2020 Mar 4. PMID: 32096904.
71. Hillen AEJ, Burbach JPH, Hol EM. Cell adhesion and matricellular support by astrocytes of the tripartite synapse. Prog Neurobiol. 2018 Jun-Aug;165-167:66-86. doi: 10.1016/j.pneurobio.2018.02.002. Epub 2018 Feb 11. PMID: 29444459.
72. Chen J, Stork T, Kang Y, Nardone KAM, Auer F, Farrell RJ, Jay TR, Heo D, Sheehan A, Paton C, Nagel KI, Schoppik D, Monk KR, Freeman MR. Astrocyte growth is driven by the Tre1/S1pr1 phospholipid-binding G protein-coupled receptor. Neuron. 2024 Jan 3;112(1):93-112.e10. doi: 10.1016/j.neuron.2023.11.008. Epub 2023 Dec 13. PMID: 38096817; PMCID: PMC11073822.
73. Grumet M, Edelman GM. Neuron-glia cell adhesion molecule interacts with neurons and astroglia via different binding mechanisms. J Cell Biol. 1988 Feb;106(2):487-503. doi: 10.1083/jcb.106.2.487. PMID: 2448316; PMCID: PMC2114985.
74. Lepeta K, Lourenco MV, Schweitzer BC, Martino Adami PV, Banerjee P, Catuara-Solarz S, de La Fuente Revenga M, Guillem AM, Haidar M, Ijomone OM, Nadorp B, Qi L, Perera ND, Refsgaard LK, Reid KM, Sabbar M, Sahoo A, Schaefer N, Sheean RK, Suska A, Verma R, Vicidomini C, Wright D, Zhang XD, Seidenbecher C. Synaptopathies: synaptic dysfunction in neurological disorders - A review from students to students. J Neurochem. 2016 Sep;138(6):785-805. doi: 10.1111/jnc.13713. Epub 2016 Sep 8. PMID: 27333343; PMCID: PMC5095804.
75. Chou VT, Johnson SA, Van Vactor D. Synapse development and maturation at the drosophila neuromuscular junction. Neural Dev. 2020 Aug 2;15(1):11. doi: 10.1186/s13064-020-00147-5. PMID: 32741370; PMCID: PMC7397595.
76. Xu C, Theisen E, Maloney R, Peng J, Santiago I, Yapp C, Werkhoven Z, Rumbaut E, Shum B, Tarnogorska D, Borycz J, Tan L, Courgeon M, Griffin T, Levin R, Meinertzhagen IA, de Bivort B, Drugowitsch J, Pecot MY. Control of Synaptic Specificity by Establishing

a Relative Preference for Synaptic Partners. Neuron. 2019 Sep 4;103(5):865-877.e7. doi: 10.1016/j.neuron.2019.06.006. Epub 2019 Jul 9. Erratum in: Neuron. 2020 Apr 22;106(2):355. doi: 10.1016/j.neuron.2020.04.007. PMID: 31300277; PMCID: PMC6728174.

77. Honig B, Shapiro L. Adhesion Protein Structure, Molecular Affinities, and Principles of Cell-Cell Recognition. Cell. 2020 Apr 30;181(3):520-535. doi: 10.1016/j.cell.2020.04.010. PMID: 32359436; PMCID: PMC7233459.
78. Ahmad M, Li W, Top D. Integration of Circadian Clock Information in the *Drosophila* Circadian Neuronal Network. J Biol Rhythms. 2021 Jun;36(3):203-220. doi: 10.1177/0748730421993953. Epub 2021 Mar 1. PMID: 33641476; PMCID: PMC8114447.
79. Madetko N, Marzec W, Kowalska A, Przewodowska D, Alster P, Koziorowski D. Anti-IgLON5 Disease - The Current State of Knowledge and Further Perspectives. Front Immunol. 2022 Mar 1;13:852215. doi: 10.3389/fimmu.2022.852215. PMID: 35300333; PMCID: PMC8921982.
80. Zhang YH, Ni Y, Gao YN, Shen DD, He L, Yin D, Meng HY, Zhou QM, Hu J, Chen S. Anti-IgLON5 disease: a novel topic beyond neuroimmunology. Neural Regen Res. 2023 May;18(5):1017-1022. doi: 10.4103/1673-5374.355742. PMID: 36254983; PMCID: PMC9827781.
81. Artiushin G, Zhang SL, Tricoire H, Sehgal A. Endocytosis at the *Drosophila* blood-brain barrier as a function for sleep. Elife. 2018 Nov 26;7:e43326. doi: 10.7554/eLife.43326. PMID: 30475209; PMCID: PMC6255390.
82. Moulton MJ, Barish S, Ralhan I, Chang J, Goodman LD, Harland JG, Marcogliese PC, Johansson JO, Ioannou MS, Bellen HJ. Neuronal ROS-induced glial lipid droplet formation is altered by loss of Alzheimer's disease-associated genes. Proc Natl Acad Sci U S A. 2021 Dec 28;118(52):e2112095118. doi: 10.1073/pnas.2112095118. PMID: 34949639; PMCID: PMC8719885.
83. Axelrod S, Li X, Sun Y, Lincoln S, Terceros A, O'Neil J, Wang Z, Nguyen A, Vora A, Spicer C, Shapiro B, Young MW. The *Drosophila* blood-brain barrier regulates sleep via Moody G protein-coupled receptor signaling. Proc Natl Acad Sci U S A. 2023 Oct 17;120(42):e2309331120. doi: 10.1073/pnas.2309331120. Epub 2023 Oct 13. PMID: 37831742; PMCID: PMC10589661.
84. Contreras EG, Klämbt C. The Drosophila blood-brain barrier emerges as a model for understanding human brain diseases. Neurobiol Dis. 2023 May;180:106071. doi: 10.1016/j.nbd.2023.106071. Epub 2023 Mar 9. PMID: 36898613.
85. Hartenstein V. Morphological diversity and development of glia in Drosophila. Glia. 2011 Sep;59(9):1237-52. doi: 10.1002/glia.21162. Epub 2011 Mar 24. PMID: 21438012; PMCID: PMC3950653.
86. Jourjine, N.; Hoekstra, H.E. Expanding evolutionary neuroscience: insights from comparing variation in behavior. *Neuron*. **2021**, *109(7)*, 1084-1099.
87. Giansanti MG, Piergentili R. *Drosophila*: A Versatile Model in Biology and Medicine. Int J Mol Sci. 2025 May 23;26(11):5032. doi: 10.3390/ijms26115032. PMID: 40507842; PMCID: PMC12154199.
88. Bauer, J.H., Goupil, S., Garber, G.B., Helfand, S.L. An accelerated assay for the identification of lifespan-extending interventions in Drosophila melanogaster. Proc Natl Acad Sci U S A. 2004 Aug 31;101(35):12980-5. doi: 10.1073/pnas.0403493101. Epub 2004 Aug 24. PMID: 15328413; PMCID: PMC516504.
89. Han C, Jan LY, Jan YN. Enhancer-driven membrane markers for analysis of nonautonomous mechanisms reveal neuron-glia interactions in Drosophila. Proc Natl Acad Sci U S A. 2011 Jun 7;108(23):9673-8. doi: 10.1073/pnas.1106386108. Epub 2011 May 23. PMID: 21606367; PMCID: PMC3111288.

90. Lee T, Luo L. Mosaic analysis with a repressible cell marker for studies of gene function in neuronal morphogenesis. Neuron. 1999 Mar;22(3):451-61. doi: 10.1016/s0896-6273(00)80701-1. PMID: 10197526.
91. Guo J, Guo S, Lu S, Gong J, Wang L, Ding L, Chen Q, Liu W. The development of proximity labeling technology and its applications in mammals, plants, and microorganisms. Cell Commun Signal. 2023 Sep 30;21(1):269. doi: 10.1186/s12964-023-01310-1. Erratum in: Cell Commun Signal. 2024 Aug 16;22(1):403. doi: 10.1186/s12964-024-01750-3. PMID: 37777761; PMCID: PMC10544124.
92. Peng X, Clements J, Jiang Z, Han S, Preibisch S, Li J. PEELing: an integrated and user-centric platform for spatially resolved proteomics data analysis. Bioinformatics. 2025 Aug 2;41(8):btaf439. doi: 10.1093/bioinformatics/btaf439. PMID: 40794857; PMCID: PMC12343102.
93. Wickham et al., (2019). Welcome to the tidyverse. Journal of Open Source Software, 4(43), 1686, https://doi.org/10.21105/joss.01686
94. Kassambara A (2023). *ggpubr: 'ggplot2' Based Publication Ready Plots*. R package version 0.6.0, https://rpkgs.datanovia.com/ggpubr/.
95. Gustavsen JA, Pai S, Isserlin R et al. RCy3: Network biology using Cytoscape from within R [version 3; peer review: 3 approved]. F1000Research 2019, 8:1774 (https://doi.org/10.12688/f1000research.20887.3)
96. Chin CH, Chen SH, Wu HH, Ho CW, Ko MT, Lin CY. cytoHubba: identifying hub objects and sub-networks from complex interactome. BMC Syst Biol. 2014;8 Suppl 4(Suppl 4):S11. doi: 10.1186/1752-0509-8-S4-S11. Epub 2014 Dec 8. PMID: 25521941; PMCID: PMC4290687.
97. Wickham H (2016). *ggplot2: Elegant Graphics for Data Analysis*. Springer-Verlag New York. ISBN 978-3-319-24277-4, https://ggplot2.tidyverse.org.
98. Slowikowski K (2024). *ggrepel: Automatically Position Non-Overlapping Text Labels with 'ggplot2'*. https://ggrepel.slowkow.com/, https://github.com/slowkow/ggrepel.
99. Wu JS, Luo L. A protocol for dissecting Drosophila melanogaster brains for live imaging or immunostaining. Nat Protoc. 2006;1(4):2110-5. doi: 10.1038/nprot.2006.336. PMID: 17487202.
100. Kelly SM, Elchert A, Kahl M. Dissection and Immunofluorescent Staining of Mushroom Body and Photoreceptor Neurons in Adult Drosophila melanogaster Brains. J Vis Exp. 2017 Nov 6;(129):56174. doi: 10.3791/56174. PMID: 29155751; PMCID: PMC5755316.
101. Schneider CA, Rasband WS, Eliceiri KW. NIH Image to ImageJ: 25 years of image analysis. Nat Methods. 2012 Jul;9(7):671-5. doi: 10.1038/nmeth.2089. PMID: 22930834; PMCID: PMC5554542.
102. Schindelin J, Arganda-Carreras I, Frise E, Kaynig V, Longair M, Pietzsch T, Preibisch S, Rueden C, Saalfeld S, Schmid B, Tinevez JY, White DJ, Hartenstein V, Eliceiri K, Tomancak P, Cardona A. Fiji: an open-source platform for biological-image analysis. Nat Methods. 2012 Jun 28;9(7):676-82. doi: 10.1038/nmeth.2019. PMID: 22743772; PMCID: PMC3855844.
103. Goodman LD, Cope H, Nil Z, Ravenscroft TA, Charng WL, Lu S, Tien AC, Pfundt R, Koolen DA, Haaxma CA, Veenstra-Knol HE, Wassink-Ruiter JSK, Wevers MR, Jones M, Walsh LE, Klee VH, Theunis M, Legius E, Steel D, Barwick KES, Kurian MA, Mohammad SS, Dale RC, Terhal PA, van Binsbergen E, Kirmse B, Robinette B, Cogné B, Isidor B, Grebe TA, Kulch P, Hainline BE, Sapp K, Morava E, Klee EW, Macke EL, Trapane P, Spencer C, Si Y, Begtrup A, Moulton MJ, Dutta D, Kanca O; Undiagnosed Diseases Network; Wangler MF, Yamamoto S, Bellen HJ, Tan QK. TNPO2 variants associate with human developmental delays, neurologic deficits, and dysmorphic features

and alter TNPO2 activity in Drosophila. Am J Hum Genet. 2021 Sep 2;108(9):1669-1691. doi: 10.1016/j.ajhg.2021.06.019. Epub 2021 Jul 26. PMID: 34314705; PMCID: PMC8456166.

104. Ali YO, Escala W, Ruan K, Zhai RG. Assaying locomotor, learning, and memory deficits in Drosophila models of neurodegeneration. J Vis Exp. 2011 Mar 11;(49):2504. doi: 10.3791/2504. PMID: 21445036; PMCID: PMC3197301.

105. Burns MP, Cavallaro FD, Saltz JB. Does Divergence in Habitat Breadth Associate with Species Differences in Decision Making in *Drosophila Sechellia* and *Drosophila Simulans*? Genes (Basel). 2020 May 9;11(5):528. doi: 10.3390/genes11050528. PMID: 32397481; PMCID: PMC7288451.

106. Burns, M.P., Saltz, J.B. Species differences in learning about gustatory and visual stimuli in two recently diverged species of *Drosophila*. *Animal Behaviour* **2024**, *215*, 177-190.

107. Goodman LD, Prudencio M, Kramer NJ, Martinez-Ramirez LF, Srinivasan AR, Lan M, Parisi MJ, Zhu Y, Chew J, Cook CN, Berson A, Gitler AD, Petrucelli L, Bonini NM. Toxic expanded GGGGCC repeat transcription is mediated by the PAF1 complex in C9orf72-associated FTD. Nat Neurosci. 2019 Jun;22(6):863-874. doi: 10.1038/s41593-019-0396-1. Epub 2019 May 20. Erratum in: Nat Neurosci. 2023 Mar;26(3):528. doi: 10.1038/s41593-023-01274-y. PMID: 31110321; PMCID: PMC6535128.

108. Zheng GX, Terry JM, Belgrader P, Ryvkin P, Bent ZW, Wilson R, Ziraldo SB, Wheeler TD, McDermott GP, Zhu J, Gregory MT, Shuga J, Montesclaros L, Underwood JG, Masquelier DA, Nishimura SY, Schnall-Levin M, Wyatt PW, Hindson CM, Bharadwaj R, Wong A, Ness KD, Beppu LW, Deeg HJ, McFarland C, Loeb KR, Valente WJ, Ericson NG, Stevens EA, Radich JP, Mikkelsen TS, Hindson BJ, Bielas JH. Massively parallel digital transcriptional profiling of single cells. Nat Commun. 2017 Jan 16;8:14049. doi: 10.1038/ncomms14049. PMID: 28091601; PMCID: PMC5241818.

109. Thurmond J, Goodman JL, Strelets VB, Attrill H, Gramates LS, Marygold SJ, Matthews BB, Millburn G, Antonazzo G, Trovisco V, Kaufman TC, Calvi BR; FlyBase Consortium. FlyBase 2.0: the next generation. Nucleic Acids Res. 2019 Jan 8;47(D1):D759-D765. doi: 10.1093/nar/gky1003. PMID: 30364959; PMCID: PMC6323960.

110. Fleming SJ, Chaffin MD, Arduini A, Akkad AD, Banks E, Marioni JC, Philippakis AA, Ellinor PT, Babadi M. Unsupervised removal of systematic background noise from droplet-based single-cell experiments using CellBender. Nat Methods. 2023 Sep;20(9):1323-1335. doi: 10.1038/s41592-023-01943-7. Epub 2023 Aug 7. PMID: 37550580.

111. Germain PL, Lun A, Garcia Meixide C, Macnair W, Robinson MD. Doublet identification in single-cell sequencing data using *scDblFinder*. F1000Res. 2021 Sep 28;10:979. doi: 10.12688/f1000research.73600.2. PMID: 35814628; PMCID: PMC9204188.

112. Luecken MD, Theis FJ. Current best practices in single-cell RNA-seq analysis: a tutorial. Mol Syst Biol. 2019 Jun 19;15(6):e8746. doi: 10.15252/msb.20188746. PMID: 31217225; PMCID: PMC6582955.

113. Ilicic T, Kim JK, Kolodziejczyk AA, Bagger FO, McCarthy DJ, Marioni JC, Teichmann SA. Classification of low quality cells from single-cell RNA-seq data. Genome Biol. 2016 Feb 17;17:29. doi: 10.1186/s13059-016-0888-1. PMID: 26887813; PMCID: PMC4758103.

114. Korsunsky I, Millard N, Fan J, Slowikowski K, Zhang F, Wei K, Baglaenko Y, Brenner M, Loh PR, Raychaudhuri S. Fast, sensitive and accurate integration of single-cell data with Harmony. Nat Methods. 2019 Dec;16(12):1289-1296. doi: 10.1038/s41592-019-0619-0. Epub 2019 Nov 18. PMID: 31740819; PMCID: PMC6884693.

115. Stuart T, Butler A, Hoffman P, Hafemeister C, Papalexi E, Mauck WM 3rd, Hao Y, Stoeckius M, Smibert P, Satija R. Comprehensive Integration of Single-Cell Data. Cell. 2019 Jun 13;177(7):1888-1902.e21. doi: 10.1016/j.cell.2019.05.031. Epub 2019 Jun 6. PMID: 31178118; PMCID: PMC6687398.
116. Traag VA, Waltman L, van Eck NJ. From Louvain to Leiden: guaranteeing well-connected communities. Sci Rep. 2019 Mar 26;9(1):5233. doi: 10.1038/s41598-019-41695-z. PMID: 30914743; PMCID: PMC6435756.
117. Wolf FA, Angerer P, Theis FJ. SCANPY: large-scale single-cell gene expression data analysis. Genome Biol. 2018 Feb 6;19(1):15. doi: 10.1186/s13059-017-1382-0. PMID: 29409532; PMCID: PMC5802054.
118. Yu G, Wang LG, Han Y, He QY. clusterProfiler: an R package for comparing biological themes among gene clusters. OMICS. 2012 May;16(5):284-7. doi: 10.1089/omi.2011.0118. Epub 2012 Mar 28. PMID: 22455463; PMCID: PMC3339379.
119. Kanehisa M, Goto S. KEGG: kyoto encyclopedia of genes and genomes. Nucleic Acids Res. 2000 Jan 1;28(1):27-30. doi: 10.1093/nar/28.1.27. PMID: 10592173; PMCID: PMC102409.

Supplemental Figure S1 to S9

Figure legends for Figure S1 to S9

Table legends for Supplementary Table 1 to 3

Fig. S1

A

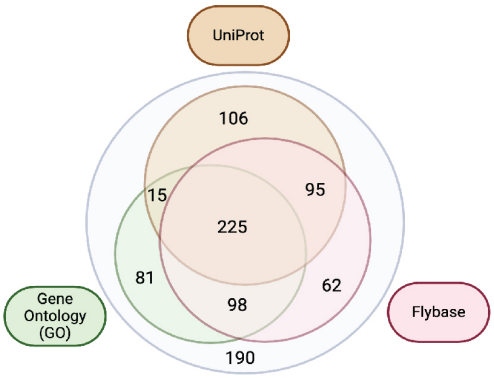

Total proteins identified: **872**
Total proteins validated: **682**

B

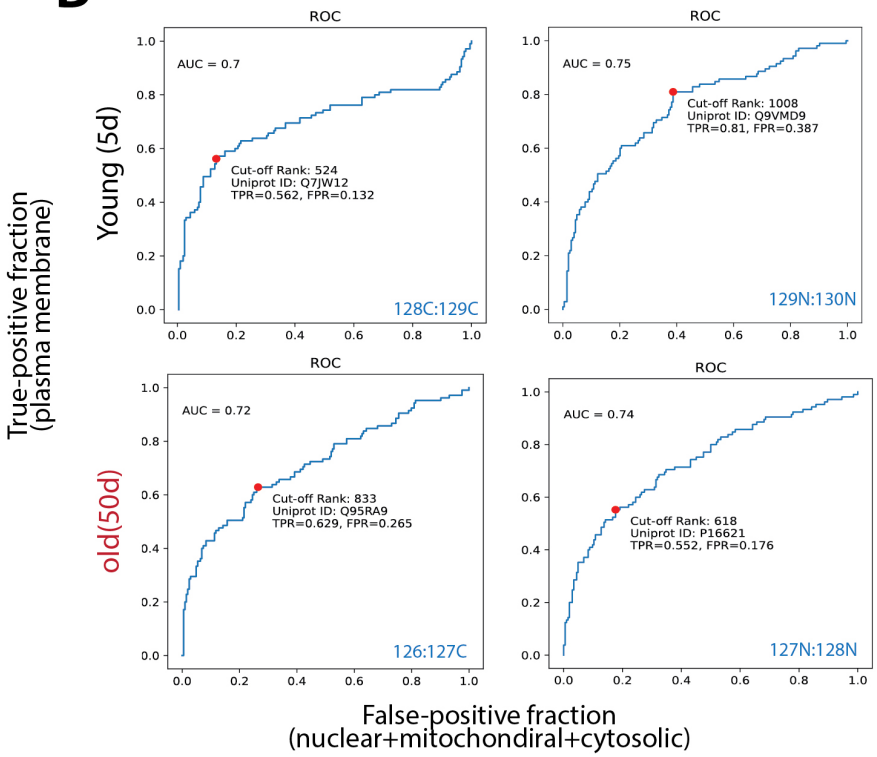

C

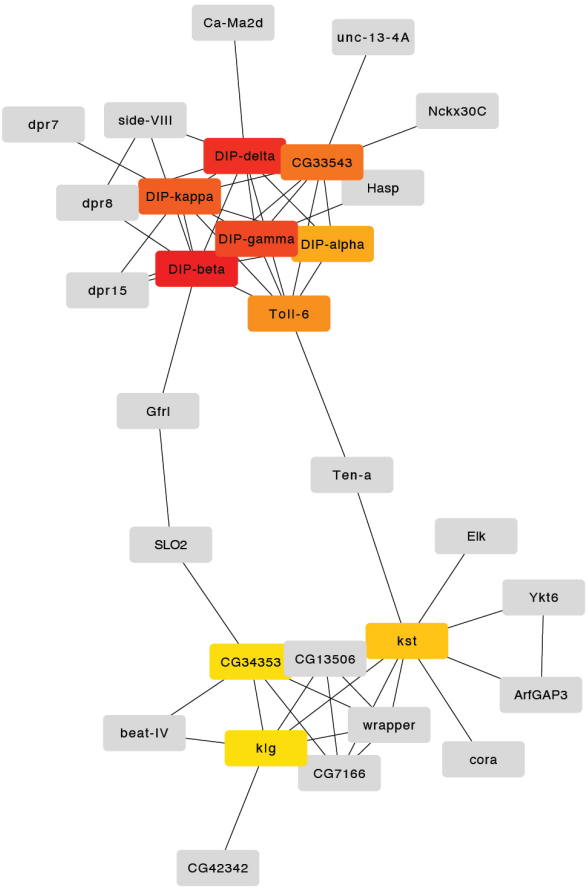

Hub Gene	Rank
DIP-beta	1
DIP-delta	2
DIP-gamma	3
DIP-kappa	4
CG33543	5
Toll-6	6
DIP-alpha	7
kst	8
klg	9
CG34353	9

Fig. S2

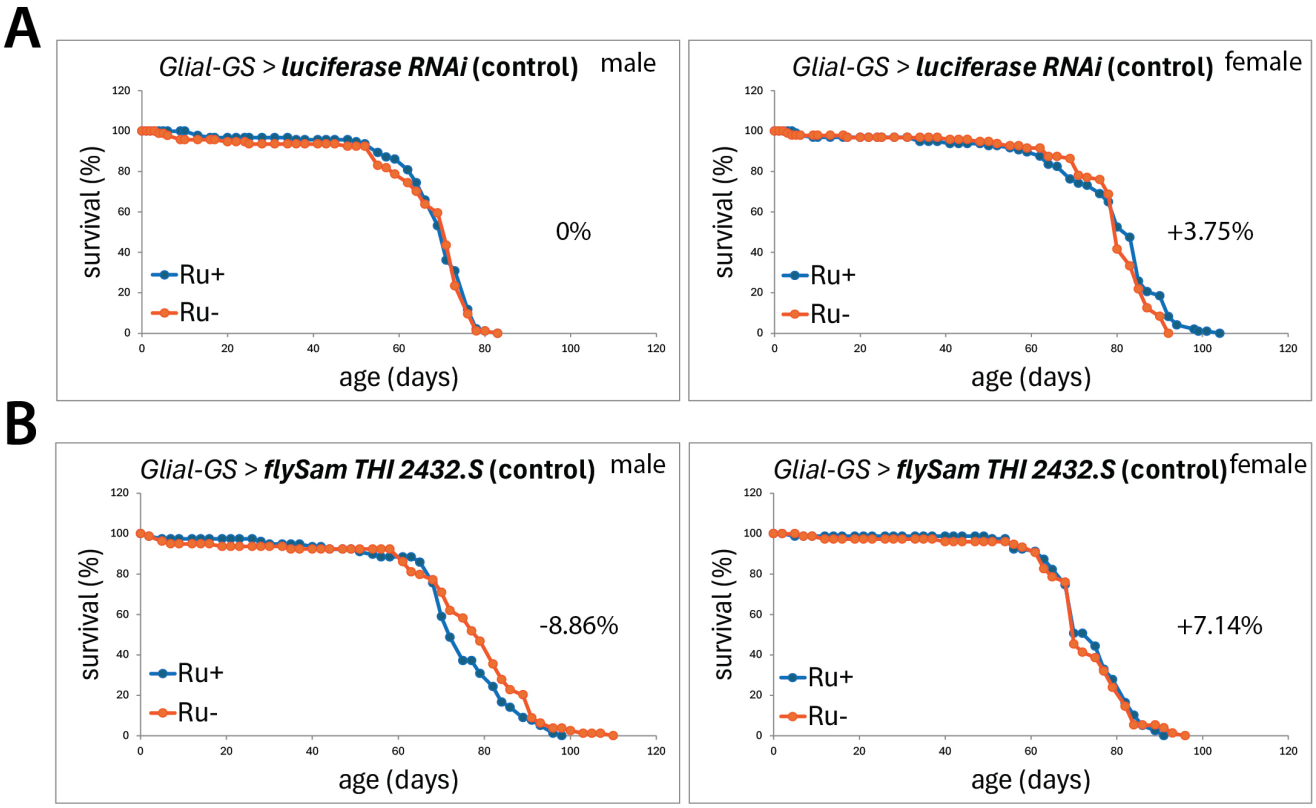
A
Glial-GS > luciferase RNAi (control)
male
survival (%)
age (days)
Ru+
Ru-
0%
Glial-GS > luciferase RNAi (control)
female
survival (%)
age (days)
Ru+
Ru-
+3.75%
B
Glial-GS > flySam THI 2432.S (control)
male
survival (%)
age (days)
Ru+
Ru-
-8.86%
Glial-GS > flySam THI 2432.S (control)
female
survival (%)
age (days)
Ru+
Ru-
+7.14%

Fig. S3

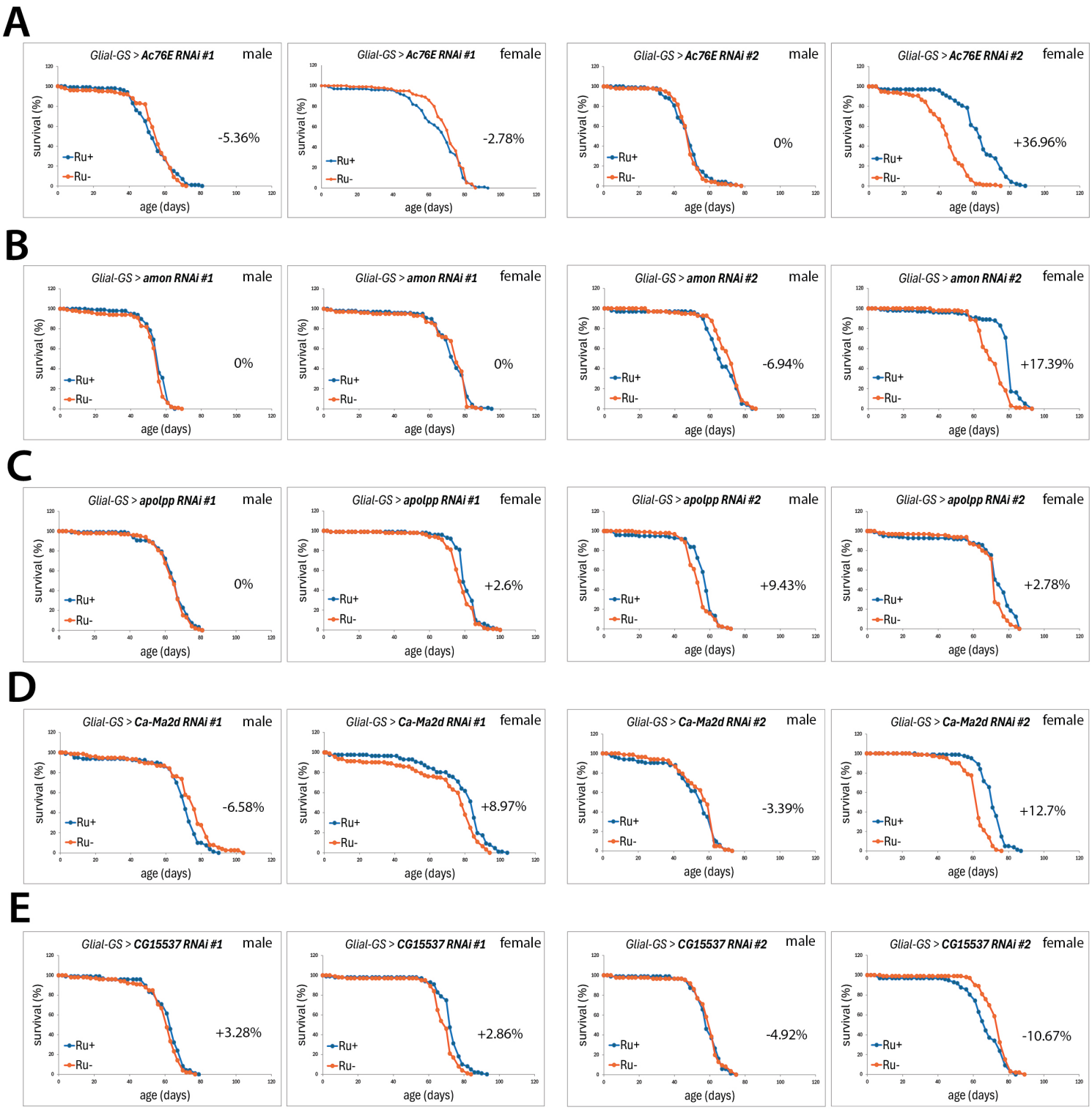
A
Glial-GS > Ac76E RNAi #1 male
-5.36%
Glial-GS > Ac76E RNAi #1 female
-2.78%
Glial-GS > Ac76E RNAi #2 male
0%
Glial-GS > Ac76E RNAi #2 female
+36.96%
B
Glial-GS > amon RNAi #1 male
0%
Glial-GS > amon RNAi #1 female
0%
Glial-GS > amon RNAi #2 male
-6.94%
Glial-GS > amon RNAi #2 female
+17.39%
C
Glial-GS > apolpp RNAi #1 male
0%
Glial-GS > apolpp RNAi #1 female
+2.6%
Glial-GS > apolpp RNAi #2 male
+9.43%
Glial-GS > apolpp RNAi #2 female
+2.78%
D
Glial-GS > Ca-Ma2d RNAi #1 male
-6.58%
Glial-GS > Ca-Ma2d RNAi #1 female
+8.97%
Glial-GS > Ca-Ma2d RNAi #2 male
-3.39%
Glial-GS > Ca-Ma2d RNAi #2 female
+12.7%
E
Glial-GS > CG15537 RNAi #1 male
+3.28%
Glial-GS > CG15537 RNAi #1 female
+2.86%
Glial-GS > CG15537 RNAi #2 male
-4.92%
Glial-GS > CG15537 RNAi #2 female
-10.67%
survival (%)
age (days)
Ru+
Ru-

Fig. S4

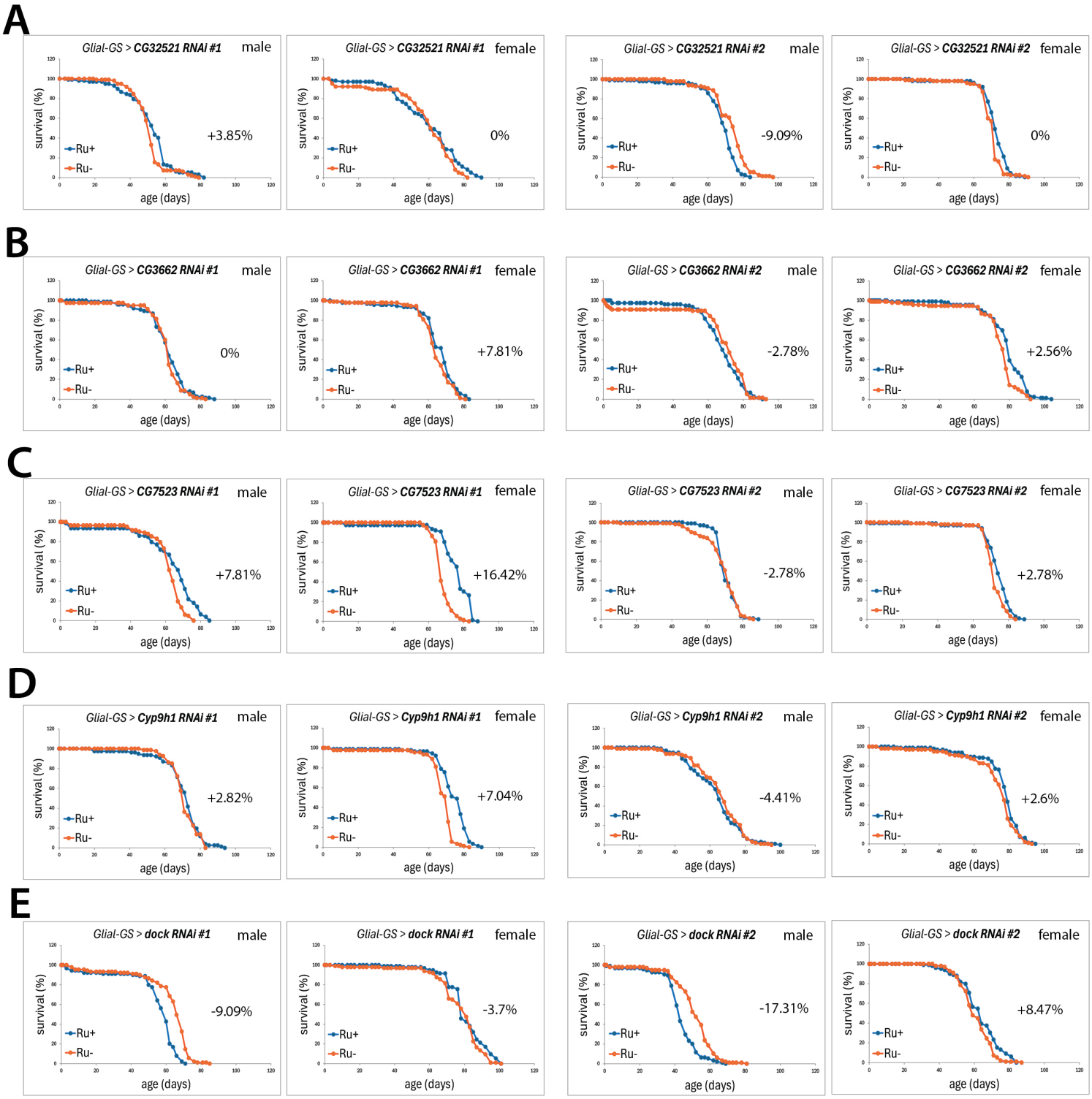
A
Glial-GS > CG32521 RNAi #1 male
+3.85%
Glial-GS > CG32521 RNAi #1 female
0%
Glial-GS > CG32521 RNAi #2 male
-9.09%
Glial-GS > CG32521 RNAi #2 female
0%
B
Glial-GS > CG3662 RNAi #1 male
0%
Glial-GS > CG3662 RNAi #1 female
+7.81%
Glial-GS > CG3662 RNAi #2 male
-2.78%
Glial-GS > CG3662 RNAi #2 female
+2.56%
C
Glial-GS > CG7523 RNAi #1 male
+7.81%
Glial-GS > CG7523 RNAi #1 female
+16.42%
Glial-GS > CG7523 RNAi #2 male
-2.78%
Glial-GS > CG7523 RNAi #2 female
+2.78%
D
Glial-GS > Cyp9h1 RNAi #1 male
+2.82%
Glial-GS > Cyp9h1 RNAi #1 female
+7.04%
Glial-GS > Cyp9h1 RNAi #2 male
-4.41%
Glial-GS > Cyp9h1 RNAi #2 female
+2.6%
E
Glial-GS > dock RNAi #1 male
-9.09%
Glial-GS > dock RNAi #1 female
-3.7%
Glial-GS > dock RNAi #2 male
-17.31%
Glial-GS > dock RNAi #2 female
+8.47%
survival (%)
age (days)
Ru+
Ru-

Fig. S5

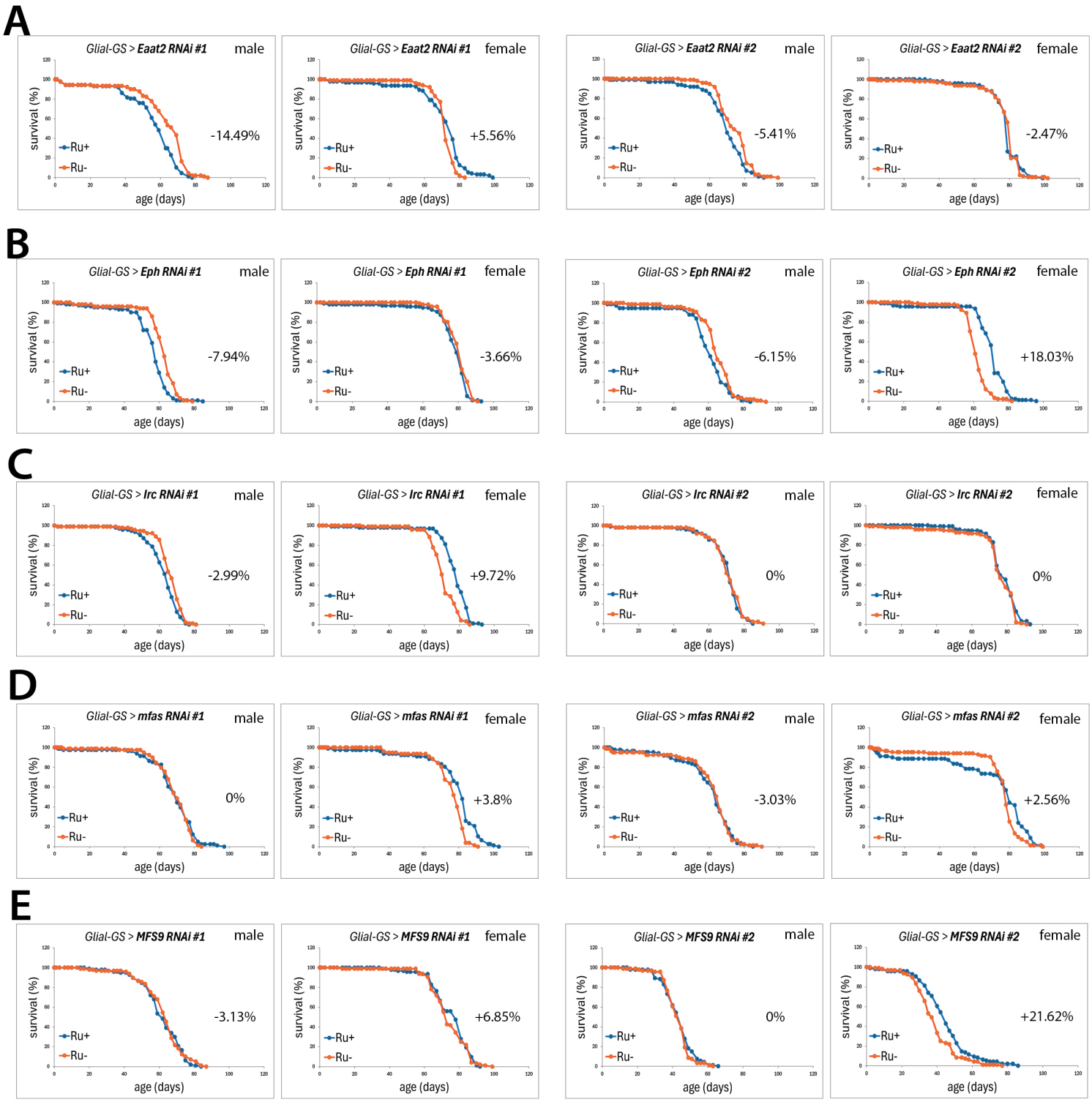
A
Glial-GS > Eaat2 RNAi #1 male
-14.49%
Glial-GS > Eaat2 RNAi #1 female
+5.56%
Glial-GS > Eaat2 RNAi #2 male
-5.41%
Glial-GS > Eaat2 RNAi #2 female
-2.47%
B
Glial-GS > Eph RNAi #1 male
-7.94%
Glial-GS > Eph RNAi #1 female
-3.66%
Glial-GS > Eph RNAi #2 male
-6.15%
Glial-GS > Eph RNAi #2 female
+18.03%
C
Glial-GS > Irc RNAi #1 male
-2.99%
Glial-GS > Irc RNAi #1 female
+9.72%
Glial-GS > Irc RNAi #2 male
0%
Glial-GS > Irc RNAi #2 female
0%
D
Glial-GS > mfas RNAi #1 male
0%
Glial-GS > mfas RNAi #1 female
+3.8%
Glial-GS > mfas RNAi #2 male
-3.03%
Glial-GS > mfas RNAi #2 female
+2.56%
E
Glial-GS > MFS9 RNAi #1 male
-3.13%
Glial-GS > MFS9 RNAi #1 female
+6.85%
Glial-GS > MFS9 RNAi #2 male
0%
Glial-GS > MFS9 RNAi #2 female
+21.62%
survival (%)
age (days)
Ru+
Ru-

Fig. S6

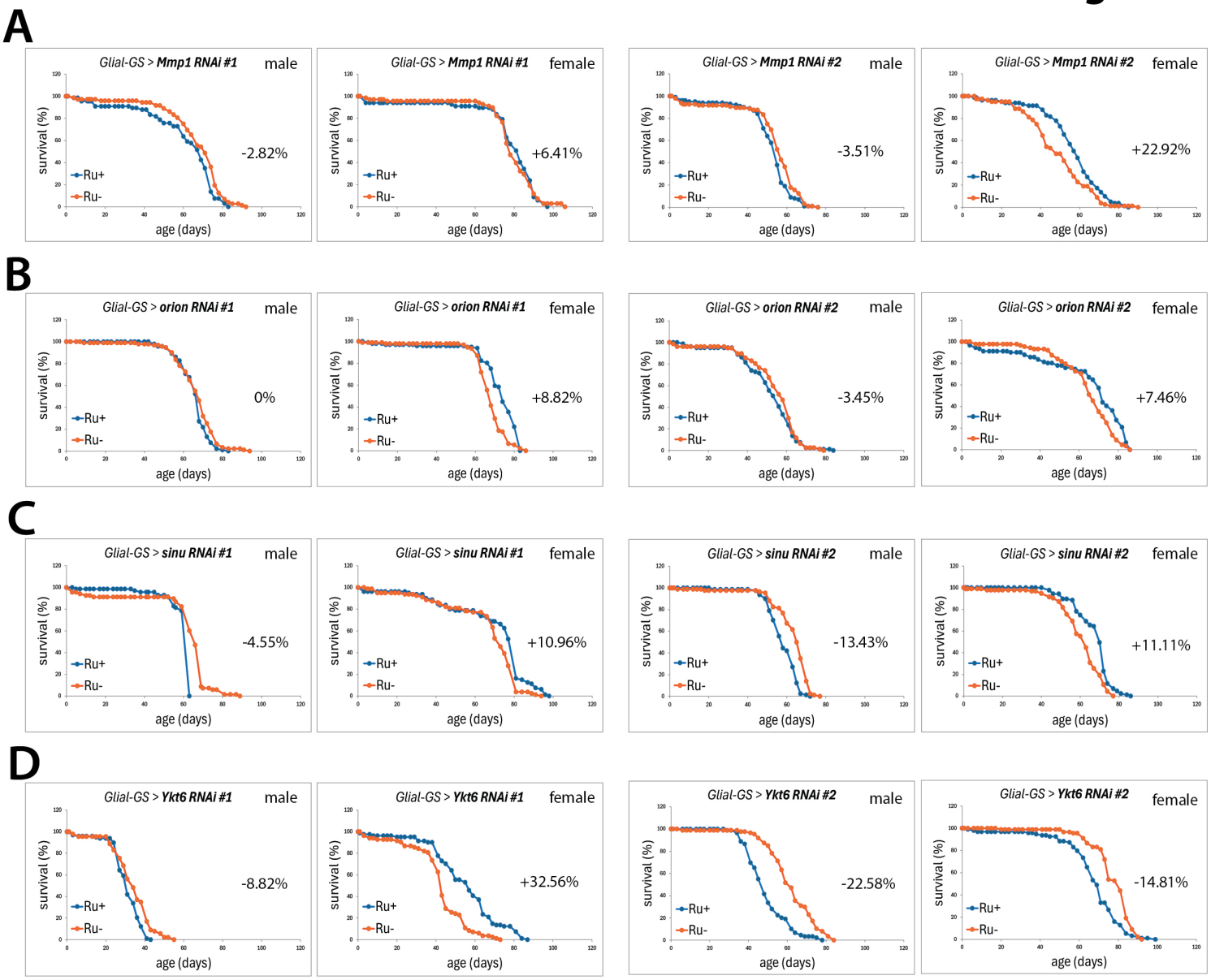
A
Glial-GS > Mmp1 RNAi #1 male
-2.82%
Glial-GS > Mmp1 RNAi #1 female
+6.41%
Glial-GS > Mmp1 RNAi #2 male
-3.51%
Glial-GS > Mmp1 RNAi #2 female
+22.92%
B
Glial-GS > orion RNAi #1 male
0%
Glial-GS > orion RNAi #1 female
+8.82%
Glial-GS > orion RNAi #2 male
-3.45%
Glial-GS > orion RNAi #2 female
+7.46%
C
Glial-GS > sinu RNAi #1 male
-4.55%
Glial-GS > sinu RNAi #1 female
+10.96%
Glial-GS > sinu RNAi #2 male
-13.43%
Glial-GS > sinu RNAi #2 female
+11.11%
D
Glial-GS > Ykt6 RNAi #1 male
-8.82%
Glial-GS > Ykt6 RNAi #1 female
+32.56%
Glial-GS > Ykt6 RNAi #2 male
-22.58%
Glial-GS > Ykt6 RNAi #2 female
-14.81%
survival (%)
age (days)
Ru+
Ru-

Fig. S7

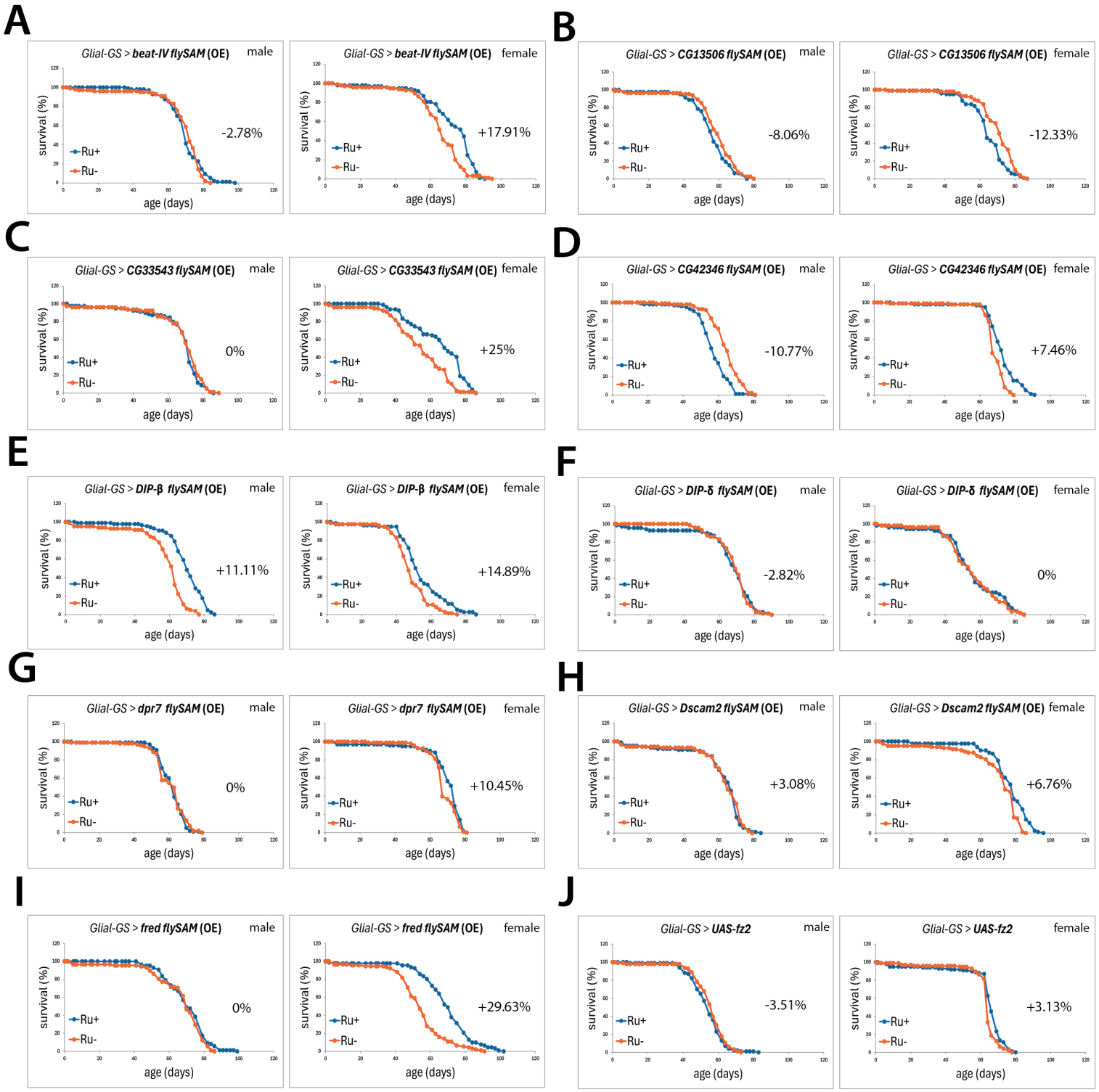
A
Glial-GS > beat-IV flySAM (OE) male
-2.78%
Glial-GS > beat-IV flySAM (OE) female
+17.91%
B
Glial-GS > CG13506 flySAM (OE) male
-8.06%
Glial-GS > CG13506 flySAM (OE) female
-12.33%
C
Glial-GS > CG33543 flySAM (OE) male
0%
Glial-GS > CG33543 flySAM (OE) female
+25%
D
Glial-GS > CG42346 flySAM (OE) male
-10.77%
Glial-GS > CG42346 flySAM (OE) female
+7.46%
E
Glial-GS > DIP-β flySAM (OE) male
+11.11%
Glial-GS > DIP-β flySAM (OE) female
+14.89%
F
Glial-GS > DIP-δ flySAM (OE) male
-2.82%
Glial-GS > DIP-δ flySAM (OE) female
0%
G
Glial-GS > dpr7 flySAM (OE) male
0%
Glial-GS > dpr7 flySAM (OE) female
+10.45%
H
Glial-GS > Dscam2 flySAM (OE) male
+3.08%
Glial-GS > Dscam2 flySAM (OE) female
+6.76%
I
Glial-GS > fred flySAM (OE) male
0%
Glial-GS > fred flySAM (OE) female
+29.63%
J
Glial-GS > UAS-fz2 male
-3.51%
Glial-GS > UAS-fz2 female
+3.13%
survival (%)
age (days)
Ru+
Ru-

Fig. S8

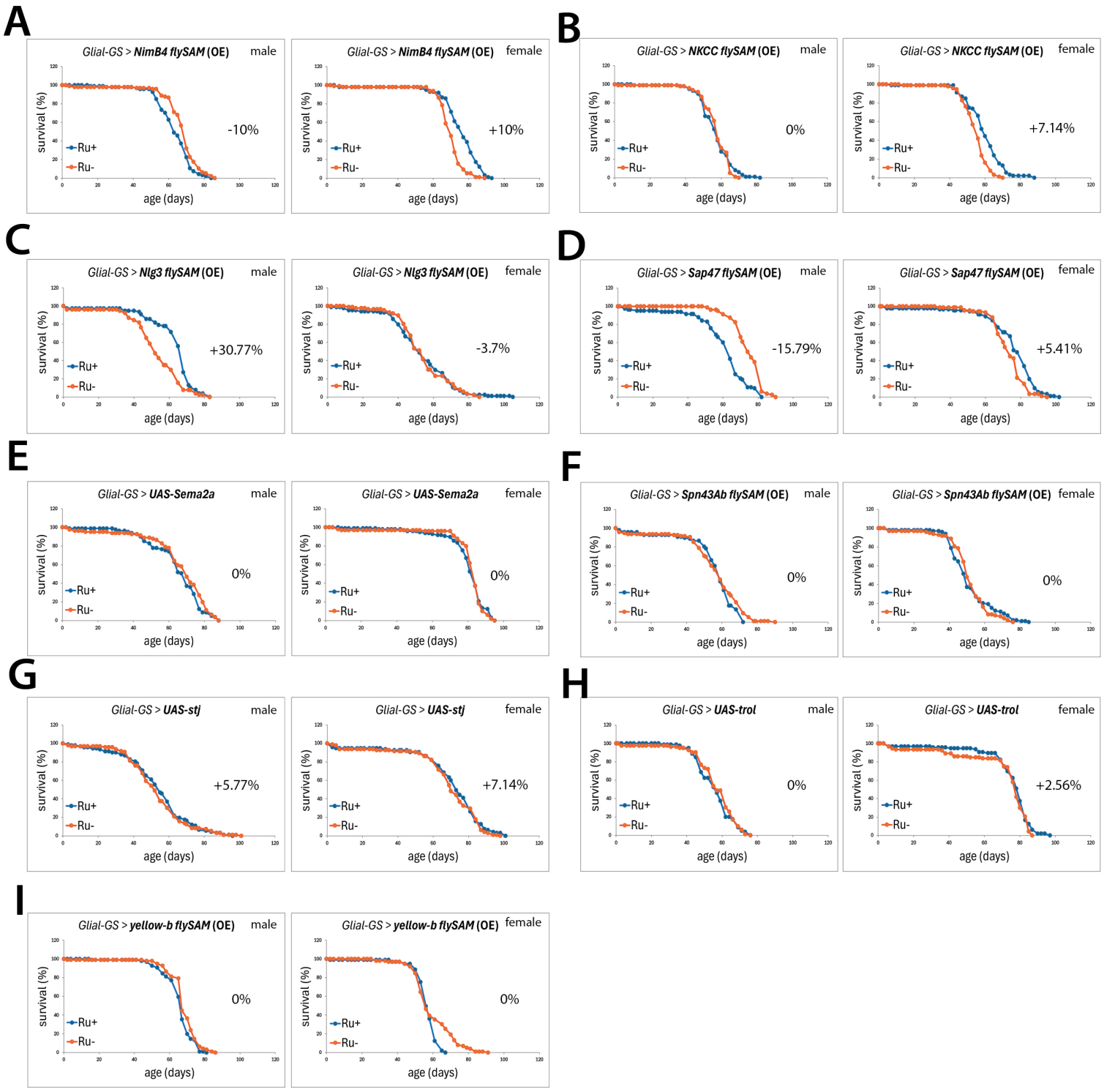
A
Glial-GS > NimB4 flySAM (OE) male
-10%
Glial-GS > NimB4 flySAM (OE) female
+10%
B
Glial-GS > NKCC flySAM (OE) male
0%
Glial-GS > NKCC flySAM (OE) female
+7.14%
C
Glial-GS > Nlg3 flySAM (OE) male
+30.77%
Glial-GS > Nlg3 flySAM (OE) female
-3.7%
D
Glial-GS > Sap47 flySAM (OE) male
-15.79%
Glial-GS > Sap47 flySAM (OE) female
+5.41%
E
Glial-GS > UAS-Sema2a male
0%
Glial-GS > UAS-Sema2a female
0%
F
Glial-GS > Spn43Ab flySAM (OE) male
0%
Glial-GS > Spn43Ab flySAM (OE) female
0%
G
Glial-GS > UAS-stj male
+5.77%
Glial-GS > UAS-stj female
+7.14%
H
Glial-GS > UAS-trol male
0%
Glial-GS > UAS-trol female
+2.56%
I
Glial-GS > yellow-b flySAM (OE) male
0%
Glial-GS > yellow-b flySAM (OE) female
0%
survival (%)
age (days)
Ru+
Ru-

Fig. S9

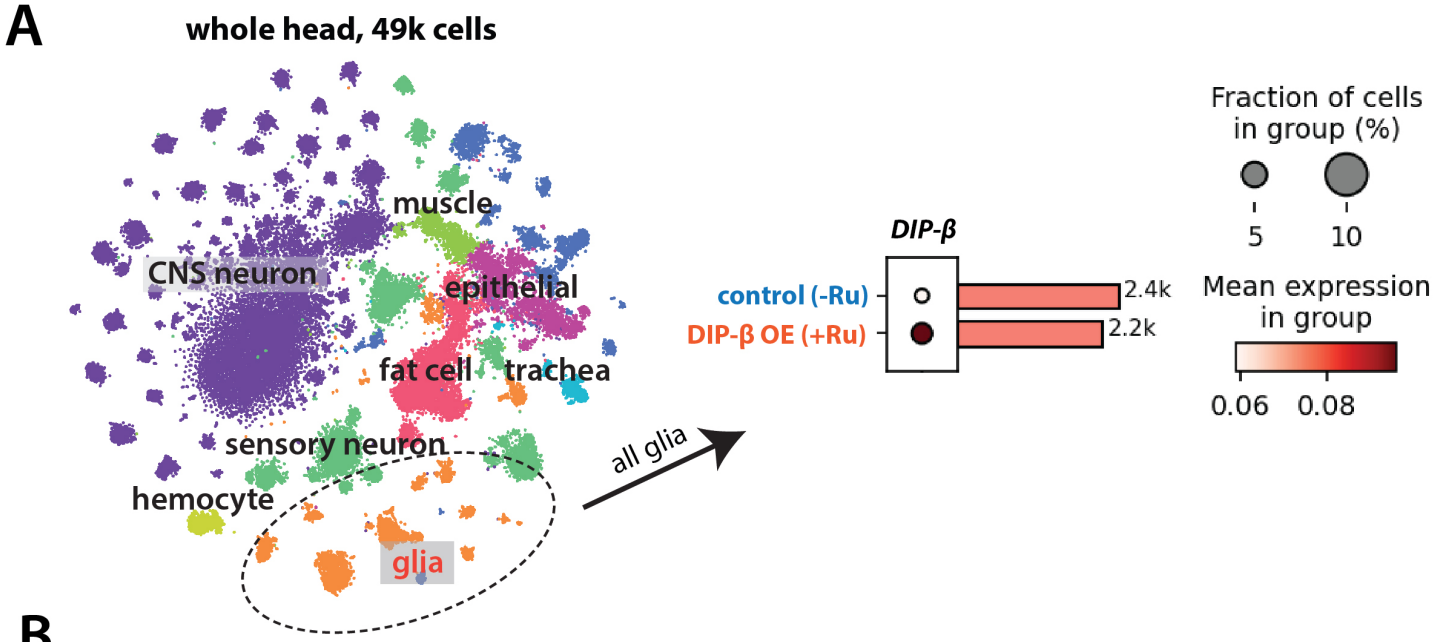
A
whole head, 49k cells
muscle
CNS neuron
epithelial
fat cell
trachea
sensory neuron
hemocyte
glia
all glia
DIP-β
control (-Ru)
DIP-β OE (+Ru)
2.4k
2.2k
Fraction of cells in group (%)
5
10
Mean expression in group
0.06
0.08

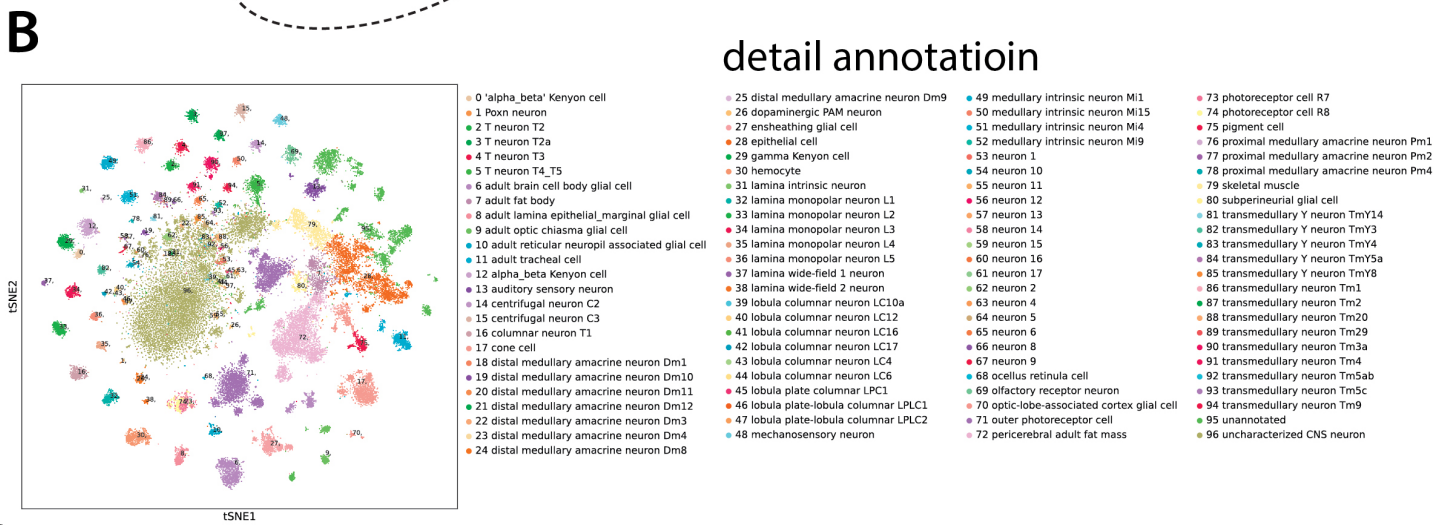
B
detail annotatioin
tSNE1
tSNE2
0 'alpha_beta' Kenyon cell
1 Poxn neuron
2 T neuron T2
3 T neuron T2a
4 T neuron T3
5 T neuron T4_T5
6 adult brain cell body glial cell
7 adult fat body
8 adult lamina epithelial_marginal glial cell
9 adult optic chiasma glial cell
10 adult reticular neuropil associated glial cell
11 adult tracheal cell
12 alpha_beta Kenyon cell
13 auditory sensory neuron
14 centrifugal neuron C2
15 centrifugal neuron C3
16 columnar neuron T1
17 cone cell
18 distal medullary amacrine neuron Dm1
19 distal medullary amacrine neuron Dm10
20 distal medullary amacrine neuron Dm11
21 distal medullary amacrine neuron Dm12
22 distal medullary amacrine neuron Dm3
23 distal medullary amacrine neuron Dm4
24 distal medullary amacrine neuron Dm8
25 distal medullary amacrine neuron Dm9
26 dopaminergic PAM neuron
27 ensheathing glial cell
28 epithelial cell
29 gamma Kenyon cell
30 hemocyte
31 lamina intrinsic neuron
32 lamina monopolar neuron L1
33 lamina monopolar neuron L2
34 lamina monopolar neuron L3
35 lamina monopolar neuron L4
36 lamina monopolar neuron L5
37 lamina wide-field 1 neuron
38 lamina wide-field 2 neuron
39 lobula columnar neuron LC10a
40 lobula columnar neuron LC12
41 lobula columnar neuron LC16
42 lobula columnar neuron LC17
43 lobula columnar neuron LC4
44 lobula columnar neuron LC6
45 lobula plate columnar LPC1
46 lobula plate-lobula columnar LPLC1
47 lobula plate-lobula columnar LPLC2
48 mechanosensory neuron
49 medullary intrinsic neuron Mi1
50 medullary intrinsic neuron Mi15
51 medullary intrinsic neuron Mi4
52 medullary intrinsic neuron Mi9
53 neuron 1
54 neuron 10
55 neuron 11
56 neuron 12
57 neuron 13
58 neuron 14
59 neuron 15
60 neuron 16
61 neuron 17
62 neuron 2
63 neuron 4
64 neuron 5
65 neuron 6
66 neuron 8
67 neuron 9
68 ocellus retinula cell
69 olfactory receptor neuron
70 optic-lobe-associated cortex glial cell
71 outer photoreceptor cell
72 pericerebral adult fat mass
73 photoreceptor cell R7
74 photoreceptor cell R8
75 pigment cell
76 proximal medullary amacrine neuron Pm1
77 proximal medullary amacrine neuron Pm2
78 proximal medullary amacrine neuron Pm4
79 skeletal muscle
80 subperineurial glial cell
81 transmedullary Y neuron TmY14
82 transmedullary Y neuron TmY3
83 transmedullary Y neuron TmY4
84 transmedullary Y neuron TmY5a
85 transmedullary Y neuron TmY8
86 transmedullary neuron Tm1
87 transmedullary neuron Tm2
88 transmedullary neuron Tm20
89 transmedullary neuron Tm29
90 transmedullary neuron Tm3a
91 transmedullary neuron Tm4
92 transmedullary neuron Tm5ab
93 transmedullary neuron Tm5c
94 transmedullary neuron Tm9
95 unannotated
96 uncharacterized CNS neuron

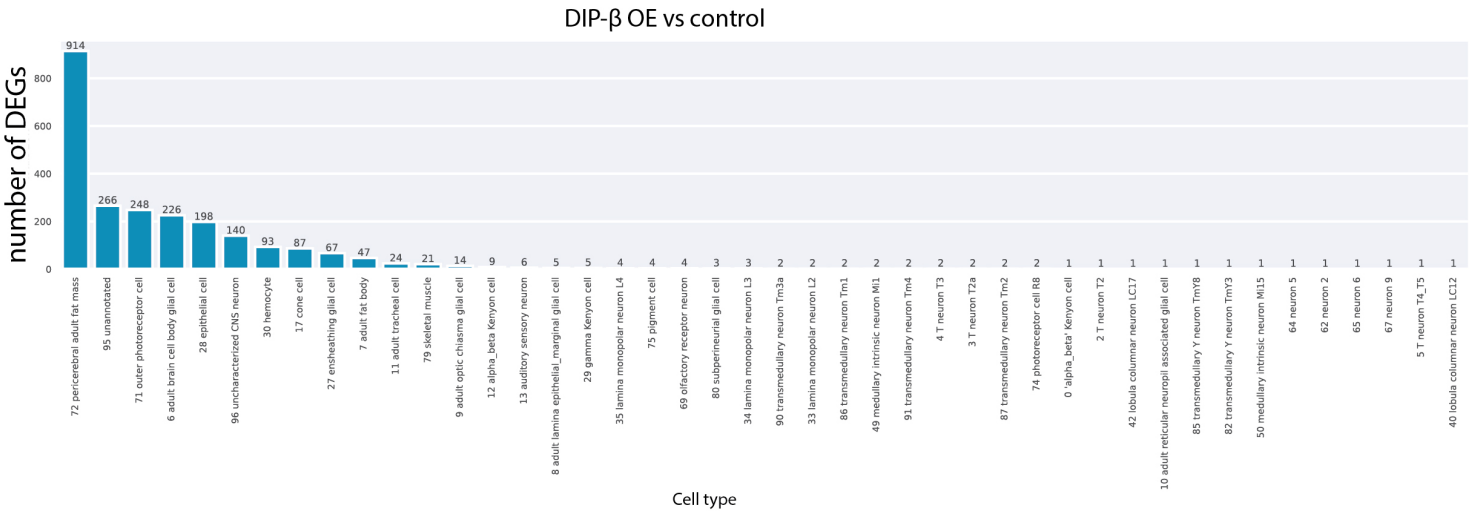
C
DIP-β OE vs control
number of DEGs
0
200
400
600
800
914
266
248
226
198
140
93
87
67
47
24
21
14
9
6
5
5
4
4
4
3
3
2
2
2
2
2
2
2
2
1
1
1
1
1
1
1
1
1
1
1
1
1
1
1
72 pericerebral adult fat mass
95 unannotated
71 outer photoreceptor cell
6 adult brain cell body glial cell
28 epithelial cell
96 uncharacterized CNS neuron
30 hemocyte
17 cone cell
27 ensheathing glial cell
7 adult fat body
11 adult tracheal cell
79 skeletal muscle
9 adult optic chiasma glial cell
12 alpha_beta Kenyon cell
13 auditory sensory neuron
8 adult lamina epithelial_marginal glial cell
29 gamma Kenyon cell
35 lamina monopolar neuron L4
75 pigment cell
69 olfactory receptor neuron
80 subperineurial glial cell
34 lamina monopolar neuron L3
90 transmedullary neuron Tm3a
33 lamina monopolar neuron L2
86 transmedullary neuron Tm1
49 medullary intrinsic neuron Mi1
91 transmedullary neuron Tm4
4 T neuron T3
3 T neuron T2a
87 transmedullary neuron Tm2
74 photoreceptor cell R8
0 'alpha_beta' Kenyon cell
2 T neuron T2
42 lobula columnar neuron LC17
10 adult reticular neuropil associated glial cell
85 transmedullary Y neuron TmY8
82 transmedullary Y neuron TmY3
50 medullary intrinsic neuron Mi15
64 neuron 5
62 neuron 2
65 neuron 6
67 neuron 9
5 T neuron T4_T5
40 lobula columnar neuron LC12
Cell type

Figure S1: Glial cell-surface proteomics

A: We searched the 872 proteins included in our proteomic profiles against three databases: FlyBase, UniProt, and the Gene Ontology Data Archive (DOI 10.5281/zenodo.1205166; Version 2023-05-10; Ashburner et al., 2000) to determine which proteins had previous plasma membrane or extracellular matrix annotations. We found the 682 out of the 872 proteins could be validated by at least one database, further validating the quality of our cell-surface proteomic labeling.

B: We plotted the receiver operating characteristic (ROC) curve for each biological replicate answer observed high specificity.

C: We identified the top 10 "hub" genes in our PPI network and found that of the top 10 hub genes identified, 7 had reported function in cell adhesion (klg, kst) and synaptic wiring (DIP-β, DIP-δ, DIP-γ, DIP-κ, DIP-α), while the remaining three had reported function in neuron projection (CG33543), axon guidance (CG34353), and dendrite guidance (Toll-6).

Figure S2: Functional screening of candidate genes.

A-C: In our initial functional lifespan screen, glial overexpression of DIP-β was found to significantly extend lifespan for both male and female flies, compared to the negative controls (only the luciferase RNAi and flySAM controls are pictured here).

Figure S3-S6: Functional screening of up-regulated candidate genes.

A-E: We selected 19 up-regulated candidate genes for functional screening, which we selectively knocked down in glia to examine their influence on lifespan. For each up-regulated gene, we screened two RNAi lines (to control for possible off target effects). Of the 19 up-regulated candidates screened, we found that RNAi knockdown of 4 genes led to consistent lifespan decreases for males. Alternatively, for female flies, RNAi knockdown of 3 genes led to consistent lifespan increases.

Figure S7-S8: Functional screening of down-regulated candidate genes.

A-J: We selected 29 down-regulated candidate genes for functional screening, which we selectively overexpressed in glia to examine their influence on lifespan. For each of the 29 down-regulated genes, we screened one overexpression line (using either UAS-cDNA lines or flySAM2.0 lines), when available. In total, we were able to acquire and screen lines for 19 genes. Of these candidates, overexpression of 2 genes led to lifespan increases for males, whereas overexpression of 3 genes led to lifespan decreases. Alternatively, overexpression of 10 genes led to lifespan increases for females, whereas overexpression of 1 gene led to decreased lifespan. We found that constitutive overexpression of DIP-β in glia significantly increased lifespan in both males and females compared to controls.

Figure S9: Single-nucleus RNA-sequencing - investigating the downstream transcriptomic effects of pan-glial DIP-β overexpression.

A: In total, we sequenced approximately 49,000 cells from our fly head samples, with approximately 23,000 from the glial DIP-β overexpression, (i.e., Ru486+) sample and approximately 26,000 from the negative control (i.e., Ru486-) sample.

B: Detailed cell subtype cluster composition annotations.

C: A detailed analysis investigating differentially expressed genes (DEGs) across cell subtypes.

1681 **Supplementary Table 1: Original proteomic data prior to analyses.**
1682
1683 **Supplementary Table 2: Candidate genes selected for further investigation.**
1684 **a:** In total, we selected 29 down-regulated candidate genes for functional screening. Candidate
1685 genes were selected for further screening only if they were known (or predicted) to be located
1686 either on the cell-surface or in the extracellular space.
1687 **b:** In total, we selected 19 up-regulated candidate genes for functional screening. Candidate
1688 genes were selected for further screening only if they were known (or predicted) to be located
1689 either on the cell-surface or extracellular space. Most candidate genes selected for further
1690 screening were found to have at least one strong human ortholog (Wang et al., 2017; Wang et
1691 al., 2019a; Wang et al., 2019b).
1692
1693 **Supplementary Table 3: RNAi lines used to screen up-regulated candidate genes and OE**
1694 **lines used to screen down-regulated candidate genes.**
1695 For each of the 19 up-regulated candidate genes, we screened 2 RNAi transgenic lines to control
1696 for potential off-target effects. For each of the 29 down-regulated genes, we screened one
1697 overexpression line (using either UAS-cDNA lines or flySAM2.0 lines), when available. Of the 29
1698 down-regulated genes selected, we were able to acquire and screen lines for 19 genes.
1699